A Study of Biomedical Sensors Based on Layered Semiconductors: From Characteristics to Nanofabrication Approaches

by

Byunghoon Ryu

A dissertation submitted in partial fulfillment
of the requirements for the degree of
Doctor of Philosophy
(Mechanical Engineering)
in the University of Michigan
2020

Doctoral Committee:

Associate Professor Xiaogan Liang, Chair
Professor Katsuo Kurabayashi
Assistant Professor Andrej Lenert
Professor Wei Lu

Byunghoon Ryu
bhryu@umich.edu
ORCID iD: 0000-0003-3654-6198

Acknowledgments

First and foremost, I would like to thank my advisor, Prof. Xiaogan Liang, for giving me an opportunity to dive into the wonderful nano research world. I am greatly appreciative of what he has offered me. He not only helped me financially but also supported me as a sincere mentor. What he frequently said to his students, I remember, is to be a “troubleshooter”, not a “troublemaker”. The word stuck into my mind and always makes me feel the responsibility of a doctorate. He never forced me to follow his point. Instead, he was open to my idea and thought and gave me the freedom to choose the research topic that I found interesting. His invaluable guidance, encouragement, and patience enabled me to complete this thesis successfully.

I am extending heartfelt thanks to my committee members, Prof. Katsuo Kurabayashi, Prof. Wei Lu, and Prof. Andrej Lenert, for their valuable advice on my work. They allowed me to collaborate with their graduate students and use their lab equipment and supplies.

In particular, I am deeply grateful to Prof. Kurabayashi for having me involved in a series of collaborative projects. He has a keen sense of connecting various research items and combining them into a novel topic of study. I learned a lot from him about not only technical/theoretical backgrounds but also how to communicate and work together with other researchers. I would also like to especially thank my mentor and collaborator, Dr. Younggeun Park, for sharing his great research experiences and skills with me. He was a person of a strong drive who can make something meaningful even in any situation. Notably, he helped shape my abstract research ideas to be more feasible and worthwhile.

I also want to express thanks to previous and current members in Nanoengineering and Nanodevice lab (NNL): Dr. Sungjin Wi, Dr. Hongsuk Nam, Dr.

Mikai Chen, and Da Li. As collaborators or friends, they gladly shared their knowledge and were willing to support my works. I was lucky to have such great colleagues in Michigan.

I enormously appreciate my parents, grandparents, and brother for their unconditional love, patience, support, and encouragement. They believed me a valuable person more than I believed in myself. They were always on my side during my Ph.D. program. Without their back up, this thesis could not exist.

Last but not least, let me express my sincere gratitude to my fiancée, Hye-ran Moon, who has been and will be the love of my life forever. She was far away from me over the years of graduate study. The famous proverb, "out of sight, out of mind," loses its effect on us. Even out of sight, our mind and love remained unchanged. She was always supportive and gave me warm encouragement. It is no exaggeration to say that her love makes me successfully finalize this thesis. Now, I am happily anticipating our wedding ceremony in the upcoming December.

05/06/2020

Byunghoon Ryu

Table of Contents

List of Figures

List of Tables

List of Appendices

Abstract

Among other layered two-dimensional (2D) materials, transition metal dichalcogenides (TMDCs) have revealed their importance in developing novel electronic devices such as field-effect transistors (FETs), optoelectronics, and biomedical sensors. The superior electrical, mechanical, and optoelectronic characteristics, in combination with naturally formed sizable and tunable bandgap of TMDCs, have turned out to be promising for making new biomedical sensors. Despite such a bright prospect, there remain critical scientific and technical gaps that should be filled to enable advanced and practical biomedical sensor applications. Specifically, such gaps include (i) loss of operation stability of MoS_2 FET biosensors under wet conditions, (ii) lack of reusability of the electronic biosensors made of TMDCs, and (iii) absence of scalable nanofabrication methods capable of producing well-defined TMDC device patterns.

A series of studies presented in this thesis leveraged scientific and technical knowledge to deal with the aforementioned urgent demands and was categorized into three main topics: (i) devise a cycle-wise method for operating MoS_2 FET biosensors integrated with a microfluidic channel, which alleviates the liquid-solution-induced issues; (ii) design a new biosensor structure consisting of a bio-tunable nanoplasmonic window and a low-noise few-layer MoS_2 photodetector, which can enable highly sensitive, fast, and reusable biosensing processes; (iii) invent scalable nanofabrication and nanomanufacturing approaches capable of producing orderly-arranged TMDCs device channel patterns at designated locations on a target substrate.

The first topic (*i.e.,* the second chapter) presents a cycle-wise method for operating MoS_2 FET biosensors to quantify fM-level disease-related biomarkers. This approach enhances the detection performance of the MoS_2 FET sensors by providing a series of advantages such as fast detection, low-noise, and high specificity. In this detection scheme, the MoS_2 FET sensing channel is integrated with a microfluidic structure that delivers reagent fluids to the sensor in a time-sequence order. The reagent fluids (*e.g.,* Analyte solution, Deionized (DI) water, Phosphate buffer solution (PBS), and Air) periodically set the sensing channel into four different cycle stages: incubation, flushing, drying, and measurement (*i.e.,* an IFMD cycle). Such a cycle-wise approach can physically prevent the electrical sensing components from being exposed to liquid solutions, which significantly mitigates liquid-solution-induced issues such as electrochemical damage, electronic noise, signal screening, and nonspecific adsorption. Due to such benefits, the cycle-wise method can significantly improve sensors' sensitivity, durability, detection limit, and specificity. In my experimental demonstration, MoS_2 FET sensors, in combination with the cycle-wise method, can quantify streptavidin and interleukin -1β (IL-1β) biomarkers with a detection limit as low as 1 fM within a total assay time less than 23 min.

The second part (*i.e.,* the third and fourth chapters) exhibits a highly sensitive and label-free biosensor consisting of a plasmonic window that is bearing gold nanoparticles (AuNPs) and a few-layer MoS_2 photodetector. The plasmonic window is located 100 μm above the MoS_2 photodetector, which physically separates the MoS_2 device from the plasmonic window where the binding reaction happens. Due to such a new decoupled sensor structure, the few-layer MoS_2 photodetector can be reused for multiple sensing cycles. With presence of an analyte solution to the plasmonic window, binding reactions occur at the surface of antibody-functionalized AuNPs, which results in the redshift of the extinction spectrum peak of the AuNPs due to the shift of localized surface plasmon resonance (LSPR) peak. In this process, the extinction peak shift, dependent on the concentration of analyte solution, dynamically modulates the intensity of the light transmitting to the MoS_2 photodetector. The measured photocurrents here serve as the sensor response signals for quantifying the concentration of analyte solutions. Such a new biosensor can quantify the concentrations of interleukin-1β (IL-1β) with limit-of-

detection (LOD) of 250 fg/mL (14 fM) and dynamic concentration range as large as 10^6. The assay time for quantifying each concentration requires ~ 10 min. Multiple such biosensors have been also utilized to detect CitH3, a biomarker indicating the sepsis. Due to the excellent detection capabilities such as high sensitivity, high accuracy, high detection speed, and label-free detection, the developed biosensors can successfully quantify the concentrations of circulating CitH3 and other biomarkers such as procalcitonin (PCT) and IL-1β in a living mouse.

The third part (*i.e.,* the fifth and sixth chapter) focuses on developing scalable nanofabrication methods capable of producing layered semiconductors (TMDCs, *e.g.,* MoS_2) patterns without requiring additional resist-based lithography and plasma-based etching processes. Specifically, various techniques (*e.g.,* triboelectric effect or inkjet printing) have been applied to modify the surface property of a substrate, which results in triboelectric charge patterns or local topography changes on the substrate. In the basis of these two surface modification approaches, new nanofabrication methods are named as rubbing-induced site-selective (RISS) and inkjet-defined site-selective (IDSS), respectively. The modified regions of the substrate possess a high affinity to precursor molecules, thus inducing site-selective nucleation of MoS_2 during chemical vapor deposition (CVD). The site-selectively formed MoS_2 lines and pixels by RISS and IDSS have been utilized to produce arrays of field-effect transistors (FETs). The yield of working FETs produced by RISS is about ~ 76 %, and such devices exhibit a good device-to-device consistency in transport characteristics. The site-selective synthesis methods presented here are facile, scalable, and cost-efficient. More importantly, they do not require exquisite lithographic tools and reduce the chance of serious contaminations.

The presented works have engineered layered semiconductors and device structures based on the scientific knowledge and device physics to realize practical and functional TMDC-based biomedical devices. Additionally, the nanofabrication methods invented in this thesis work could be further developed into cost-efficient and scalable nanomanufacturing techniques that will speed up the development of a wide variety of new device applications made of layered semiconductors.

Chapter 1

Introduction

1.1 The Emergence of Atomically Layered Materials

The first layered material introduced to the scientific community is graphene. In 2004, Andre Geim and Konstantin Novoselov successfully isolated a two-dimensional (2D) graphene layer and broke the prevalent belief that planar graphene cannot stably exist in the free state [1]. Graphene consists of sp^2 hybridized carbon atoms forming a hexagonal or honeycomb structures, and its thickness can be scaled down up to the diameter of an atom [2]. The covalent bond between carbon-carbon atoms makes graphene the most robust material ever reported. For example, tensile strength and Young's modulus (stiffness) of graphene are reported as 130 GPa and 1 TPa, respectively [3]. Such superior mechanical robustness of graphene is over 100 times higher than that of the strongest steel by weight [4]. Furthermore, such a carbon-carbon bond in graphene shares three electrons and lets a fourth electron be delocalized over the whole graphene layer, which leads to the conduction of electrical current [5]. More interestingly, such delocalized electrons behave uncommonly and form an energy band that consists of two circular cones with connected extremities, which is referred to as Dirac cones [5]. Such a band structure cannot belong to an insulator nor a metal. Instead, the unique energy band makes graphene electrons move with the same velocity and no inertia as if they have no

mass (*i.e.,* massless Dirac Fermions) [6]. As massless Dirac Fermions, electrons in graphene are less vulnerable to scatterings originated from defects in graphene layers; thus, leading to ultrahigh carrier mobility about ~ 15,000 $cm^2\ V^{-1}\ s^{-1}$ at room temperature [6]. Such extraordinary properties of graphene have attracted considerable attention and evoked a gold rush in the fields of nanoelectronics, quantum science, and condensed matter physics. Motivated by the first layered material, graphene, explosive research has been conducted to dig out the undiscovered or underestimated potential of other families of atomically layered materials such as black phosphorus [7], layered metal oxides, hexagonal boron nitrides (h-BN) [8], and transition metal dichalcogenides (TMDCs) [9].

Especially, molybdenum disulfide (MoS_2), one of the transition metal dichalcogenides (TMDCs), was mostly known as a promising dry lubricant in the field of tribology due to its 2D lamellar structure that can easily slide against each other [10]. Ever since the first study about the unique electrical properties of monolayer MoS_2 conducted by Andras Kis in 2011, however, intense research in TMDCs has been ignited. In the study from the Kis group, monolayer MoS_2 is fabricated as active field-effect transistors (FETs). The reported unique electrical properties of monolayer MoS_2 are including direct bandgap (~ 1.8 eV), high current on/off ratio (> 10^8), and good mobility (~ 700 $cm^2\ V^{-1}\ s^{-1}$) [11]. Such a high field-effect mobility and current on/off ratio cannot be achieved by using graphene due to the lack of a bandgap. Furthermore, the bandgap of MoS_2 gradually decreases from ~ 1.8 eV (Direct, Monolayer) to ~ 0.9 eV (Indirect, Bulk) with increasing the thickness of the layer [11]. Not only MoS_2, but many 2D TMDCs are semiconductors with a sizable and tunable bandgap (Figure 1.1), which implies that the TMDCs can be used to fabricate next-generation low-power electronic devices. Such tunable bandgap energy of 2D TMDCs, which is in the range of visible to near infra-red light in combination with strong photoluminescence (PL) and large exciton energy, opens up new opportunities in the study of optoelectronic devices such as photodetectors, photovoltaics, and light-emitting diodes [12-13].

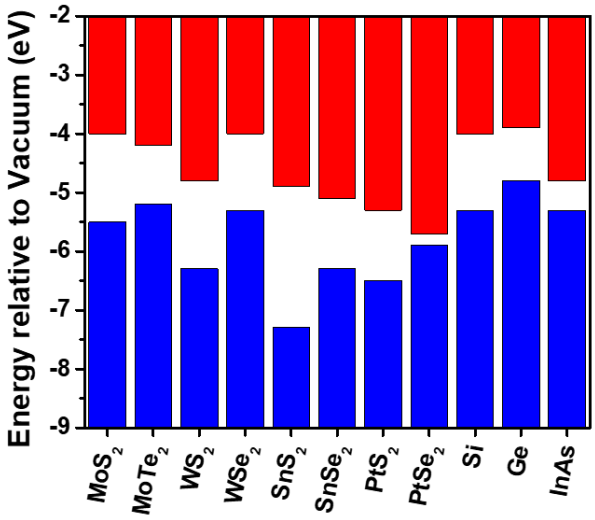

Figure 1.1 Bandgap energy of various TMDCs and conventional semiconductors

More importantly, researchers have already discovered atomically layered materials showing conducting (*e.g.,* graphene), semiconducting (*e.g.,* TMDCs), and insulating (*e.g.,* h-BN) behaviors, which can be primary building blocks to fabricate next-generation electronic devices. By virtue of such discoveries, new approaches have been made to produce electronic devices composed of only atomically layered materials, which is considered as ideal structures that can overcome short channel effects and beyond Moore's law (Figure 1.2) [14].

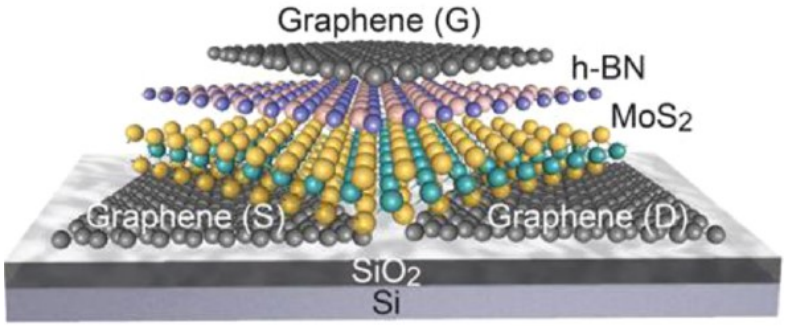

Figure 1.2 A field-effect transistor fabricated by using stacked atomically layered materials. Courtesy of reference [14]

In addition to the characteristics as mentioned earlier, atomically layered materials also exhibit extraordinary mechanical properties stemmed from the nature of two-dimensionality and extremely low density of surface defects. The covalent bonds connecting the neighboring atoms in the same plane efficiently diffuse and endure strain energy applied from externally applied mechanical stress. Moreover, the defect-free surface of the layered materials can minimize localized stress concentration, which results in strong in-plane mechanical properties [15]. For example, MoS_2 has Young's modulus (stiffness) of ~ 270 GPa, which is higher than that of steel (~ 200 GPa) and can sustain mechanical strain up to ~ 11 % from its original length without experiencing any mechanical fracture [16]. Such excellent mechanical properties of atomically layered materials can be utilized to speed up the development of flexible and wearable electronic devices [17-18]. The atomically layered materials also exhibit a significantly large specific surface area due to their 2D planar structure and atomic-level thickness. Among the layered materials, graphene is reported to have the largest specific surface area of ~ 2150 $m^2 g^{-1}$ [19] and relatively large specific surface area as high as ~ 210 $m^2 g^{-1}$ is also reported for MoS_2 [20]. Such a large specific surface area leads to a large surface-to-volume ratio which is a key factor to design and fabricate devices requiring extreme surface sensitivity such as sensors [21], photo/electro-catalysis [22-23], supercapacitors, and solar cells [24].

1.2 Promising Characteristics of Semiconducting Transition Metal Dichalcogenides for Biomedical Sensor Applications

The crystal structure of transition metal dichalcogenides (TMDCs) is represented as MX_2, where M is a transition metal (M) which belongs to group IV, V, or VI in the periodic table, and X is from a chalcogen atom (S, Se, or Te) [25-27]. A single layer of TMDCs is composed of a central transition metal (M) sandwiched by two chalcogen atoms. Multiple stacking of such a single layer leads to a multilayer TMDCs and each layer is bound by van der Waals (vdW) interactions (Figure 1.3) [25, 28-29]. Such a weak vdW force between TMDCs layers can enable the cleavage of a single layer using

mechanical exfoliation method [30-32]. In recent years, a number of studies have reported that TMDCs have a great potential to be utilized for producing a biomedical sensor that exhibits unprecedented sensing capabilities due to their attractive properties [33-35].

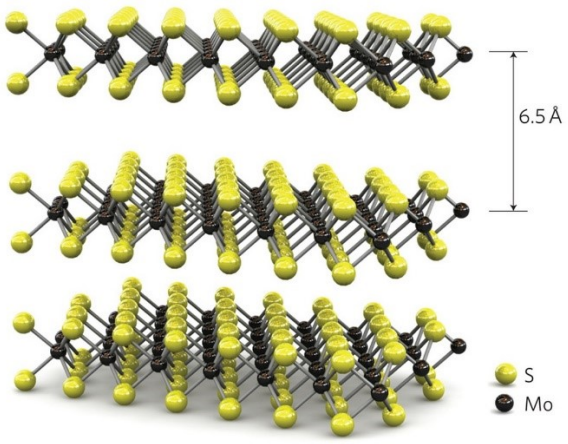

Figure 1.3 Crystal structure of multilayer of MoS_2. Covalent bond between Mo and S form a single layer. Thickness of the single layer is ~ 0.65 nm. Courtesy of reference [11]

Especially, MoS_2, the most famous TMDC, exhibits promising properties such as large specific surface area, no dangling bonds and defects on the surface, high carrier mobility, sizable bandgap, excellent mechanical flexibility, and good stability in a liquid environment, which are beneficial to a biomedical sensor [36-37]. The atomically thin 2D layer of MoS_2 results in the extremely high surface-to-volume ratio which makes the surface of MoS_2 ultrasensitive to external stimuli. As an example, the high surface-to-volume ratio indicates that the whole thickness of MoS_2 is influenced by binding reactions between antibody and antigen biomolecules [38]. To be specific, adsorbed target biomolecules can interfere with the flow of charge carriers in the atomically thin layer of MoS_2 by inducing scattering or depletion of the carriers, which leads to a current sensor signal change in an electronic biosensor [39]. Furthermore, defects/dangling bonds-free surface of MoS_2 can minimize the intrinsic electrical noise of the biosensor, which contributes to achieving a high signal-to-noise ratio. A particular merit of MoS_2 differentiated from other 2D layered materials is the existence of bandgap, which can

further enhance the biosensing performance. The bandgap of MoS_2 forms the source-to-channel barrier which allows only electrons having higher energy than the barrier can travel across the MoS_2 sensing channel. Such a modulation effect of the bandgap restricts the total number of electrons in the MoS_2 channel by forbidding the tunneling leakage current often observed in no or small bandgap materials such as graphene or reduced graphene oxide (rGO) [35]. Since the sensitivity of electronic biosensor is inversely proportional to the concentration of electrons in the channel as shown in equation (1), the sensitivity of the biosensor made of MoS_2 is ~ 74 times higher than that of the biosensor based on graphene [35]. Equation (1) expresses the sensitivity of electronic biosensors, where S represents sensitivity of the biosensor, $N_{Analyte}$ is the concentration of analyte biomolecules, N_e is the concentration of electrons, and R is the geometric factor of the biosensor.

$$S \sim \frac{N_{Analyte}}{N_e R} \qquad (1)$$

In addition, the superior optical properties of TMDCs can be exploited to design an ultrasensitive sensor signal detector. The band structures of TMDCs are either fully or partially quantized along the z-direction as the thickness of them evolves from mono- to multilayers, which results in Van Hove singularities forming sharp peaks in the density of states (DOS) at specific energy levels (Figure 1.4) [40]. Such singularities appearing close to the band edges make charge carriers flowing across TMDC channels stationary at certain wave frequencies. Therefore, the charge carriers behave very sensitively to externally applied electromagnetic stimuli, which effectively causes *e-h* pairs (*i.e.,* excitons) upon illumination of light with higher energy than the bandgap. Due to such an exciting feature of TMDCs, a monolayer TMDC (~ 0.6 nm thick) can absorb a comparable amount of sunlight with that much thicker conventional semiconductors (50 nm thick silicon or 12 nm thick GaAs) can absorb [40]. Many biosensors already commercialized in the market are based on an optical sensing scheme by conjugating tagged fluorophores onto the surface of the biosensor. Such tagged fluorophores absorb incident light and re-emit corresponding fluorescent light depending on the extent of

binding reactions. Therefore, the detectivity of an optical detector plays a vital role in determining the sensitivity of the biosensor [41]. In this regard, an optical detector designed by using TMDCs can surpass the sensitivity of current detectors made of conventional semiconductors. Moreover, the mechanical robustness and flexibility in combination with keen sensitivity in light can enable TMDCs to become a promising candidate for fabricating a miniaturized flexible and wearable biomedical sensor.

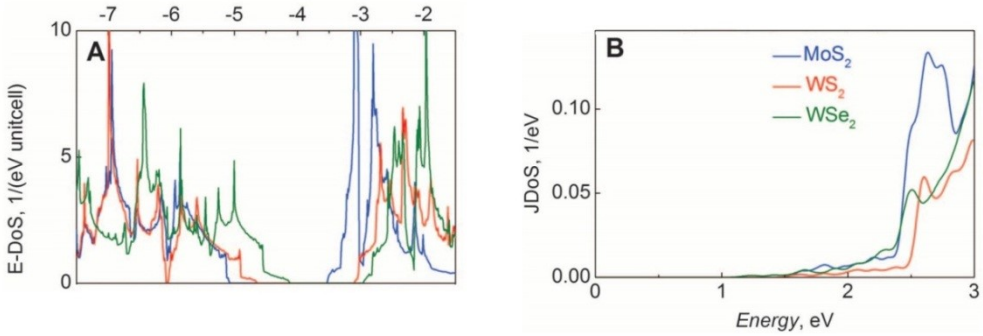

Figure 1.4 The Density of State (DOS) obtained from monolayer TMDCs. (a) Electronic DOS for monolayer MoS_2, WS_2, and WSe_2. Sharp peaks known as Van Hove singularities induce a strong light-matter interaction. (b) Joint Density of State for monolayer MoS_2, WS_2, and WSe_2. Courtesy of reference [40]

1.3 Need of Developing Novel Biomedical Sensors and Nanofabrication Technologies Compatible with Layered Transition Metal Dichalcogenides

The current gold standard of biosensing is an enzyme-linked immunosorbent assay (ELISA) method [42]. The ELISA has become a critical assay tool widely used in clinical diagnostics due to its relatively high sensitivity, the capability of multi-assay using 96 wells, and a well-developed operation manual [43]. However, even though the advantages of ELISA mentioned above, a series of challenges have brought on continuous demands to develop a new biosensor. For example, the secondary antibodies used to label target analytes significantly prolong the total assay time (usually over 10 hours) and aggravate the complexity in the assay process [44]. Additionally, a large volume of a sample should be prepared for the fluorescent-based detection of ELISA to

attain reliable sensor signals with a sufficiently high signal-to-noise ratio. On top of everything else, the ELISA further requires an expensive and bulky fluorescence microplate reader, which makes the use of the ELISA method available only at the laboratory [45].

Among manifold biosensing principles suggested so far, a nanoelectronic biosensor based on layered transition metal chalcogenides (TMDCs) has occupied an important position as a complementary substitute for the ELISA. Specifically, a field-effect transistor (FET) MoS_2 biosensor can enable label-free biosensing and only requires a minimal amount of sample volume, which simplifies and speeds up the whole assay process (Figure 1.5). The MoS_2 FET biosensor also exhibits exceptionally high sensitivity and surprisingly low limit-of-detection (LOD), which raises the possibility of the detection of biomarkers at the early stage of the disease [46]. However, even such promising MoS_2 FET biosensor still has some drawbacks such as loss of sensitivity and stability under liquid environment and lack of reusability. Similar to other electronic devices, MoS_2 FET biosensor is highly vulnerable to a wet environment. In the current operation method, however, the sensing channel of MoS_2 is exposed continuously to a liquid analyte solution (Figure 1.5), which impedes the stability of biosensor. Furthermore, to realize real-time monitoring of disease-related biomarkers, the FET biosensor should be electrically biased all the time during the detection process. Such electrical stresses under the liquid environment can lead to unexpected current leakage, severe electronic noises, and false signals. More seriously, the analyte solution consisting of high ionic strength medium and biomolecules can generate a series of conduction pathways over the device, which can permanently damage the biosensor [47]. Therefore, there is a soaring demand to design an appropriate operation method for MoS_2 FET biosensors to avoid the issues induced by liquid analyte solution.

Another issue in the MoS_2 FET biosensor is that there is no effective way to recycle the sensor already used for detection once [48]. This issue is stemmed from the fact that antibody receptors directly grafted on the surface of the MoS_2 channel cannot be removed or refreshed even after performing several washing steps [49]. Such lack of reusability puts a damper on the economics of the biosensor because the biosensing process often requires multiple repetition tests for more accurate and reliable diagnostics.

Even if an efficient mass-production method of a disposable MoS_2 biosensor is developed in the future, a reusable biosensor scheme is still needed to be developed to save resources and get rid of additional labor for the replacement of the disposable biosensor. The unique benefits of TMDCs have to be maximally considered in device design processes to develop such a reusable biosensor made of TMDCs with maintaining the superior sensing capability.

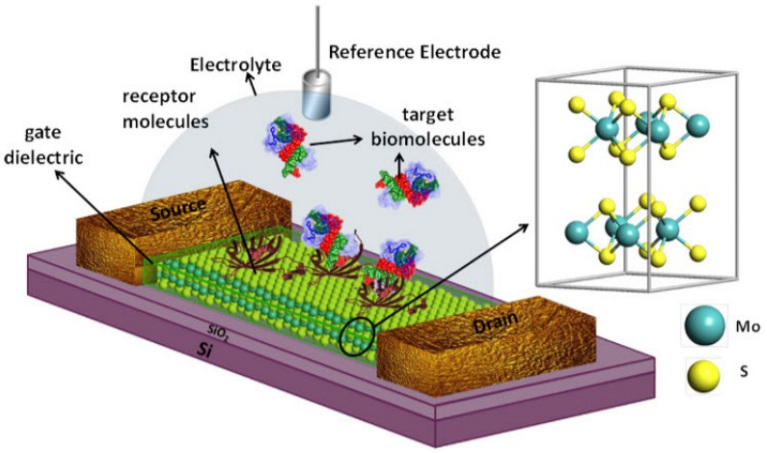

Figure 1.5 A schematic illustration of a MoS_2 field-effect transistor (FET) biosensor. Courtesy of reference [35]

More general, but the most urgent issue in TMDCs is the absence of scalable nanofabrication techniques, which retards the development of practical and functional devices leveraging the superior properties of TMDCs. The desirable nanofabrication technique should be compatible with TMDCs and needs to be able to produce TMDC materials with a large area or pattern arrays onto designated device locations. However, current methods, such as mechanical exfoliation and chemical vapor deposition (CVD), cannot meet these requirements. Specifically, in the mechanical exfoliation method, TMDC flakes are transferred from a bulk ingot to the surface of a target substrate using the scotch tape (Figure 1.6 (a)) [50]. However, this method is not suitable for large fabrication, and the thickness and location of the transferred TMDCs are very random, which shows no controllability. Even in CVD regarded as a reliable method to grow a

large-area TMDC layer has some critical issues (Figure 1.6 (b)) [51]. First, the quality of the CVD grown layer is far below that of the exfoliated one due to the small grain size formed during the CVD process. Furthermore, the large-area TMDC layer should be patterned into individual device channels to fabricate functional devices. In this patterning process, photoresist-based lithography and plasma-based etching processes should be involved, and such processes induce inevitable contaminations that degrade the performances of the device [52-53]. Unfortunately, the research community still highly rely on the above methods and has a long way to go to develop new nanofabrication methods.

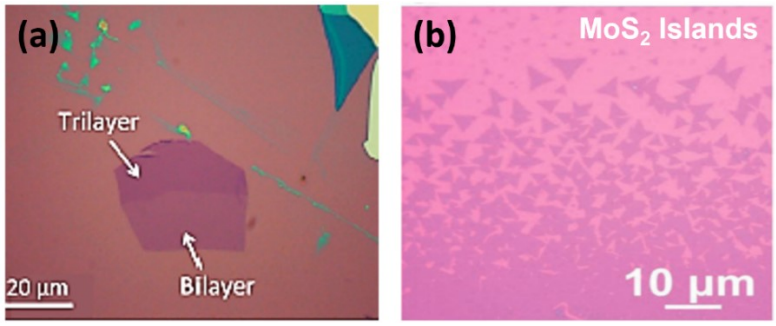

Figure 1.6 (a) A MoS_2 flakes isolated by using mechanical exfoliation, (b) MoS_2 islands synthesized by using chemical vapor deposition (CVD). Courtesy of references [50-51]

1.4 Summary of Dissertation

In response to the critical challenges described in Chapter 1.3, a series of research projects have been conducted. Specifically, such research projects can be classified into three main topics including: (i) design a new operation method for MoS_2 FET biosensors to mitigate the liquid-solution-induced issues (Chapter 2); (ii) develop a reusable biosensor structure by combining a nanoplasmonic window and a MoS_2 photodetector for realizing high-sensitive and fast biosensing application (Chapter 3 and 4); (iii) devise scalable nanofabrication techniques compatible to TMDCs for producing highly-uniform and large-array TMDCs device channel patterns (Chapter 5 and 6).

In Chapter 2, a cycle-wise operation method is presented, which consists of four assay cycles, including incubation, flushing, drying, and electrical measurement. During the cycle-wise method, a series of reagent fluids (analyte, water, and air) are subsequently supplied to the sensing channel of MoS_2 FET biosensors. This cycle-wise detection approach makes the sensing channel dry during the electrical measurement step, which rules out the liquid-solution-induced issues. In synergy with the innate high sensitivity of MoS_2 FET biosensors, the cycle-wise operation method can achieve rapid biomolecule quantification at femtomolar levels. The detection limit for quantifying an interleukin-1β (IL-1β) cytokine is as low as 1 fM and a total assay time is ~ 23 min.

In Chapter 3, I present a bio-tunable nanoplasmonic biosensor which consists of a bio-tunable nanoplasmonic window and a low-noise few-layer MoS_2 photodetector. The bio-tunable nanoplasmonic window fabricated by depositing antibody-conjugated gold nanoparticles on a SiO_2 thin layer is placed 170 μm above the MoS_2 photodetector. Here, the MoS_2 photodetector is reusable many times because it is physically separated from the nanoplasmonic window where binding reactions really happen. The operation principle of the biosensor is based on tuning the intensity of incident light delivered to the MoS_2 photodetector through biomolecular binding-induced localized surface plasmon resonance (LSPR) peak shifts occurred at the nanoplasmonic window. Depending on the concentration of cytokines on the nanoplasmonic window, corresponding level of photocurrent is generated by the MoS_2 photodetector. Using the developed biosensor, the concentration of IL-1β cytokine is quantified with a detection limit as low as 14 fM and a short assay time of 10 min.

In Chapter 4, I construct a highly miniaturized (250 x 250 μm^2) plasmo-photoelectronic nanostructure device which can be applied to point-of-care (POC) applications. This biosensor shares the working principle and device structure with the device developed in Chapter 3. However, in this chapter, highly ordered hemispherical gold nanoparticle arrays are structurally engineered, and high-affinity antibodies are employed to the biosensor. Due to such improvements, femtomolar-level sepsis biomarkers in serum are detected with a dynamic range of 10^5 and a sample-to-answer time ~ 20 minutes. Furthermore, by exploiting the fast and ultrasensitive characteristics

of the biosensor, dynamic biomarker profiles in sepsis mouse models are successfully demonstrated by using living mice.

Chapter 5 introduces a rubbing-induced site-selective (RISS) method capable of directly generating few-layer MoS_2 device patterns without the need of any additional patterning processes. This method consists of two steps: (i) a damage-free mechanical rubbing process for generating microscale triboelectric charge patterns on a dielectric surface and (ii) site-selective deposition of MoS_2 within rubbing-induced charge patterns. The microscopy characterizations in combination with finite element analysis indicate that the field magnitude distribution within triboelectric charge patterns determines the morphologies of grown MoS_2 patterns. The RISS method can demonstrate MoS_2 line/spacing patterns with various periods ranging from 200 nm to 20 μm. In addition, the MoS_2 line patterns produced by the RISS method have been implemented for making arrays of working transistors and memristors. These devices exhibit a high yield of ~76 % and a good device-to-device consistency in their critical performance parameters.

In the work presented in Chapter 6, I introduce an inkjet-defined site-selective (IDSS) method that can generate MoS_2 arrays without using any patterning processes. The IDSS includes two main steps: (i) inkjet printing of microscale liquid droplets that define the designated sites for MoS_2 growth, and (ii) site-selective growth of MoS_2 at droplet-defined sites. In the IDSS method, it is confirmed that an array of in-plane and out-of-plane MoS_2 structures with bountiful edges are preferentially grown at locations where DI and graphene ink droplets are printed, respectively. The IDSS can fabricate in-plane MoS_2 pixel features with various periods of 200 μm, 350 μm, 500 μm, and 650 μm. Furthermore, an out-of-plane MoS_2 pixel synthesized on graphene is demonstrated as an efficient lithium-ion battery due to its rich of exposed edges. Such a demonstrated battery exhibits good discharge/charge capacity parameters (206 $\mu Ah/cm^2$ / 113 $\mu Ah/cm^2$ at 55 $\mu A/cm^2$ current density).

Chapter 2

Cycle-Wise Operation of Printed MoS_2 Transistor Biosensors for Rapid Biomolecule Quantification

2.1 Introduction

Field-effect transistor (FET) biosensors based on emerging layered transition metal dichalcogenides (TMDCs), such as MoS_2 and WSe_2, have been in a spotlight due to their superior characteristics, such as high sensitivity in biosensing, low limit-of-detection (LOD), and compatibility with planar nanofabrication approaches, which is possibly expanded into multiplexing sensor arrays. Recently, Wang et al. and Sarkar et. al. demonstrated MoS_2 FET biosensors with detection limits in femtomolar (fM)-level of biomarkers [54-55]. More recently, Nam et al. demonstrated the fabrication of MoS_2 FET arrays and studied the device physics to calibrate the sensor response signals obtained from MoS_2 FET sensors [56-57]. Lee et al. later reported that antibody receptors can be directly applied on the surface of MoS_2 FET channels, which is owing to the hydrophobicity of the MoS_2 surface [58]. Such a capability of direct grafting of receptors without insulating layer can minimize the fabrication complexity and cost of MoS_2 biosensors. Nam et al. further reported that insulating-layer-free MoS_2 sensors exhibit a higher sensitivity than insulating-layer-coated ones [59]. This can be explained by using two mechanisms, target-molecule-induced electrostatic doping and target-molecule-

induced surface scattering of carriers, which synergistically contribute to the response signal of an insulating-layer-free sensor. However only target-molecule-induced electrostatic doping dominantly affects the response signal of an insulating-layer-coated sensor [59-60].

Despite the noticeable progress listed above, MoS_2 and other FET biosensors still seriously suffer from challenges that impede their practical biomedical sensing applications. Especially, a FET sensor is required to be continuously exposed to a liquid reagent environment for quantifying the time-dependent reaction kinetics of analyte-receptor binding. The capability of a time-dependent detection plays an important role to realize fast biomolecule quantification which is based on sensor response readings at the non-equilibrium states of binding reactions, which could turn out very short detection times and enable fast real-time immunoassay for quantifying extremely low concentration biomolecules (e.g., fM-level biomarkers) [61]. However, unfortunately the electrical signal acquisition process is not generally compatible with such a liquid environment in the sensor. During a typical time-dependent detection process for quantifying the binding reaction kinetics, the sensing FET is electrically biased and constantly subjected to the analyte solution. The process applies a gate voltage (V_G) to bias the FET to the linear regime of the transfer characteristic to obtain a high sensitivity as well as a consistent sensor response behavior [57, 60], and a drain-source voltage (V_{DS}) for driving the sensing channel current (I_{DS}). Such continuous electrical stresses in the liquid reagent environment can result in undesirable leakage currents flowing to electrodes and therefore generate high-level electronic noises and false sensor responses, and even electrochemically damage the sensor. It should be noted that even the FET sensor coated with an insulating layer (e.g., TiO_2, SiO_2, or Al_2O_3 layers) can hardly survive in a long continuous time-dependent detection process (e.g., several hours) because of the electric-field-enhanced permeation of reactive ions into the insulating layer [62-63]. The analyte solutions with different ionic strengths also cause different degrees of the screening effect to the electrostatic interaction between target molecules and the sensing channel, resulting in inconsistent sensor response signals. Such a screening effect also degrades the biodetection sensitivity of the sensor [64-67]. Another serious issue associated with TMDC-based FET sensors is the hysteretic behavior of the transfer characteristics of such

sensors, which is attributed to the gate-modulated charges trapped at TMDC/dielectric interfaces [68]. Such a hysteretic behavior makes the I_{DS} value measured under a given V_G highly dependent on the sweep range, sweep direction, sweep time and loading history of V_G biases, therefore resulting in inconsistent sensor readings. To rule out such indeterminacy of sensor readings due to the hysteresis effect, ones need to measure the complete transfer characteristic curves (i.e., I_{DS}-V_G curves) by sweeping V_G along both positive and negative directions, which is similar to the way for characterizing a FET memory [69-71]. However, this electrical measurement process is not applicable during a continuous time-dependent detection process. Another expedient solution is to constantly bias the FET sensor to the linear (or highly conductive) transport regime, where the indeterminacy of I_{DS} values is relatively smaller than that in the subthreshold regime. However, as discussed above, such a constantly applied gate bias can easily damage the sensor. In addition, during a continuous time-dependent detection process, the nonspecific adsorption of untargeted molecules on the FET sensing channel can also generate false signals. All these issues seriously limit the applicability of TMDC-based FET biosensors for realizing rapid, highly specific biomolecule quantification using time-dependent sensor response signals or non-equilibrium-state sensor response readings.

In this chapter, we present a cycle-wise time-dependent biodetection method for operating MoS_2-based FET biosensors. Such a cycle-wise process alternatingly sets the FET sensor into incubation, flushing, and electrical measurement steps and therefore avoids the liquid-solution-induced electrochemical damage, screening, and nonspecific adsorption to the sensor. This method can also rule out the indeterminacy of sensor readings due to the hysteretic behaviors of TMDC FETs. This cycle-wise detection method in combination with the superior sensitivity and limit-of-detection (LOD) of TMDC-based biosensors enables rapid, low-noise, and highly specific biomolecule quantification with fM-level LODs even in complex analyte solutions. In this work, we have experimentally characterized time-dependent responses associated with the reaction kinetics of streptavidin-biotin, and Interleukin 1-beta (IL-1β)-antibody bindings and demonstrated fM-level streptavidin and IL-1β quantifications in pure as well as complex solutions (e.g., serum and saliva) with detection limit of ~1 fM and total detection time less than 23 min.

2.2 Experimental Setup and Operation Process for MoS_2 FET Biosensors

2.2.1 Fabrication of MoS_2 FET Biosensors and Integration of a Biosensor with a PDMS Microfluidic Channel

Figure 2.1 (a) shows the scanning electron micrograph (SEM) of several few-layer-MoS_2 FET channels prepared by using a printing approach previously reported by us [56]. The thicknesses of printed few-layer-MoS_2 FET channels are specifically controlled to be 5 - 10 nm. Such MoS_2 channel thicknesses can result in the optimal field-effect mobility and On/Off ratio values for the FETs [72-74]. Each of the printed channels is associated with a pair of Ti/Au align-marks, which are used for locating the FET channel specifically selected for making a working biosensor. Figure 2.1 (b) displays the optical micrograph of a representative FET biosensor consisting of a few-layer MoS_2 channel (thickness ~ 5 nm), a 300 nm thick SiO_2 back gate dielectric layer, a p^+-Si back gate, and a pair of metallic drain/source (D/S) contacts (10 nm Ti/50 nm Au). The FET channel length and width are 5 and 15 μm, respectively. Figure 2.1 (c) shows the photograph of a MoS_2 FET sensor integrated with a PDMS block bearing a microfluidic channel (10 mm in length, 200 μm in width, 50 μm in height). This microfluidic structure is connected with a syringe pump (not shown in Fig. 2.1 (c)) through a pair of inlet/outlet tubes (tube diameter: 0.75 mm). We can operate this pump/tubing system to deliver a time-sequenced series of reagent fluids to the FET sensing channel for performing cycle-wise biodetection process.

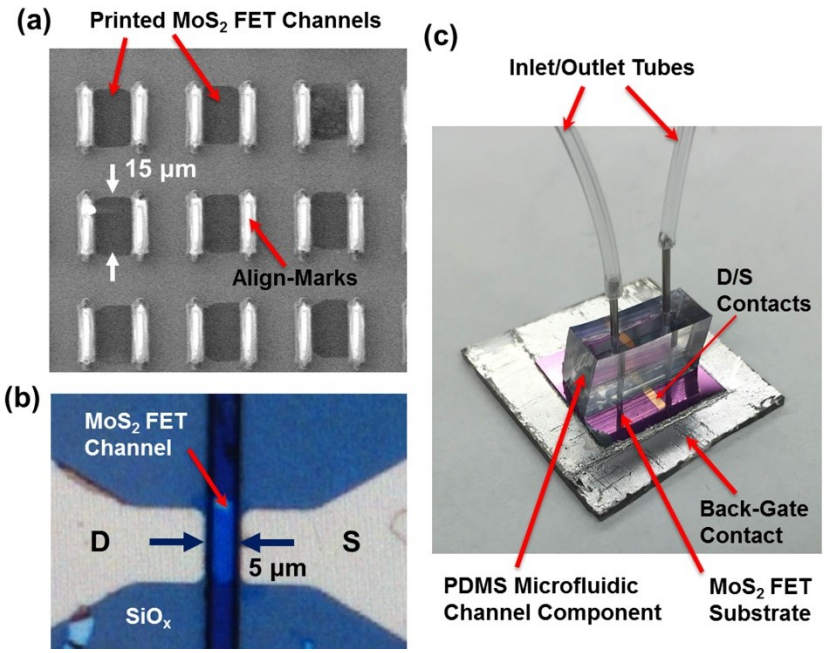

Figure 2.1 Biosensor fabrication and setup: (a) SEM image of several printed few-layer-MoS_2 FET channels; (b) optical micrograph of a representative few-layer-MoS_2 FET biosensor; (c) photograph of a MoS_2 FET sensor integrated with a microfluidic channel structure. In this work, the few-layer-MoS_2 FET channels were functionalized with either biotin or IL-1β antibody receptors, and we experimentally demonstrated time-dependent quantification of streptavidin-biotin or IL-1β-antibody binding kinetics.

2.2.2 Antibody-Functionalization of MoS_2 FET Biosensors

Figure 2.2 (a) illustrates the MoS_2-based back-gated FET biosensor under study, which is integrated with a polydimethylsiloxane (PDMS)-based microfluidic channel. Before a biosensing process, the sensing FET channel made from a few-layer MoS_2 flake is functionalized with specific antibody receptors for detecting the target molecules in the analyte solution. In this work, few-layer MoS_2 FET channels are functionalized with either biotin or IL-1β antibody receptors for detecting streptavidin or IL-1β molecules presented in pure and complex solutions, as illustrated in Figure 2.2 (b) and (c). Before functionalized with specific receptors, the as-fabricated MoS_2 FET biosensor is incubated in 5 % (3-Aminopropyl) triethoxysilane (APTES) in ethanol for 1 hour. In case of IL-1β antibody functionalization, additional 5 % glutaldehyde in Phosphate-buffered saline

(PBS) is used to incubate the FET sensor for another 2 hours. After the incubation process, the sensor is rinsed with deionized (DI) water and blown dry by using an air gun. 50 μg/ml NHS-biotin (for detecting streptavidin) or 50 μg/ml IL-1β antibody (for detecting IL-1β) in PBS is subsequently incubated on the MoS_2 FET channel area for 30 min followed by rinsing with DI water and air blow-dry.

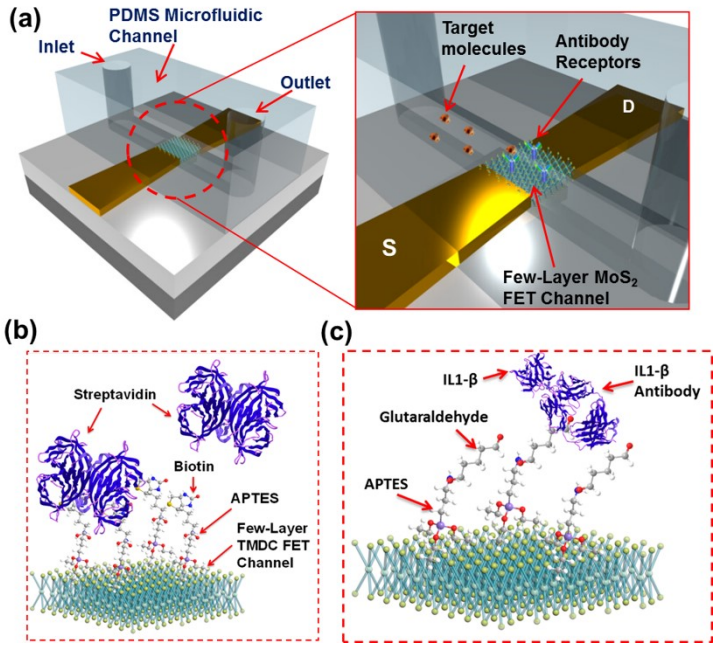

Figure 2.2 Experimental method: (a) illustration of a MoS_2-based FET sensor, which is integrated with a PDMS microfluidic structure for enabling the cycle-wise time-dependent detection capability; (b) and (c) illustrations of the few-layer TMDC FET channels that are functionalized with biotin and Interleukin 1-beta (IL-1β) antibody receptors, respectively.

2.2.3 Incubation-Flushing-Drying-Measurement (IFDM) Cycles for Operation of MoS_2 FET Biosensors

Figure 2.3 illustrates the cycle-wise biodetection and quantification process for operating a MoS_2 FET sensor. During this process, the microfluidic structure is operated to deliver a series of time-sequenced reagent fluids to the sensing FET channel and periodically set the sensor into four assay-cycle stages, including (i) incubation of the

sensing channel in the analyte solution containing target molecules for a short but deterministic duration (typically 5-10 min), (ii) flushing the sensing channel using pure buffer and DI water to eliminate unreacted target molecules and untargeted background molecules, (iii) drying the sensing channel using an air flow, and (iv) electrically measuring, under such a dry condition, the transfer characteristics (i.e., I_{DS}-V_G characteristic curves) of the sensing FET by sweeping V_G along both positive and negative directions. Repetitive operation with multiple such incubation-flushing-drying-measurement (IFDM) cycles can acquire a time-dependent sensor response signal associated with the reaction kinetics of analyte-receptor binding. During the IFDM cycle, the time durations for incubation in the analyte solution, flushing using pure buffer and DI water, drying using air flow, and electrical measurement are 10 min, ~5 sec, ~20 sec, and ~20 sec, respectively (*i.e.,* total time for a cycle is ~10.8 min).

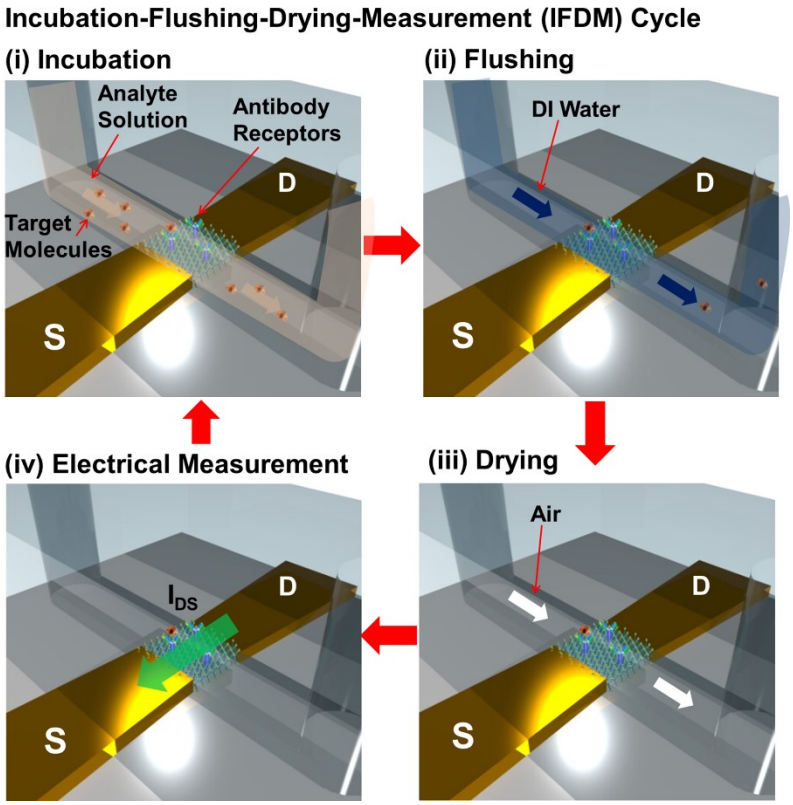

Figure 2.3 Cycle-wise biodetection process consisting of periodic incubation-flushing-drying-measurement (IFDM) cycles.

2.3 Experimental Results

2.3.1 Quantification of Streptavidin Biomarker Using MoS_2 FET Biosensors Operated by IFDM Cycles

Figure 2.4 shows the time-dependent transfer characteristics (*i.e.*, $I_{DS} - V_G$ characteristics) measured from a set of MoS_2 FET sensors, each of which was subjected to a different concentration of streptavidin (Figure 2.4 (a)-(f) shows the results for different streptavidin concentrations $n_{streptavidin}$ = 0, 1, 4, 20, 100, and 300 fM, respectively). Specifically, this set of MoS_2 sensors were fabricated in the same fabrication batch using our previously published nanoprinting method that can enable production of multiple few-layer MoS_2 FETs with a high device-to-device consistency in their transport characteristics [56]. During a detection course at a specific streptavidin concentration, one of the sensors was subjected to this concentration and operated using the IFDM cycle-wise method discussed above. For each IFDM cycle, the incubation time (T_i) was set to 10 min. In the following discussion, the sensor responses are analyzed as a function of accumulative incubation time (t), which is defined as $t = nT_i$ (here, n is the number of already performed IFDM cycles). In this experiment, the transfer characteristic curves of each MoS_2 sensor in response to a specific streptavidin concentration were acquired at a series of IFDM cycles with t values ranging from 0 to 110 min (*i.e.*, 11 IFDM cycles for a detection course). As shown in Figure 2.4, for each FET sensor in response to a specific streptavidin concentration, the linear regime of its transfer characteristic curve exhibits an evolutionary reduction of the FET transconductance (*i.e.*, $g_m = \frac{\partial I_{DS}}{\partial V_G}$ in the linear regime of the transfer curve) or the I_{DS} measured at given V_G and V_{DS} with increasing the accumulative incubation time t. Such a reduction behavior of g_m and I_{DS} values is attributed to the net effect of target-molecule-induced electrostatic doping and target-molecule-induced surface scattering of carriers [59-60]. In addition, the reduction rate and range of the g_m and I_{DS} values in the linear regime of the transfer curve become larger with enhancing the streptavidin concentration, as displayed by Figure 2.4 (a)-(f). This is attributed to the fact that the binding rate of biotin-streptavidin pairs increases with increasing streptavidin concentration, and the final occupancy of biotin

receptors at the equilibrium state of the biotin-streptavidin binding reaction becomes larger at the higher streptavidin concentration [75].

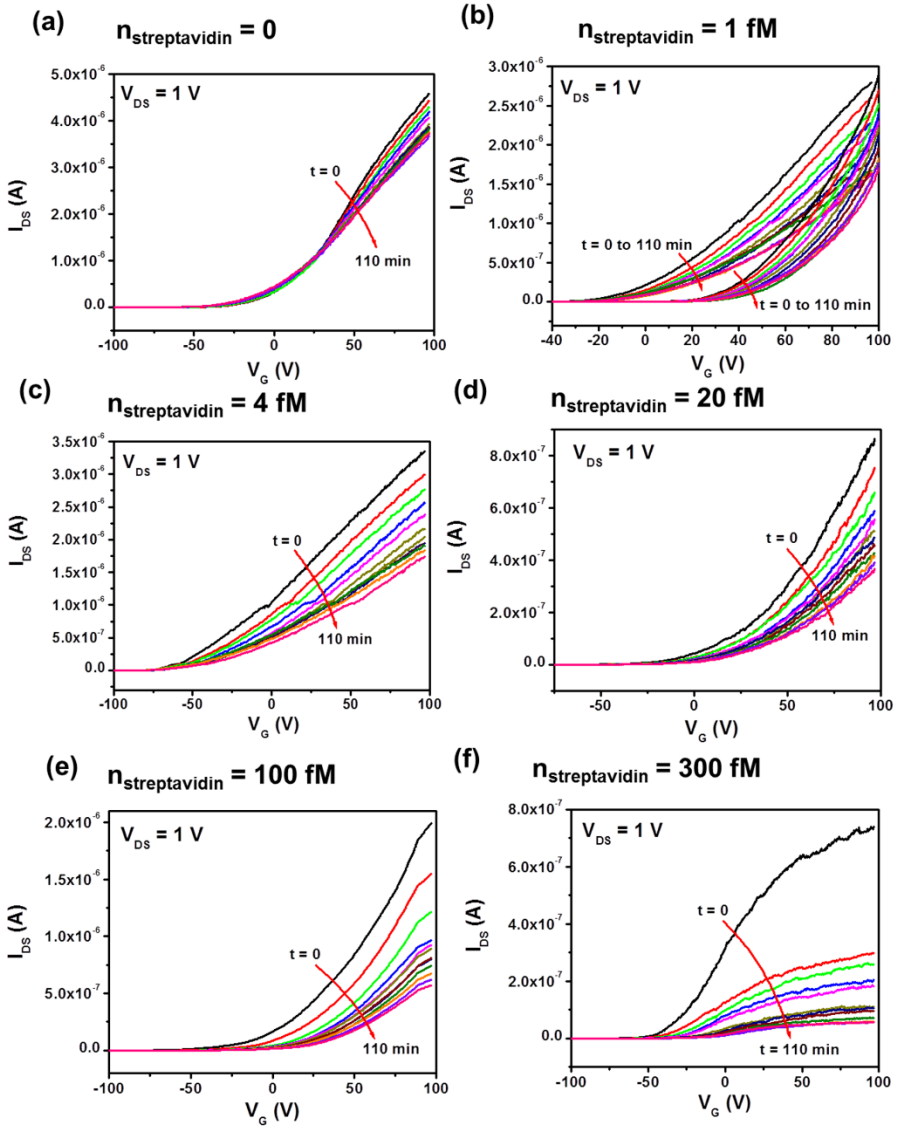

Figure 2.4 *t*-dependent $I_{DS} - V_G$ characteristic curves of a set of MoS_2 FET sensors, which were measured at different streptavidin concentrations ($n_{streptavidin}$ = 0, 1, 4, 20, 100, and 300 fM). At $n_{streptavidin}$ = 1 fM, *t*-dependent I_{DS}-V_G curves of the MoS_2 FET sensor were measured with positive and negative V_G sweep directions, respectively.

It should be noted that for the $n_{streptavidin}$ = 0 case (Figure 2.4 (a)), although no any specific binding reaction is expected, the *t*-dependent I_{DS}-V_G curves of the FET sensor still exhibit an observable reduction of the g_m (or I_{DS}) in the linear regime with increasing

t. This indicates that the pure buffer solution still results in moderate nonspecific absorption of ions or molecules on the MoS_2 channel. Currently, we have not fully understood the mechanism of such nonspecific absorption, but temporarily attributed it to the slow reaction between the crystal defects (*e.g.*, S-vacancies) on the MoS_2 channel and the ions in the buffered solution [76].

Figure 2.4 (b) specifically shows the *t*-dependent I_{DS}-V_G curves measured from the MoS_2 sensor subjected to $n_{streptavidin}$ = 1 fM. For this sensor, at each IFDM cycle (*i.e.*, at each *t* point), two I_{DS}-V_G curves were acquired with different V_G sweep directions. One was measured with positive V_G sweep direction (*i.e.*, from -100 to 100 V, which is referred to as the "positively-scanned curve"), and the other was measured with negative V_G sweep direction (*i.e.*, from 100 to -100 V, which is referred to as the "negatively-scanned curve"). Figure 2.4 (b) shows that the MoS_2 sensor exhibits a prominent hysteretic behavior in its transfer characteristics. Such a hysteretic behavior is attributed to the V_G-modulated charge trapped at MoS_2/dielectric interfaces or moisture molecules [68, 77]. Although both sets of the positively and negatively-scanned I_{DS}-V_G curves measured from this sensor exhibit similar g_m/I_{DS}-reduced response behaviors with increasing accumulative incubation time *t*, the observed hysteresis of I_{DS}-V_G curves could result in undesirable indeterminacy of sensor readings for biomolecule quantification. Specifically, to quantify the time-dependent reaction kinetics of an analyte-receptor binding reaction, the I_{DS} values measured at given V_G or the g_m values measured in the linear regime of the I_{DS}-V_G curves are captured and plotted as a function of accumulative incubation time *t*. The hysteretic effect makes the acquired I_{DS}-*t* or g_m-*t* response curves highly dependent on the loading history of V_G biases, resulting in serious inaccuracy of sensor readings for real-time biomolecule quantification. As discussed in introduction, this hysteretic effect is indeed a generic issue for current FET biosensors made from emerging low-dimensional nanomaterials [78-79]. Additional materials processing techniques are needed to form high-quality interfaces between such nanomaterials and other dielectrics to minimize charge-trapping effects. However, as implied by Figure 2.4 (b), an expedient solution to minimize the hysteresis-induced indeterminacy of sensor readings is to use the I_{DS} data measured in the highly conductive regime of I_{DS}-V_G curves (*e.g.*, V_G = 100 V for our n-type MoS_2 FETs) as the sensor response signals. The $I_{DS} - t$

response signals captured at V_G = 100 V is expected to enable reliable quantification of the time-dependent kinetics of analyte-receptor binding reactions with the minimal hysteresis-induced sensor inaccuracy. Here, it should be noted that the IFDM cycle-wise method is highly compatible with the acquisition of $I_{DS} - t$ response signals at V_G = 100 V, because in an IFDM cycle, the electrical measurement of I_{DS}-V_G curves in the V_G range of -100 to 100 V is separated from the incubation in the liquid solution, which can effectively avoid the large-bias-induced electrochemical damage to the FET. This is an advantage of the IFDM cycle-wise method in minimizing or eliminating hysteresis-induced inaccuracy of sensor readings.

As discussed for Figure 2.4, $I_{DS} - t$ response signals can be captured from the highly-conductive n-type branches (or the regimes around V_G = 100 V) of the $I_{DS} - V_G$ curves of MoS_2 FET sensors. To further minimize the fabrication-process-induced device-to-device variation in captured I_{DS} values, we use the relative percentage change in I_{DS} (*i.e.*, $S = 100\% \times [I_{DS}(t) - I_{DS}(t=0)]/I_{DS}(t=0)$) with respect to the accumulative incubation time (t) as a calibrated time-dependent sensor response signal. Here, S can also serve as the measure of the biodetection sensitivity. Figure 2.5 (a) plots the $S - t$ response curves corresponding to different streptavidin concentrations ($n_{streptavidin}$ = 0, 1, 4, 20, 100, and 300 fM), which were captured from the corresponding t-dependent I_{DS}-V_G curves displayed in Fig. 4. The nonflat S-t curve at $n_{streptavidin}$ = 0 serves as the biodetection baseline. The S-t curve measured at $n_{streptavidin}$ = 1 fM can be well resolved from this baseline. This demonstrates that the few-layer-MoS_2 FET sensors operated by the IFDM cycle-wise method can enable a LOD of at least 1 fM for streptavidin detection. In Figure 2.5 (a), the $S - t$ response curves labelled with "1 fM (+)" and "1 fM (-)" are captured from the positively and negatively-scanned t-dependent I_{DS}-V_G curves shown in Figure 2.4 (b) (captured at V_G = 100 V), respectively. These two $S - t$ response curves obtained from the highly conductive n-type regimes of I_{DS}-V_G curves are highly consistent with each other regardless of the scanning direction (or the loading history of V_G-modulated charges). This further demonstrates that the IFDM cycle-wise method can generate unambiguous time-dependent sensor response signals for quantifying the kinetics of binding reactions and rule out the indeterminacy of sensor readings due to the hysteresis of the transfer characteristics of TMDC-based FET sensors.

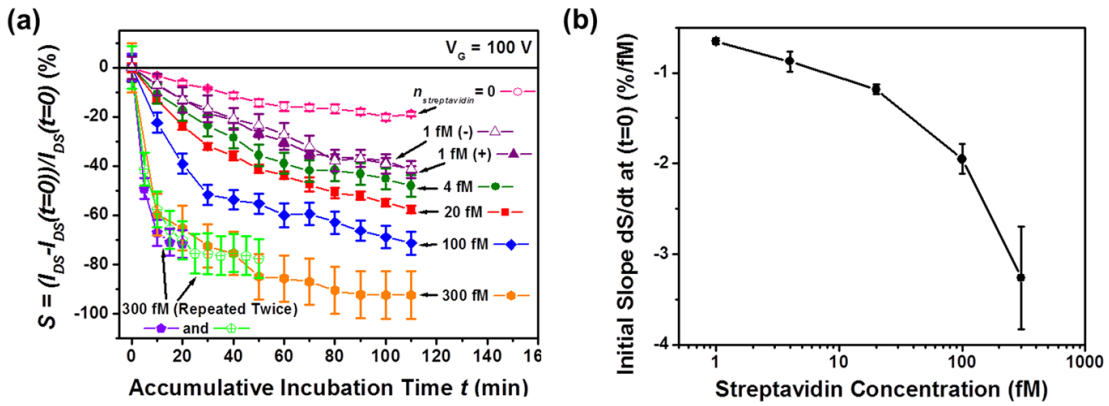

Figure 2.5 (a) S – t response curves measured at different streptavidin concentrations ($n_{streptavidin}$ = 0, 1, 4, 20, 100, and 300 fM), which are captured from the t-dependent I_{DS} – V_G curves of a set of MoS_2 sensors; (b) plots the dS/dt - $n_{streptavidin}$ curves extracted from the S – t response curves.

We further attempted to extract derived sensor response parameters from the measured S – t response curves to obtain a standard curve (*i.e.*, calibrated sensor response (R) *versus* analyte concentration (n) curve) for enabling rapid biomolecule quantification at femtomolar levels. Figure 2.5 (a) shows that within an accumulative incubation time (t) of ~2 hr, the S-t response curves measured at $n_{streptavidin}$ < 300 fM do not fully saturate to the S values corresponding to the equilibrium states of the binding reaction processes at these femtomolar-level concentrations. This means that the sensor response quantities measured at the equilibrium states of the binding reactions are not suitable for rapid femtomolar-level biomolecule quantification, because even for the analyte-receptor pair with a strong affinity (*e.g.*, streptavidin-biotin pair), it still takes several hours for the binding reaction at a femtomolar-level analyte concentration to reach to the equilibrium state. Figure 2.5 (a) also shows that the initial slopes of S – t response curves exhibit a strong dependence on streptavidin concentrations and can be exploited for rapid streptavidin quantification. The determination of such initial slopes of S – t curves does not need a long accumulative incubation time until the analyte-receptor binding reaction reaches to the equilibrium state. Therefore, the initial slope of an S – t curve (*i.e.*, dS/dt at $t \sim 0$) can serve as a derived sensor response quantity for enabling rapid biomolecule quantification. Here, the specific dS/dt value is extracted from the S – t response curve

through linearly fitting the *S* data measured within the first three IFDM cycles (typically, the accumulative incubation time is ~20 min, and the total assay time is less than 23 min). Figure 2.5 (b) plots the dS/dt - $n_{streptavidin}$ curve extracted from the $S - t$ response curves shown in Figure 2.5 (a). Such a dS/dt - $n_{streptavidin}$ curve can serve as a standard curve for rapid streptavidin quantification.

To evaluate the repeatability of biomolecule quantification based on initial varying slopes of $S - t$ response curves, another two MoS_2 FET sensors fabricated in a different batch were used to repeat the cycle-wise detection course at $n_{streptavidin}$ = 300 fM and generate another two $S - t$ response curves, which are also plotted in Figure 2.5 (a). The corresponding *t*-dependent I_{DS}-V_G curves of these two sensors are shown in Figure 2.6. All three $S - t$ response curves (two newly measured curves plus the previously measured one) for $n_{streptavidin}$ = 300fM are consistent with each other. Especially, their initial slopes are very close (the relative standard deviation is ~16%) and can be unambiguously associated with 300fM streptavidin. In addition, for these two repeated courses, the incubation time (T_i) in an IFDM cycle is 5 min. As shown in Figure 2.5 (a), the *S*-*t* response curves measured by these two sensors at T_i = 5 min are consistent with that measured at T_i = 10 min. This result also shows that the variation of the IFDM cycle period in the range of 5-10 min does not significantly affect the resulted *t*-dependent sensor response signals.

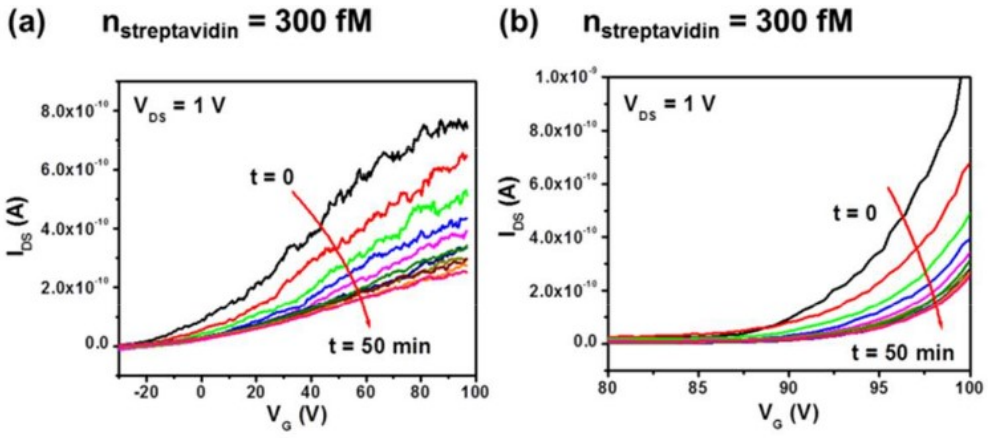

Figure 2.6 *t*-dependent $I_{DS} - V_G$ characteristic curves of two MoS_2 FET sensors, which were measured by using IFDM cycle-wise method at $n_{streptavidin}$ = 300 fM.

For these two repeated detection courses, the incubation time (T_i) in an IFDM cycle is set to 5 min.

2.3.2 Quantification of Interleukin-1 beta (IL-1β) Biomarker Using MoS_2 FET Biosensors Operated by IFDM Cycles

We further used our MoS_2 FET sensors, the IFDM cycle-wise method, as well as the analysis method discussed above for investigating the quantification of other clinical biomarkers, which usually exhibit a much weaker affinity to their antibody receptors in comparison with streptavidin. Here, we demonstrated Interleukin 1beta (IL-1β) quantification. IL-1β is a cytokine protein and serves as an important mediator of the inflammatory response [80-83]. It is related to many cellular activities, including cell proliferation, differentiation, and apoptosis [84-86]. IL-1β has a relatively weak affinity to its antibody in comparison with streptavidin (*i.e.*, the affinity constant for the streptavidin-biotin pair $K_{D,\ Streptavidin} \sim 10^{-14}$ M (or 10 fM), and that of the IL-1β-antibody $K_{D,\ IL\text{-}1\beta} \sim 10^{-9}$ M (or 1 nM)). Therefore, rapid fM-level IL-1β quantification is still a challenge (note that IL-1β quantification with LOD of ~10 fM can be realized by using advanced enzyme-linked immunosorbent assays (ELISAs), but such assays need very long processing times) [87-89].

Figure 2.7 displays the *t*-dependent I_{DS}-V_G characteristic curves measured from a set of six MoS_2 FET sensors, which were subjected to a set of pure IL-1β solutions with different IL-1β concentrations (*i.e.*, $n_{IL\text{-}1\beta}$ = 0 fM, 1 fM, 4 fM, 20 fM, 100 fM, and 500 fM), respectively. From these I_{DS}-V_G curves, the corresponding *S*-*t* response curves were extracted at V_G = 100 V and plotted in Figure 2.8 (a). The method for processing the sensing data for IL-1β quantification is the same as that for streptavidin quantification. Here, the *S*-*t* response curve for $n_{IL\text{-}1\beta}$ = 0 is still not flat but is highly consistent with that for $n_{streptavidin}$ = 0. This further indicates that such a zero-concentration *S*-*t* response curve can serve as a generic baseline for quantification of different target molecules in the same solvent. Figure 2.8 (a) shows that the *S*-*t* response curve measured at $n_{IL\text{-}1\beta}$ = 1 fM is significantly distinct from the nonflat baseline measured at $n_{IL\text{-}1\beta}$ = 0. This indicates

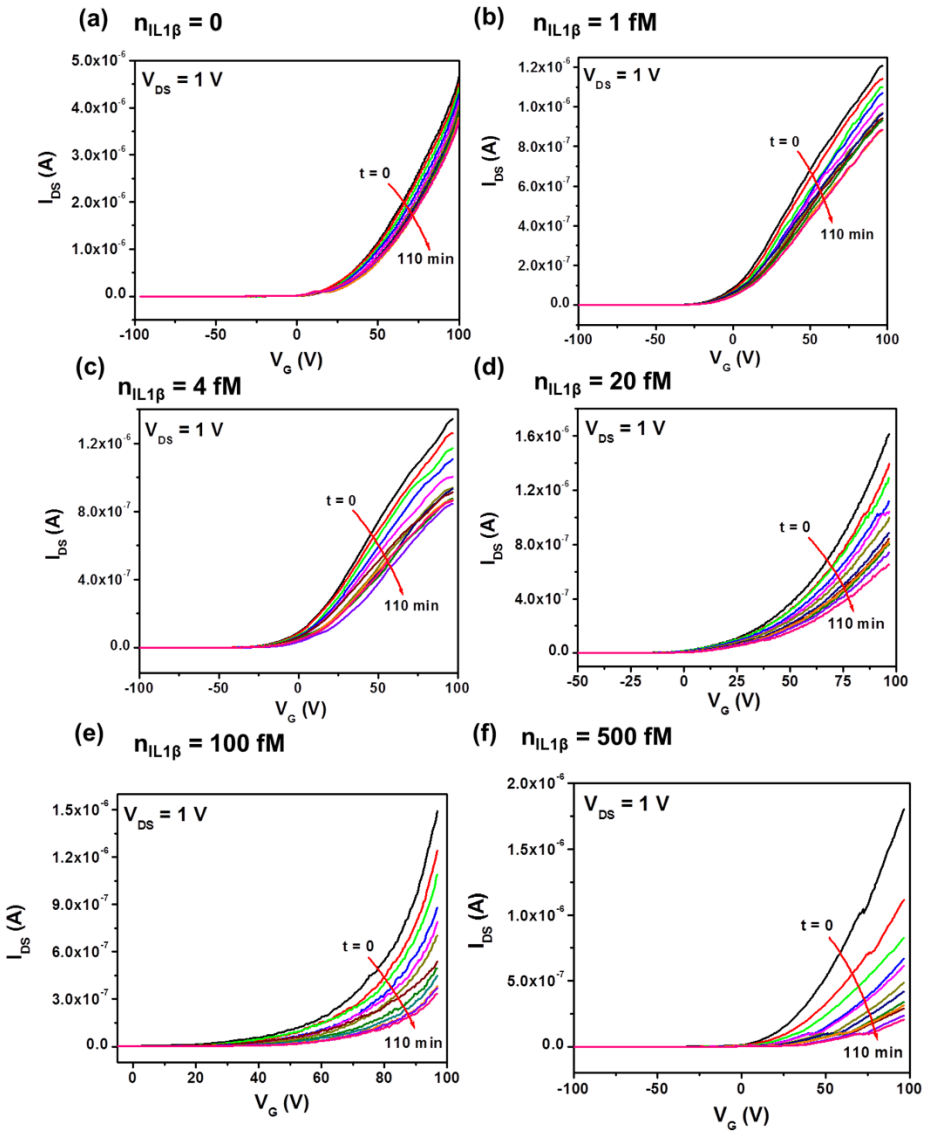

Figure 2.7 SEM images of (a) a HOPG stamp prepatterned with 100 nm half-pitch relief gratings by using nanoimprint lithography followed with plasma etching, and (b) graphene nanoribbons printed onto a plasma-charged SiO2 substrate.

that our MoS_2 FET biosensors in combination with the IFDM cycle-wise method can result in a LOD of ~1 fM for IL-1β quantification. As discussed for streptavidin quantification, the initial slopes of the *S-t* response curves shown in Figure 2.8 (a) can be also used as a derived response quantity for enabling rapid IL-1β quantification. Figure 2.8 (b) shows the extracted *dS/dt* data plotted as a function of the IL-1β concentrations

($n_{IL\text{-}1\beta}$). Similar to the case for streptavidin quantification, to unambiguously determine the *dS/dt* values for IL-1β quantification, the minimum incubation time is about 20 min, and the corresponding total assay time is about 23 min. Therefore, this work has further demonstrated that the MoS_2 FET biosensors operated using the IFDM cycle-wise method can enable rapid femtomolar-level quantification of IL-1β and other biomolecules with relatively weak affinities (*i.e.*, nM-level K_D values) to their receptors.

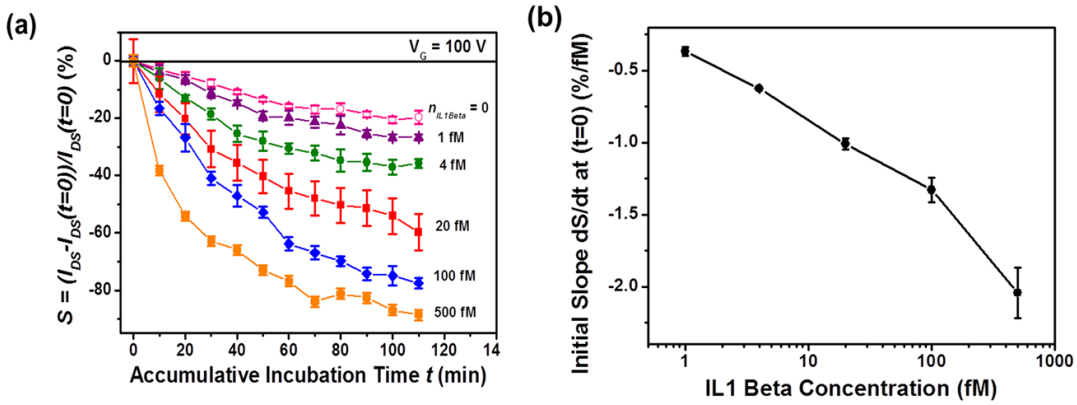

Figure 2.8 (a) $S - t$ response curves measured at different IL-1β concentrations ($n_{IL\text{-}1\beta}$ = 0, 1, 4, 20, 100, and 500 fM), which are captured from the t-dependent $I_{DS} - V_G$ curves of a set of MoS_2 sensors; (b) plots the *dS/dt* - $n_{IL\text{-}1\beta}$ curves extracted from the $S - t$ response curves.

2.3.3 IFDM Cycle-Wise Operation Method for Mitigating Liquid-Solution-Induced Issues

Furthermore, we characterized two MoS_2 FET sensors fabricated in the same batch for a direct comparison of the time-dependent response signals measured using the cycle-wise method and the regular continuous detection method. Figure 2.9 shows these two sensors' responses to the same pure 30 fM streptavidin solution. Figure 2.9 (a) shows the t-dependent $I_{DS} - V_G$ characteristic curves measured using one of the MoS_2 sensors, which was operated using the IFDM cycle-wise method (T_i = 10 min). Figure 2.9 (b) plots the calibrated $S - t$ response signal extracted from these t-dependent $I_{DS} - V_G$ curves shown in Fig. 2.9 (a). The other MoS_2 FET sensor was used to continuously measure the

electrical signal associated with the time-dependent reaction kinetics of biotin-streptavidin binding. In particular, the sensor was continuously biased with a back-gate voltage (V_G) of 100 V and a drain-source voltage (V_{DS}) of 1 V. Since the 30fM streptavidin solution was introduced into the sensor, the instant I_{DS} signal had been being continuously recorded as a function of t. This $I_{DS} - t$ signal was also calibrated into the signal of t-dependent relative change in I_{DS} (*i.e.*, the $S - t$ signal), which was also plotted in Figure 2.9 (b). In comparison with this $S - t$ signal obtained using the continuous detection method, the $S - t$ signal obtained using the IFDM cycle-wise method exhibits the larger signal magnitude (*i.e.*, the higher sensitivity) and the smaller relative error of the signal magnitude (*i.e.*, the higher signal-to-noise ratio) at a given accumulative incubation time. The relatively weaker magnitude of the $S - t$ signal obtained using the continuous method is attributed to the Debye screening effect of the liquid solution, which can weaken the electrostatic coupling between the charges of target molecules and the FET channel, resulting in the lower sensitivity [64-67]. The IFDM cycle-wise method can address this issue through physically isolating the incubation and measurement stages during an IFDM cycle. This cycle-wise method can also eliminate the electrical noise from the liquid solution and therefore result in the lower LOD. Our cycle-wise detection method using MoS_2 FETs results in a much lower LOD in comparison with a standard ELISA. The LOD of the standard ELISA is presented in Figure A.1 in Appendix A. Additionally, as shown in Figure 2.9 (b), the MoS_2 sensor operated using the continuous method failed at $t \sim 50$ min. Our other TMDC FET sensors, when operated using the continuous method, also usually fail within one hour of the operation. Such a poor durability is attributed to the net effect of the electrical stresses continuously applied to the FET channel and the continuous exposure of the sensor to the liquid environment, which can lead to electrochemical or thermal damage to the sensing channel. However, the similar TMDC sensors, if operated using the IFDM cycle-wise method (T_i: 5-10 min), can properly work for several hours (*i.e.*, accumulative incubation times of several hours) without damage. Therefore, this comparison work indicates that the TMDC FET sensors operated using the IFDM cycle-wise method exhibit the better durability, the higher sensitivity, and the higher signal-to-noise ratio in comparison with those operated using the continuous detection method.

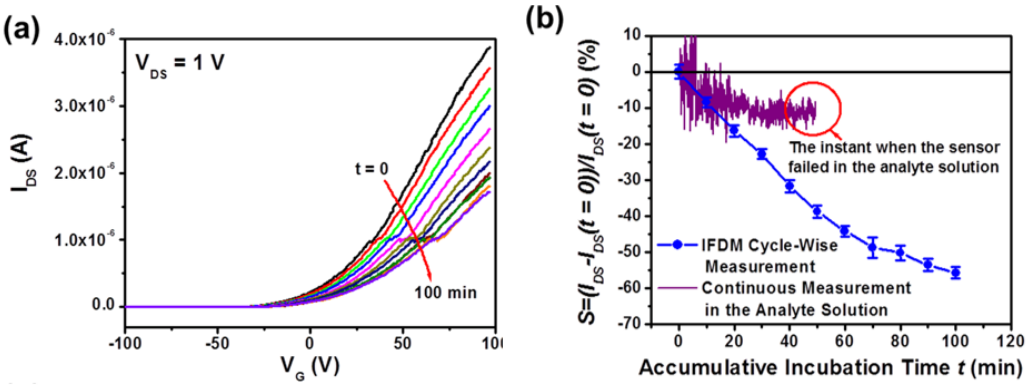

Figure 2.9 Comparison between a MoS_2 FET biosensor operated using the IFDM cycle-wise method and another similar sensor operated using the regular continuous detection method in their responses to a 30 fM solution of pure streptavidin: (a) t-dependent $I_{DS} - V_G$ characteristic curves of the sensor operated using the cycle-wise method; (b) the $S - t$ response signals obtained using the IFDM cycle-wise method (solid circles) and the regular continuous detection method (the solid line).

2.3.4 Detection Specificity of MoS_2 FET Biosensors Operated by the IFDM Method

To evaluate the detection specificity of the MoS_2 FET biosensors operated by the IFDM cycle-wise method as well as the effect of complex solutions on the detection results, we further performed two experiments to study the time-dependent sensor responses to biotin-streptavidin and IL-1β-antibody binding reactions in various solution backgrounds. In the first experiment, we fabricated three MoS_2 FET biosensors in the same batch. One of them (sensors #1) was used to quantify 20 fM streptavidin in a pure solution. The other two sensors (sensors #2 and #3) were used to quantify 20 fM streptavidin in a solution that also contained 60 fM tumor necrosis factor alpha (TNF-α). Figure 2.10 shows the t-dependent $I_{DS} - V_G$ characteristic curves of these three MoS_2 FET sensors, which were measured using the IFDM cycle-wise method (T_i = 10 min).

Figure 2.11 (a) plots three $S - t$ response curves extracted from the t-dependent $I_{DS} - V_G$ curves of these three MoS_2 sensors (all I_{DS} and S data were captured at V_G = 100 V). These three $S - t$ response curves are highly consistent with each other. This indicates that the presence of 60 fM TNF-α in the analyte solution does not noticeably affect the t-dependent sensor responses to 20 fM streptavidin.

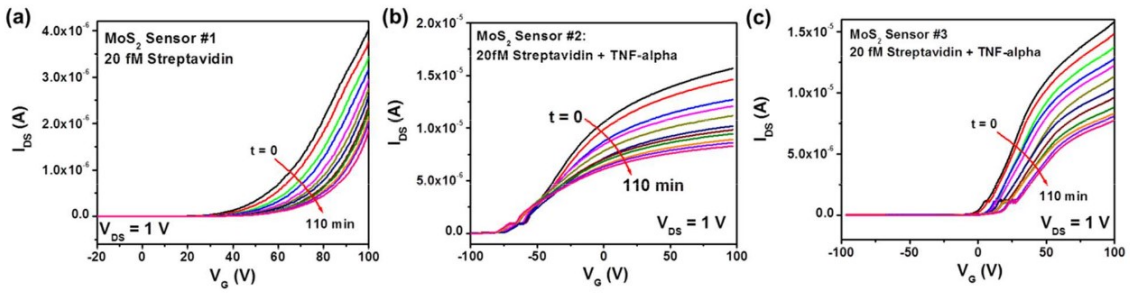

Figure 2.10 IFDM cycle-wise responses (T_i = 10 min) of three MoS_2 FET biosensors that were fabricated in the same fabrication batch: t-dependent $I_{DS} - V_G$ characteristic curves of Sensor #1 (a), which was measured in a pure solution of 20 fM streptavidin, and Sensors #2 (b) and #3 (c), which were measured in a mixed solution containing 20 fM streptavidin and 60 fM tumor necrosis factor alpha (TNF-α).

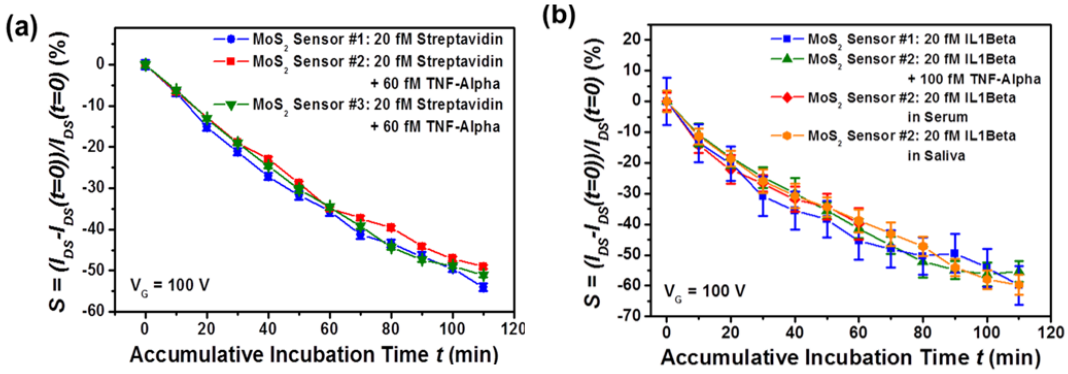

Figure 2.11 Sensor responses to targeted streptavidin and IL-1β molecules in different solution backgrounds: (a) $S - t$ responses, measured from three MoS_2 FET sensors, to 20 fM streptavidin in a pure solution (Sensors #1) and a solution also containing 60 fM TNF-α (Sensors #2 and #3); (b) $S - t$ responses, measured from four MoS_2 FET sensors, to 20 fM IL-1β in a pure solution (Sensor #1), a solution also containing 100 fM TNF-α (Sensor #2), serum (Sensor #3), and human saliva (Sensor #4).

In the second experiment, four MoS_2 FET biosensors were fabricated and used to quantify 20 fM IL-1β in a pure solution (sensor #1), a solution also containing 100 fM TNF-α (sensor #2), serum (sensor #3), and saliva (sensor #4), respectively. The serum matrix used here was purchased from Merck KGaA, Inc. and diluted by 20 times in DI water. It contains 0.08% Sodium Azide. The saliva used here was collected from healthy

human donors using reported drooling method [90]. The as-pooled saliva was diluted in DI water by 10 times. Figure 2.12 shows the *t*-dependent $I_{DS} - V_G$ curves of these four MoS_2 FET sensors, which were measured using the IFDM cycle-wise method (T_i = 10 min).

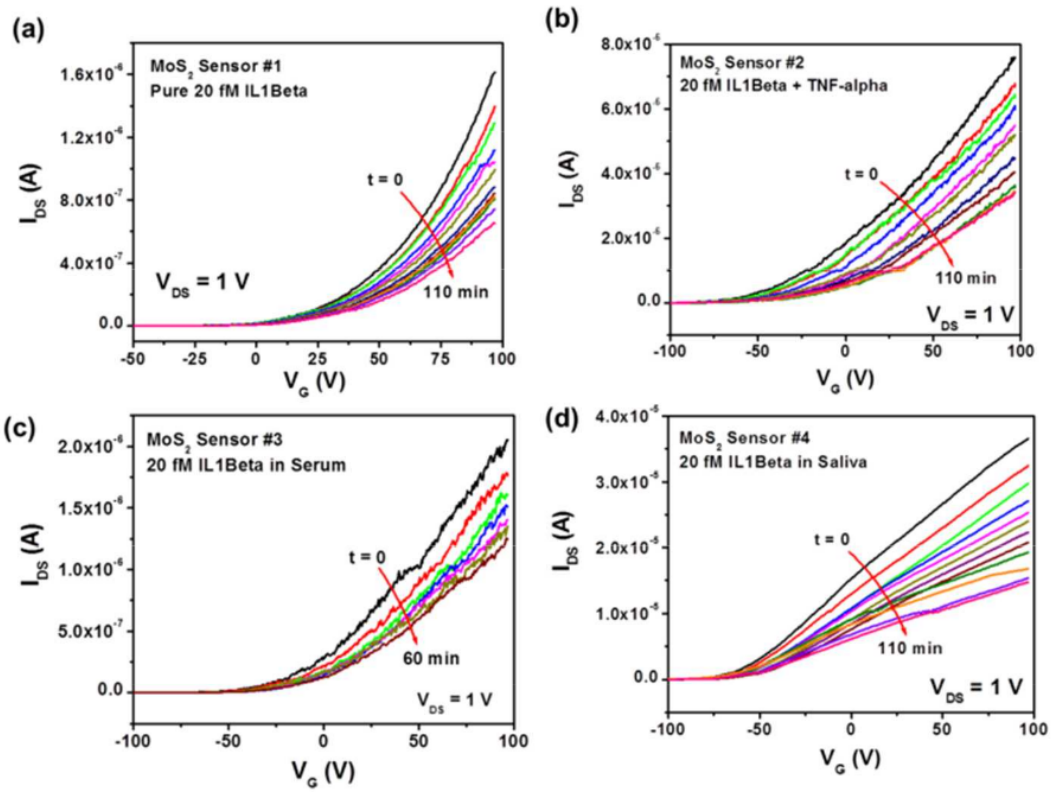

Figure 2.12 IFDM cycle-wise responses (T_i = 10 min) of four MoS_2 FET biosensors that were fabricated in the same fabrication batch: *t*-dependent $I_{DS} - V_G$ characteristic curves of Sensor #1 (a) that was measured in a pure solution of 20 fM IL-1β, Sensor #2 (b) that was measured in a mixed solution containing 20 fM IL-1β and 100 fM tumor necrosis factor alpha (TNF-α), Sensor #3 (c) that was measured in a serum solution containing of 20 fM IL-1β, and Sensor #4 (d) that was measured in a saliva solution containing of 20 fM IL-1β.

Figure 2.11 (b) plots the $S - t$ response curves extracted from the *t*-dependent $I_{DS} - V_G$ curves of these four MoS_2 sensors (all I_{DS} and S data were captured at V_G = 100 V). All of these *S*-*t* signals in response to 20 fM IL-1β in different solution backgrounds are consistent with each other. This good consistency further demonstrates that the reliable *t*-dependent sensor responses to target analyte molecules (*i.e.*, 20 fM IL-1β) can be

acquired regardless of the different solution backgrounds, and the complex protein backgrounds in serum and saliva do not significantly affect the *t*-dependent sensor readings associated with the specific concentrations of target molecules. The slight difference among these $S - t$ curves in Figure 2.11 (a) and (b) is attributed to the slight sensor-to-sensor variation in transport characteristics. These two comparison experiments have demonstrated that the MoS_2 FET biosensors operated using the IFDM cycle-wise method exhibit a high biodetection specificity. This is attributed to the flushing step in an IFDM cycle, which can effectively remove non-specifically adsorbed molecules from the FET sensing channel, therefore minimizing the false sensor responses. Furthermore, two-dimensional MoS_2 or other TMDC surfaces usually have a very low friction coefficient and exhibit very low adhesion to other materials, which is expected to make the flushing of non-specifically adsorbed molecules on TMDC FET channels much easier than that on the FET channels made from conventional semiconductors [91].

2.4 Summary

In summary, we established a cycle-wise approach for operating MoS_2 FET biosensors. This approach enabled rapid, low-noise, highly specific biomolecule quantification and analyte-receptor binding kinetics analysis. This detection process utilized a microfluidic structure to deliver a time-sequenced series of reagent fluids to the MoS_2 FET channel. Periodically delivering the reagent fluids into the device resulted in assay cycles, each with four stages: incubation, flushing, drying, and measurement (*i.e.*, IFDM cycles). This process can measure time-dependent sensor responses to analyte-receptor binding reactions. This cycle-wise approach can physically separate incubation, flushing, and electrical measurement steps from each other in the time sequence. Thus, it can prevent liquid-solution-induced electrochemical damage, electronic noise, signal screening, and nonspecific adsorption, therefore improving the sensors' durability, detection limit, sensitivity, and specificity. Combined with the high sensitivity and low detection limit of MoS_2 FET biosensors, this cycle-wise detection method can realize rapid biomolecule quantification at femtomolar levels. In this work, we have

demonstrated the quantification of streptavidin and IL-1β suspended in pure and complex solutions (*e.g.*, serum and saliva) with a detection limit of ~1 fM and a total assay time less than 23 min). In comparison with previously reported FET biosensors made from graphene layers [92], Si nanowires [93-94], and MoS_2 layers [35, 95], our MoS_2 sensors operated by the cycle-wise detection method enable a lower LOD for quantifying low-abundant biomolecules. For femtomolar-level IL-1β quantification, our IFDM cycle-wise method can result in a much shorter required incubation time in comparison with advanced ELISA [96-98]. The comparison parameters (LODs and incubation time) are provided in Table A.1 in Appendix A. This work leverages the superior electronic properties of emerging layered semiconductors for label-free biosensing applications and advances the sensor operation technology toward realizing fast real-time biomolecule quantification at femtomolar levels. In addition, the presented cycle-wise method could be generally applied to other nanoelectronics-based biological and chemical sensors while overcoming the issues resulting from poor compatibility between reagents and electrical detection processes in a fluidic environment.

Chapter 3

Bio-Tunable Nanoplasmonic Filter on Few-Layer MoS_2 for Rapid and Highly Sensitive Cytokine Immunosensing

3.1 Introduction

Cytokines are key biomolecules acting as mediators and modulators of the complex functional interactions and responses of the immune systems [99-101]. Quantifying cytokines allows monitoring of immune responses, providing clinically and immunologically useful information related to infectious diseases, cancer, autoimmune diseases, allergy transplantation, and drug discovery [102]. There has been an explosion in the use of cytokine-targeting immunotherapies for treating autoimmune diseases, infection [103], cancer [104], and other immune-related deficiencies [105-106]. Establishing a normal balance of a cytokine network in the host, these therapies have shown great promise for treating inflammatory diseases [107-108]. In treatment of a systemic inflammatory disorder, rapid and sensitive profiling of the cytokine-mediated immune response is required for realizing timely personalized immunomodulatory drug delivery to a critically ill patient. However, in conventional enzyme-linked immunosorbent assay (ELISA) and bead-based immunoassay processes, the sensing signals are detected either by microplate readers or flow cytometers, which need very long (normally 3-8 hours) and complicated assay processes. These assay techniques preclude researchers from analyzing inflammatory biomarker profiles and host-defense

responses in real time during the course of disease development [109-113]. Recently, a great deal of research efforts has been made to address this challenge. These efforts include nano/microscopic biosensing methods based on localized surface plasmon resonance (LSPR) [44, 114-115], nano-enzyme-linked immunosorbent assay (Nano-ELISA) [42, 116], micro-particle control [117] and so on. Nevertheless, these state-of-the-art methods still fall short of achieving high sensitivity and speed simultaneously in cytokine detection.

Owing to their attractive electronic/optical properties, large abundance, and compatibility to planar nanofabrication processes, atomically layered semiconducting materials, such as MoS_2, WSe_2, and WS_2, have recently garnered much attention as promising candidates for development of high-performance field-effect transistors (FETs) and other relevant nanoelectronic devices [118-120]. The transport characteristics of monolayer or few-layer MoS_2 FET channels are extremely sensitive to the external stimuli and can be exploited to make biosensors with high sensitivity and fast response speed [121-122]. Electrical response characteristics of such MoS_2 FET devices have been used to create ultrasensitive biosensors capable of detecting antigen-antibody binding events [123-124]. However, such purely electrical and electronic biosensors still suffer from degradation of detection stability and sensitivity over a long incubation time, which is attributed to ionic screening of electric field and unwanted short-circuit effects in an aqueous environment [125-128]. Specifically, the ions in an aqueous solution and other heterogeneous liquid components could result in serious shorting of electric circuits and distract electron current distribution in the presence of direct contact between the biomolecules and transistor regions. In this regard, alternative sensing mechanisms are needed to prevent the MoS_2-based sensing component from directly contacting with liquid reagents.

In this chapter, we explore a cytokine biosensing approach based on a MoS_2 photoconductive device that is highly sensitive to light transmission through a biomolecule-capturing nanoplasmonic optical filter. In recent study, photodetectors consisting of a MoS_2 layer-based photoconductive channel have been demonstrated as ultrasensitive photo-response devices [124, 129-130]. Our approach allows us to take full advantage of high photo-absorption coefficients resulting from the atomically layered

structure of MoS_2 while avoiding the above-described contact of the photoactive structures with aqueous reagents. This study develops an integrated immunosensor device with a decoupled design that eliminates electron transfer between a nanoplasmonic structure and an atomically layered MoS_2 photodetector under light illumination to achieve highly sensitive, rapid, and stable cytokine detection. The nanoplasmonic optical filter of the device is an optically transparent SiO_2 layer (170 μm) coated with spherical gold nanoparticles (AuNPs; d = 50nm). Light trapping by the AuNPs due to localized surface plasmon resonance (LSPR) results in an efficient nano optics filtering effect under resonant light illumination (λ = 532nm). We find that the biosensor device enables us to detect a pro-inflammatory cytokine, IL-1β, at a concentration as low as 250 fg/mL (14 fM) with a sampling-to-answer time of ~10 min. We anticipate that such a LSPR-modulated optoelectronic biosensor can find a wide range of applications, including point-of-care disease diagnosis, and environmental monitoring.

3.2 Experimental Setup of Bio-Tunable Nanoplasmonic Biosensors

3.2.1 Fabrication of Gold Nanoparticle Arrays on a SiO_2 substrate (Nanoplasmonic Filter) and Functionalization Process

To prepare the gold nanostructure, we centrifuged gold nanospherical particle (AuNP) and gold nanorod (AuNR) stock solutions (0.2 nM) three times at 5000 rpm for 10 min, and washed them in D.I. water to remove excessive structure direction agents (citrate for AuNP and cetrimonium bromide (CTAB, Cetyltrimethylammonium bromide) for AuNR) in the solutions. As a substrate, we used thin SiO_2 layer (100um). The SiO_2 substrate was rinsed with acetone, isopropanol and DI water. Piranha clean with a solution of H_2SO_4:H_2O_2 = 3:1 v/v was followed for 30 min. The SiO_2 substrate was washed with D.I. water carefully. After drying, the surface of the SiO_2 substrate was treated by O_2 plasma for 2 min at 18 W (COVANCE 1-MP, Femto). Then the number of hydroxyl groups on the SiO_2 substrate can be created on the surface. Then the SiO_2 substrate was incubated in a 0.1M (3-Aminopropyl) triethoxysilane (APTES) solution for

6hrs. The AuNP (or AuNR) solution was then loaded into a chamber and incubated overnight. The inlets and outlets were sealed with a cover glass to prevent evaporation and avoid dry-out of the AuNP (or AuNR) solution during incubation. After the incubation, the AuNPs- SiO_2 (or AuNR- SiO_2) substrate was washed with DI water and strong air blowing was followed (Figure 3.1).

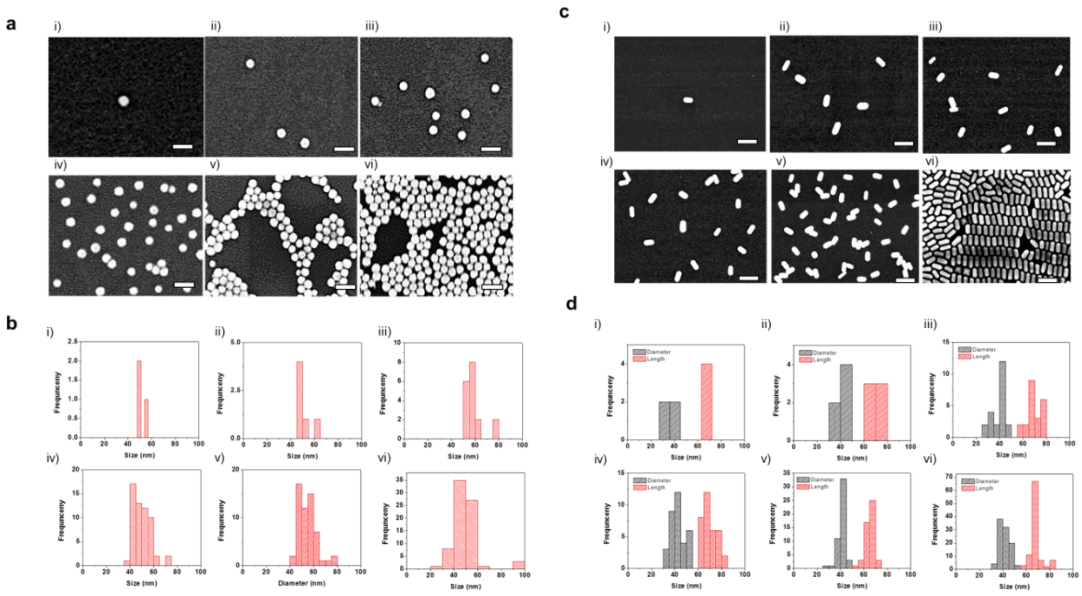

Figure 3.1 Scanning electron microscopy (SEM) images of gold nanospherical particles (AuNPs) and gold nanorod particles (AuNRs) with varying particle density on SiO_2 substrate. (a) SEM images of AuNPs, (b) particle size distribution of AnNPs, with i) 5 particles/μm^3 , ii) 25 particles/μm^3, iii) 50 particles/μm^3, iv) 125 particles/μm^3, v) 250 particles/μm^3, and vi) 1000 particles/μm^3, (c) SEM images of AuNRs, and (d) particle size distribution of AuNRs with i i) 5 particles/μm^3 , ii) 25 particles/μm^3, iii) 50 particles/μm^3, iv) 125 particles/μm^3, v) 250 particles/μm^3, and vi) 1000 particles/μm^3.

After preparation of the AuNP (or AuNR) array on the SiO_2 substrate, functionalization of thiolated alkane 10-Carboxy-1-decanethiol (HS-(CH_2)10-COOH) using a self-assembly method (SAM) was followed. At first, the SiO_2 substrate was incubated in 1mM of thiolated alkane 10-Carboxy-1-decanethiol (HS-$(CH_2)_{10}$-COOH) overnight. Then the formed carboxylic group (-COOH) on the AuNP surface enabled us to attach a linker for antibody. The antibody linking was performed by way of the antibody binding to the –COOH functional group through standard 1-ethyl-3-[3-

dimethylaminopropyl] carbodiimide / N-hydroxysuccinimide (EDC / NHS) coupling chemistry. After washing the –COOH formed AuNP (or AuNR)–SiO_2 substrate, we loaded a mixture of 0.4 M EDC and 0.1 M NHS at a 1:1 volume ratio in a 0.1 M EDC solution into the chamber to activate the AuNP (or AuNR) array surfaces on the SiO_2 substrate. Then, to attach the antibody, we prepared diluted primary cytokine antibodies from 100 to 10 μg/mL in 1x PBS. We loaded the prepared antibody solution into the chamber and incubated it at room temperature for 60 min. To suppress the non-specific binding on the detection surface, we treated the prepared Anti-AuNP (or Anti-AuNR) conjugates with 10μL of 1% BSA in 1x PBS in blocking buffer and incubated the whole system for 20 min. Before detecting cytokines, the Anti-AuNP (or Anti-AuNR) array surface was thoroughly washed to remove any excessive solutions or molecules using 20μL of 1x PBS.

3.2.2 Fabrication of a Highly Sensitive Few-Layer MoS_2 Photodetector

The few-layer MoS_2 thin-film transistors were fabricated using a micro printing method [130]. Flake MoS_2 channel thicknesses were specifically controlled to be 15–20 nm. Such a MoS_2 thickness range has been demonstrated to result in the optimal field-effect mobility values for MoS_2 transistors. The transistor channel lengths (L) were ~10 μm and the channel widths (W) ranged from 5 μm. Ti (5 nm)/Au (50 nm) electrode pairs served as drain (D) and source (S) contacts, which were created using photolithography followed by metal deposition and lift-off. Such thin SiO_2 layers can enable a simple color-coding method whereby MoS_2 flakes with suitable thicknesses (*i.e.*, 15–20 nm) may be quickly identified.

3.2.3 Integration of a Nanoplasmonic Filter and a Few-Layer MoS_2 Photodetector

After separately preparing a AuNP/SiO_2 nanoplasmonic optical filter thin layer and an atomically layered MoS_2 photodetector, we assembled them into the same device platform (Figure 3.2). Using macro manipulation control, we placed the AuNP/SiO_2 on

Au electrode of MoS_2 detection platform. Along the alignment marks in both SiO_2 substrates of Au/SiO_2 and MoS_2/SiO_2, we made constant location between nanoplasmonic filter and MoS_2 photodetector. To avoid any alignment change, the nanoplasmonic optical filter and MoS_2 photodetector were physically bonded using a dielectric sticky PDMS thin (0.5 mm) handling layer.

Figure 3.2 (b) shows a cross-sectional view of the whole decoupled device architecture, where the nanoplasmonic filter and few-layer MoS_2 flake are physically decoupled by an intermediate SiO_2 thin layer with an air gap. This decoupled architecture ensures non-physical contact between the plasmonic nanostructure and semiconducting structures while other previous device structures incorporated a metal / semiconductor interface.[131] In general, at the metal / semiconductor interface, it is well known that electron transfer takes place between the plasmonic nanostructure and the few-layer MoS_2 flake due to band gap bending. The metal / semiconductor contact device architecture allows direct interaction between plasmonic nanostructure/ few-layer MoS_2 and biomolecules in an aqueous solution, which leads to non-uniform surface charge distribution and signal instability. In our decoupled architecture, electron transfer causing irradiative plasmon decay is minimized. As such, radiative decay of plasmons in the nanoplasmonic structure only determines the sensitivity of few-layer MoS_2 while maintaining high stability of the electrical signal.

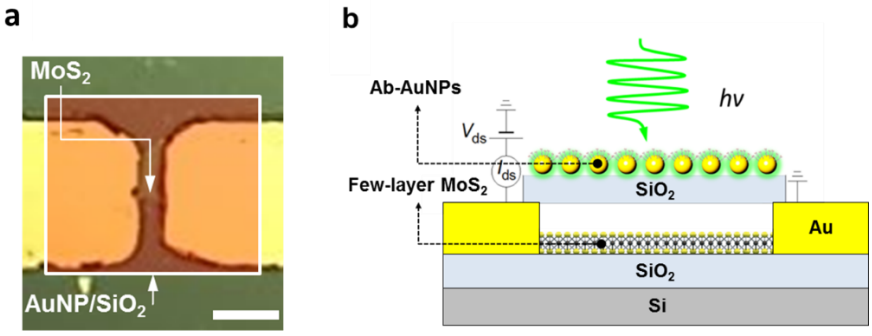

Figure 3.2 Bio-tunable nanoplasmonic filter on few-layer MoS_2 photodetector. (a) Optical microscope image of the decoupled AuNP/SiO_2 and MoS_2 photodetector (scale bar = 20 μm). (b) Schematic image of the structure of the assembled device.

3.3 Experimental Results

3.3.1 Detection Scheme of a Nanoplasmonic Integrated MoS_2 Optoelectronic Biosensor

Figure 3.3 illustrates the underlying concept of hybrid integration of a AuNP-SiO_2 nanoplasmonic filter layer and a few-layer MoS_2 photoconductive flake on a common device platform for cytokine detection. The AuNPs (d = 50nm) on the SiO_2 layer are coated with antibodies (Ab) specifically targeting IL-1β. In the absence of the targeted cytokine (IL-1β) molecules, the Ab coated-AuNPs blocks incident light at $\lambda = \sim 532$ nm as a result of the LSPR effect ("OFF" mode). In the OFF mode, light transmission through the SiO_2 layer becomes weak, keeping incident light from reaching the underlying few-layer MoS_2 photoconductive flake. Now, binding of IL-1β molecules onto the Ab-coated AuNP surfaces shifts the plasmonic resonance wavelength owing to a change in the local refractive index near the AuNP surfaces [44, 114-115]. A larger fraction of the incident photons then transmits through the SiO_2 thin layer and reaches the underlying MoS_2 photoconductive flake ("ON" mode). The ON mode results in a red shift of the extinction spectrum peak of the AuNP-SiO_2 nanoplasmonic filter layer, thus leading to an increased photoconduction of the MoS_2 flake. The photoconduction of the device is determined by the cytokine concentration of a sample solution deposited on the device surface covered with the AuNP-SiO_2 thin layer. Obtaining a correlation between the photoconduction change and the cytokine concentration allows highly sensitive quantification of IL-1β.

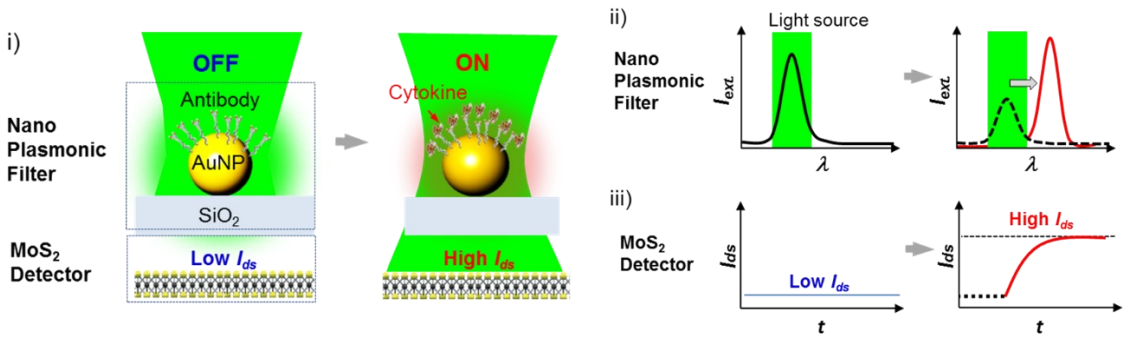

Figure 3.3 Schematic of decoupled nanoplasmonic filter on few-layer MoS_2 sensor for cytokine detection. i) An antibody-attached plasmonic gold nanoparticle (AuNP [d = 50nm]) resonates with incident light at λ = 532 nm. The resonance induces strong extinction around the Antibody(Ab)-AuNP on SiO_2. Due to the strong extinction, limited power density of incident light is delivered to the few-layer MoS_2 flake, which results in lower photocurrent in MoS_2. When cytokines bind to the antibodies on the AuNP selectively, there is a change in the local refractive index. This local refractive index change decreases resonance between the cytokine-antibody-AuNP and the incident light. A larger portion of light-power density can be delivered to the MoS_2 film sensor. ii) The extinction of the AuNP is matched to the incident light. Local refractive index change based on cytokines binding on the antibody-AuNP leads to a shift of the extinction peak. The extinction peak and wavelength of the incident light are no longer matched. iii) Resonance between plasmonic extinction of the antibody-AuNP and the incident light source induces a decrease in the amount of the incident light detected in MoS_2. The extinction peak shift leads to a higher amount of the incident light detected.

3.3.2 Comparison of Nanoplasmonic Filtering Effects Between Gold Nanospheres (AuNPs) and Gold Nanorods (AuNRs)

We first tested the impact of LSPR on the nanoplasmonic filtering effect of our device using gold nanospherical particles (AuNPs) and gold nano nanorod particles (AuNRs) on a SiO_2 thin layer. The SiO_2 layer was placed on two electrodes adjacent to a few-layer MoS_2 photoconductive film, which were connected to electronics used to characterize the device. One of the gold electrodes acting as a drain was connected to a voltage source while the other, the source electrode, was grounded. The testing structures were prepared by attaching nanoparticles to a 3-Aminopropyl triethoxysilane (APTES)-functionalized SiO_2 thin layer with an amino functional group. The resulting AuNP and

AuNR structures on the SiO_2 thin layer revealed uniform color over ~ 5 mm^2 area samples, which suggested uniform distribution of the nanoparticles on the surface. The morphology and optical property of each testing structure were analyzed by scanning electron microscopy (SEM), and ultraviolet-visible (UV-VIS) spectrometer. We verified that a monolayer of AuNPs or AuNRs was uniformly distributed on the SiO_2 thin layer without aggregations for each structure. Same particle density of the AuNPs and AuNRs (Figure 3.4 (b), $d_{particle}$ = ~ 125 particles / μm^3) were tested.

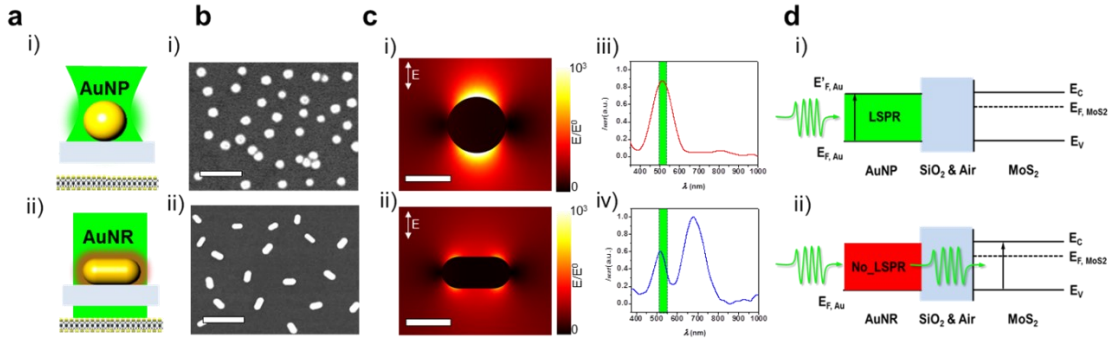

Figure 3.4 Localized surface plasmon resonance (LSPR) induced selective photo-enhancement effect on AuNP nanoplasmonic filter and MoS_2 photodetector. (a) Plasmonic resonance induces optical filtering effects. The selective photodetection based on plasmon resonance is verified by comparison between i) gold nanosphere- (AuNP [d = 50nm]) and ii) gold nanorod (AuNR [d /l = 40/68 nm])-coated SiO_2 layers. (b) Scanning electron microscopy (SEM) image of AuNP and AuNR arrays on SiO_2 (scale bar = 500 nm), (c) Calculated electric field distribution based on finite element analysis (FEA) reveals high extinction for i) the AuNP and lower extinction for ii) the AuNR with incident light at λ = 532 nm. Extinction peak of iii) the AuNP located at ~ 532 nm and extinction peaks of iv) the AuNR located at 530 nm and 670 nm. Under the light source at λ = 532 nm, the AuNP leads to lower photocurrent. The AnNR array results in higher photocurrent, (d) Schematic of the optical filtering mechanism through the SiO_2 layer between the AuNP (or AuNR) metal nanostructure and the atomically layered MoS_2 (semiconductor) without bandgap bending; i) A LSPR mode in the metal nanostructure enables filtering of the incident light and ii) No LSPR leads to transmission of photons to the atomically layered MoS_2.

Our system used a visible laser light source at λ = 532 nm ± 10 nm. The fabricated few-layer MoS_2 photoconductive flake shows sufficient photoresponsivity at this wavelength (Figure 3.5). The wavelength λ = 532 nm lies in a biologically benign

optical band. The MoS_2 flake exhibits higher photoresponsivity at shorter wavelengths in the ultraviolet (UV) region but UV light is often harmful to biological systems. The AuNPs (d = 50 nm) exhibit a strong LSPR peak at this wavelength while the primary (longitudinal) plasmonic resonance peak of the AuNRs (d = 40 nm and l = 68 nm) lies at λ = 680 nm, where the MoS_2 flake experiences a significant reduction of photoresponsivity. Choosing the excitation light source wavelength λ = 532 nm also brings a practical benefit that enables us to use AuNPs for the nanoplasmonic optical filter of our device rather than AuNRs. AuNPs are more readily commercially accessible than AuNRs because of their much simpler synthesis requirements and cost effectiveness.

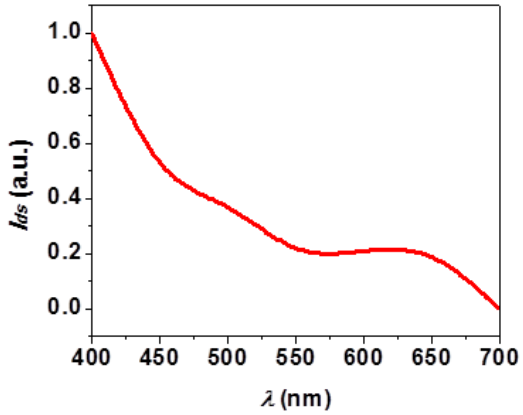

Figure 3.5 Spectral response of the few-layer MoS_2 photoconductive flake. Drain current (I_{ds}) as a function of excitation wavelength of the illumination source normalized by optical power.

Calculated electric field distributions around AuNP and AuNR support the high extinction in AuNP (Figure 3.4 (c)). Then, we hypothesized that the plasmonic filtering effect would cause the AuNPs to yield a lower photocurrent signal in the few-layer MoS_2 flake than the AuNRs (Figure 3.4 (d)). Our photoconduction experiment was performed for devices incorporating the testing structures above (Figure 3.7 (a)). The test obtained a photocurrent of I_{ds} = 0.21 μA at a drain-source voltage of V_{ds} = 1.0 V and I_{ds} = - 0.7 μA at V_{ds} = -1.0 V with the AuNPs, whereas I_{ds} = 0.75 μA at V_{ds} = 1.0 V and I_{ds} = -1.5 μA at V_{ds} = -1.0V with the AuNRs. These experimental results verified our hypothesis, indicating

more significant plasmonic filtering effect with the AuNPs than with the AuNRs, which proves that strong extinction-based resonance between plasmonic nanoparticle and incident light determines the performance of the nanoplasmonic filter. In addition, we controlled the density of AuNPs on SiO_2, expecting that it would tune the filtering

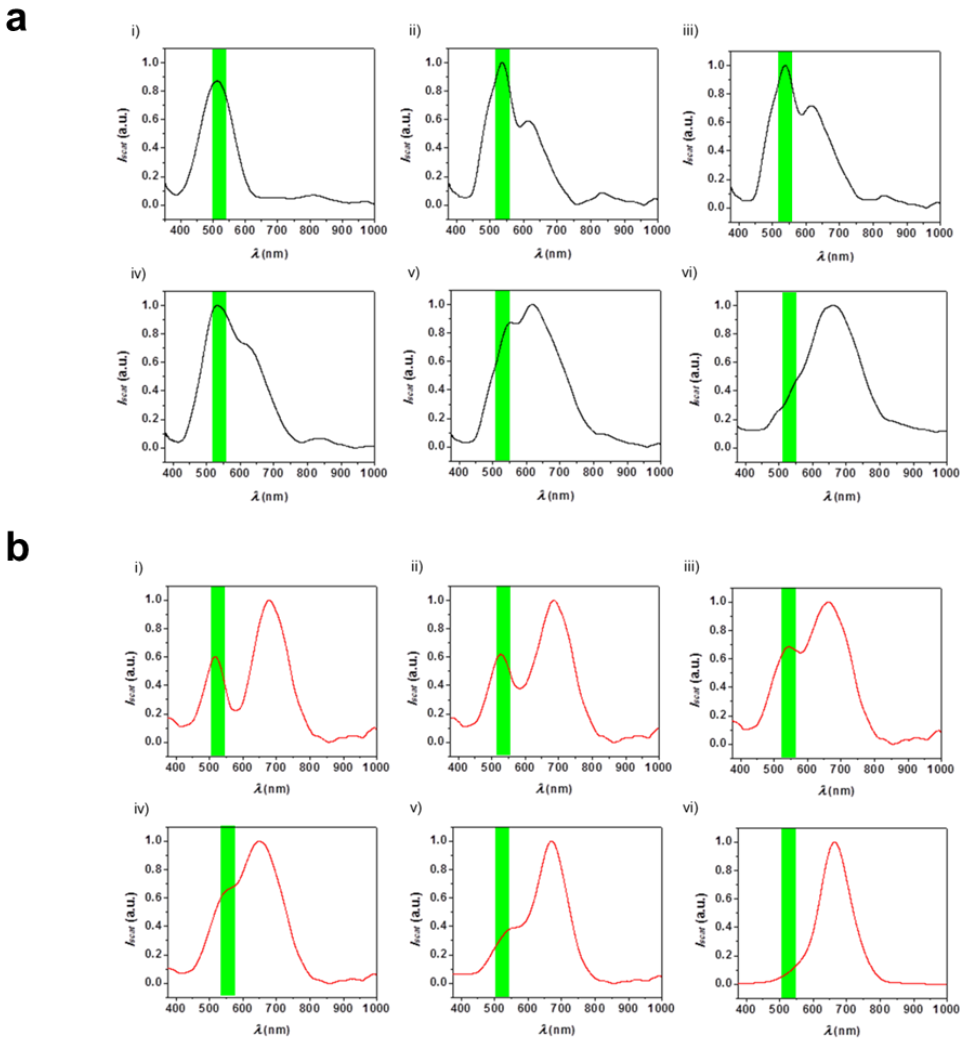

Figure 3.6 Optical properties of nanoplasmonic optical filter with varying particle density on SiO_2 substrate. (a) Optical properties of AuNPs with i) 5 particles/μm^3 , ii) 25 particles/μm^3, iii) 50 particles/μm^3, iv) 125 particles/μm^3, v) 250 particles/μm^3, and vi) 1000 particles/μm^3 and (b) Optical properties of AuNRs with i) 5 particles/μm^3 , ii) 25 particles/μm^3, iii) 50 particles/μm^3, iv) 125 particles/μm^3, v) 250 particles/μm^3, and vi) 1000 particles/μm^3.

intensity under the resonance condition. Here, we prepared testing structures with 6 different densities of AuNPs and AuNRs: ~ 5, ~ 25, ~ 50, ~ 125, ~ 250, and ~ 1000 particles/μm^3. These specimens showed a narrow size distribution regardless of their density on the substrate. This narrow size distribution minimized LSPR spectrum broadening for all the structures for both AuNPs and AuNRs. The extinction spectrum peak locations were consistent across the specimens regardless of the nanoparticle density except for ~ 1000 particles/μm^3. We find a density higher than ~ 1000 particles/μm^3 causes interparticle plasmonic coupling induced by an increase in the refractive index (Figure 3.1 and Figure 3.6), which results in a broader spectrum of the extinction peak. To quantify the plasmonic filtering effect, we defined the nanoplasmonic filtering enhancement as $(I_{ds\_no\ LSPR} - I_{ds\_LSPR}) / I_{ds\_no\ LSPR}$, where I_{ds_LSPR} and $I_{ds\_no\ LSPR}$ are the photocurrent with and without plasmonic nanoparticles on the SiO_2 thin layer, respectively. The nanoplasmonic filtering enhancement with the nanoparticle density shown in Figure 3.7 (b) is further evidence supporting the mechanism of our nanoplasmonic filter. The nanoplasmonic filtering variation from AuNPs dramatically increased from ~ 0.50 to 0.75 with particle density changes from 5 to 250 particles /μm^3, while the change of photocurrent from AuNRs was from 0.47 to 0.48 with a similar range of particle density change in AuNPs.

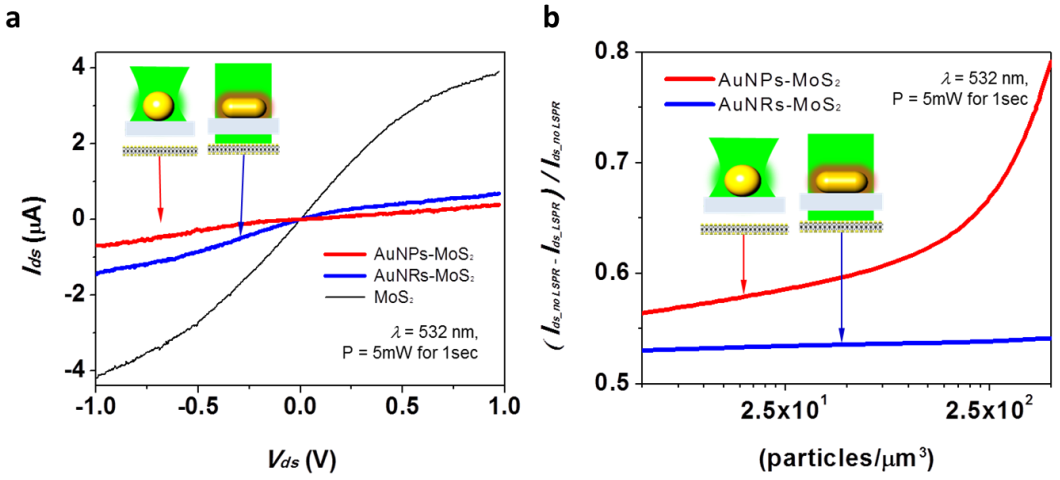

Figure 3.7 (a) Comparison of photocurrent between the AuNP and the AuNR, (b) nanoplasmonic filtering enhancement ($(I_{ds\_no\ LSPR} - I_{ds\_LSPR})/I_{ds\_no\ LSPR}$) as a function of the density of plasmonic particles in the atomically layered MoS_2.

3.3.3 Detection of Interleukin-1 beta (IL-1β) Biomarker Using Bio-Tunable Nanoplasmonic Biosensors

Next, we turned to performing rapid detection of cytokine with our devices. Our study employed interleukin-1 beta (IL-1β), a pro-inflammatory cytokine, in an aqueous phase as our model analyte. We chose IL-1β as the target because of (i) its clinical significance in immune monitoring processes [132], (ii) the well-established binding chemistry between IL-1β and its antibody on gold nanoparticles [44, 114-115, 133-135], and (iii) its surface binding that causes a near-field refractive index change without causing optical interference [136-138]. The biosensor preparation involved: (i) immobilization of gold nanoparticles onto a SiO_2 thin layer (AuNPs/SiO_2), (ii) self-assembly of 1-ethyl-3-[3-dimethylaminopropyl] carbodiimide (EDC) and/ N-hydroxysuccinimide (NHS) on the particle surfaces, (iii) antibody conjugation on the functionalized particles (Ab-AuNP/SiO_2), and (iv) attachment of the Ab-AuNP/SiO_2 thin layer on a few-layer MoS_2 flake with an alignment mark. The Ab-AuNP conjugate (50 nm in diameter) scatters light at λ = 532 nm with a sufficient intensity. The measured photocurrent (I_{ds}) increases over time with cytokine-antibody binding progresses on a nanoparticle surface. Here, a local refractive index change accompanying the cytokine binding causes a red shift of the extinction peak of the particle, leading to higher light transmission through the nanoplasmonic filter (Figure 3.8 (a)). After loading IL-1β ($C_{IL\text{-}1\beta}$ = 10 pg/mL) in a Phosphate-buffered saline (PBS) solution followed by a 30-min incubation process, the photo response of the device to a light illumination was measured as a function of time (Figure 3.8 (b)). At t = 0 min, the photocurrent I_{ds} was ~ 0.11 μA at V_{ds} = 1.0 V. The I_{ds} at V_{ds} = 1.0 V increased two times to ~ 0.23 μA in 10 min during the incubation process and reached a plateau later with the IL-1β-anti-IL-1β binding equilibrium established on the AuNPs of the nanoplasmonic filter. The plot of I_{ds} over time (I_{ds}-time curve) represents the IL-1β binding kinetics and allows us to estimate the binding affinity of IL-1β. The attachment and detachment rates of IL-1β were obtained from curve fitting to the plot based on a standard 1:1 binding kinetics model as k_{off} = 4.2×10^{-5} $M^{-1}sec^{-1}$ and k_{on} = 2.9×10^{5} M^{-1} sec^{-1}, respectively. The equilibrium constant (K_{eq}) was estimated to be 6.9×10^{9} M^{-1}, which well matches a typical equilibrium constant

value for an antigen-antibody interaction. With 5 repeats of the measurement, we observed good repeatability of the biosensing performance of the device. In addition, we would expect shorter detection time to determine the concentration of IL-1β using our subthreshold regimes analysis in the few-layer MoS_2 thin-film transistors [124]. The I_{ds} variation ($\Delta I_{ds}/I_o$) -time curves with a light illumination reached a steady state in ~ 10 min (Figure 3.8 (c)). Both at V_{ds} = 1.0 and -1.0 V, the time for the steady state is similar. Regardless of V_{ds} = 1.0 and -1.0 V, the $\Delta I_{ds}/I_o$ shows consistent value (= 0.8) at the steady state.

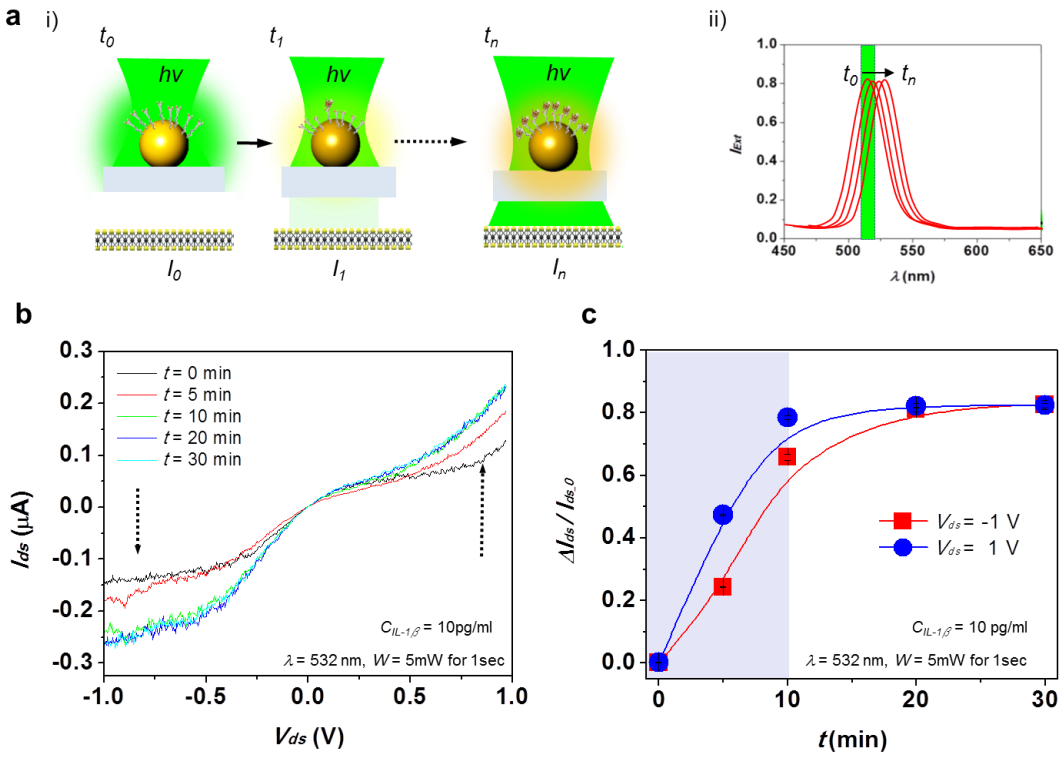

Figure 3.8 Rapid detection performance of bio-tunable nanoplasmonic filter on few-layer MoS_2 photodetector. (a) IL-1β surface binding effect on photo transmission of nanoplasmonic filter over time; i) The increasing number of IL-1β bound to the antibody-coated AuNP in causes shifts of the AuNP LSPR extinction peak, thus increases the photo transmission incident light through the nanoplasmonic filter. ii) The AuNP extinction spectrum experiences red-shifts over time during IL-1β surface binding incubation. An increase of IL-1β surface binding-induced photo transmission leads to a high level of photocurrent in the few-layer MoS_2 photodetector (green line: incident light spectrum; and red curve: nanoplasmonic filter extinction spectrum), (b) I_{ds} vs. V_{ds} curves of the few-layer MoS_2 photodetector at different IL-1β surface binding incubation time points for

a fixed IL-1β concentration of $C_{IL\text{-}1\beta}$ = 10 pg/ml. Each curve is obtained under illumination of light at λ = 532 nm, P = 5mW for1sec, and (c) photocurrent variation ($\Delta I_{ds\_t} / I_{ds\_0}$) over time during incubation process at V_{ds} = 1.0 and -1.0 V for $C_{IL\text{-}1\beta}$ = 10 pg/ml.

3.3.4 Quantification of Interleukin-1 beta (IL-1β) with Various Concentrations and Selectivity of the Biosensor

We further performed the cytokine measurement with different concentrations of IL-1β from 0.1pg/mL to 1ng/mL (Figure 3.9). Varying the concentration of IL-1β is expected to change the overlapping spectral band between the extinction peak of the nanoparticle and the wavelength of the light source. Increasing the IL-1β concentration results in higher optical transmission, leading to an increase in the photocurrent of the device (Figure 3.9 (a)). Measuring the photocurrent changes allowed us to quantify the IL-1β concentration of a sample. Our biosensor device incorporating the high-sensitivity few-layer MoS_2 photoconductive thin layer enabled recognition of a very low light intensity change at the presence of low-concentration IL-1β. We first measured the LSPR extinction spectral peak shift of the Anti-AuNP/SiO_2 thin layer from $C_{IL\text{-}1\beta}$ = 0.1 pg/mL to $C_{IL\text{-}1\beta}$ = 1 ng/mL using a photo spectrometer (USB4000, Ocean Optics) [44, 115]. The measured peak shift was ~ 0 or 0.2 nm (Figure 3.9 (b)), which was too small to detect with the above-mentioned LSPR extinction spectrum detection setup. Whereas, our device allowed quantification of IL-1β at a low concentration by managing to detect the subtle LSPR peak shift. At V_{ds} = 1V, I_{ds} increases from ~ 0.15 μA to 0.45 μA with $C_{IL\text{-}1\beta}$ increasing from 0.1 pg/mL to 1 ng/mL. The I_{ds}–time curves across the measured range of $C_{IL\text{-}1\beta}$ reached a steady state in ~ 10 min as we observed in Figure 3.8 (c). Figure 3.9 (c) represents the standard curve of our device and clearly demonstrates that the device yields high cytokine detection sensitivity and a large (10^6) dynamic range. We compared sensitivity between our biosensor (LSPR/MoS_2) and the commercial photospectrometer detecting an extinction spectral shift (LSPR) at the same surface density of AuNP on SiO_2 as a function of IL-1β concentration. In the comparison, we determined the limit of

detection from the decoupled LSPR/MoS_2 ($LOD_{LSPR/MoS2)}$ from the obtained calibration curve (Figure 3.9 (d)), Our device achieved a $LOD_{LSPR/MoS2}$ of 0.25 pg/mL while the direct LSPR extinction peak shift detection obtained a LOD_{LSPR} of 22.5 pg/mL at the same density of AuNPs. Here, all the LOD values were given by $3\sigma/k_{slope}$, where σ and k_{slope} are the standard deviation of background signal measured from a blank control and regression slope of calibration curve, respectively. Our decoupled LSPR/MoS_2 device is ~ 90 times more sensitive than the common LSPR peak shift detection method. The $LOD_{LSPR/MoS2}$ was also compared to the LOD obtained from ELISA, which is the current gold standard immunoassay method (Table 3.1).

Table 3.1 Limit of detection (LOD) resulting from different cytokine detection methods. A LOD value was experimentally determined in the current study for three cytokine detection methods, given by $3\sigma/k_{slope}$., where σ is the standard derivation of background noise detected from a blank sample, and k_{slope}. is the regression slope extracted by sigmoidal curve-fitting from a standard curve.

	Blank S.D. (σ) (%)	**U_{system} (3σ) (%)**	**k_{slope} $(pg/mL)^{-1}$**	**$LOD=3\sigma/k_{slope}$ (pg/mL)**
LSPR/MoS_2	4.61×10^{-4}	1.38×10^{-3}	0.0035	0.25
LSPR	1.50×10^{-3}	4.50×10^{-3}	0.0002	22.5
ELISA	0.0135	0.0405	0.004	10.12

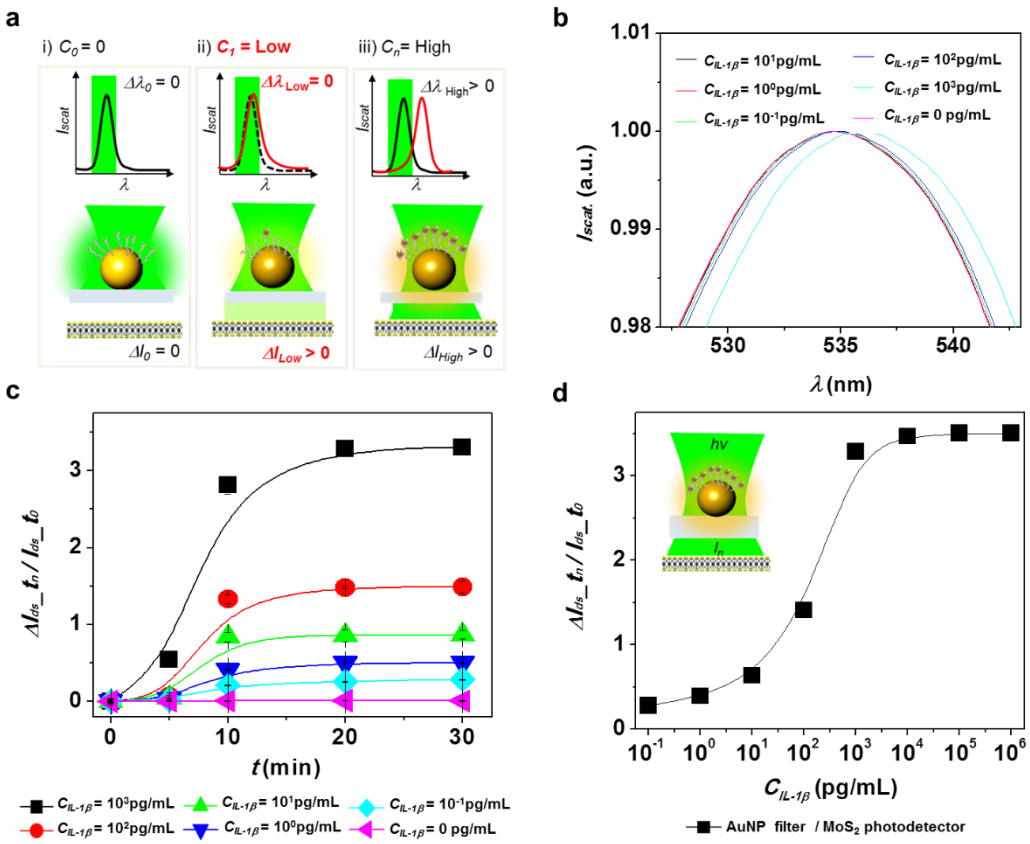

Figure 3.9 IL-1β Sensitivity of bio-tunable nanoplasmonic filter on few-layer MoS_2 photodetector. (a) Illustration of highly sensitive IL-1β detection using few-layer MoS_2; i) At a cytokine (IL-1β) free environment (C_0 = 0), no peak shift of the AuNP LSPR spectrum (represented by the scattering light spectrum I_{scat} here) or no photocurrent change is observed, ii) At a low concentration of IL-1β (C_1), a weak change of local refractive index at the AuNR surface leads to a I_{scat} peak shift hardly measurable by a photo spectrometer (ΔI_{Low}~0) while the photocurrent change (ΔI_{Low}>0) is detectable with the high-sensitivity few-layer MoS_2 photodetector, and iii) At a higher concentration of IL-1β (C_n), both the I_{scat} peak shift (ΔI_{High} > 0) and the photocurrent changes (ΔI_{High}> 0) are highly noticeable. (b) LSPR spectra of AuNP-coated SiO_2 surface at $C_{IL\text{-}1\beta}$ ranging from 0.1pg/mL to 1ng/ml, (c) Photocurrent variation (ΔI_{ds_t} / I_{ds_0}) during IL-1b surface binding incubation for different $C_{IL\text{-}1\beta}$ values. Each curve is obtained under photo illumination at λ = 532 nm, P = 5mW for 1sec, and (d) Standard curve of photoelectronic cytokine immunobiosensor incorporating bio-tunable nanoplasmonic filter on few-layer MoS_2 photodetector.

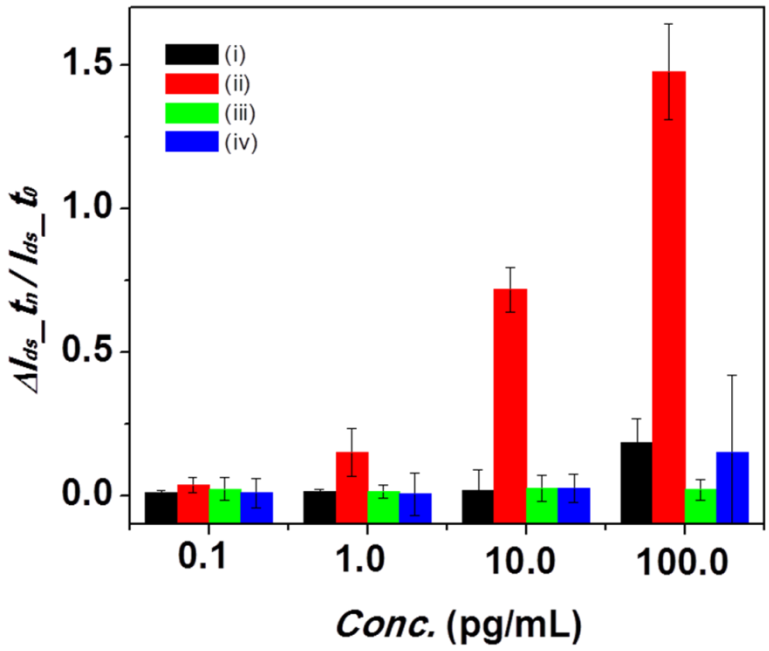

Figure 3.10 Highly selective detection of IL-1β owing to selective IL-1β and IL-1β antibody biding on nano plasmonic optical filter. Bar graph summarizing the variation of photocurrent to four cytokines (i) TNF-α, ii) IL-1β, iii) IL-6, and iv) INF-γ. The height of each bar, *ΔIds_tn/Ids_to*, represents photocurrent variation at 10 min after loading samples. Error bars correspond to standard errors (n = 3, P < 0.005).

In addition, the selectivity of the LSPR/MoS_2 biosensor was explored by testing the device response to four relevant cytokines, including tumor necrosis factor (TNF)-α, interferon type (INF)-γ, IL-6, and IL-1β at a concentration range from 0.1 to 100 pg/mL (Figure 3.10). We observed no variations of I_{ds} with analyte concentration for other cytokines than IL-1β. This verifies that the cross-reactivity is negligible with our device.

3.4 Summary

In conclusion, we have successfully developed a high-sensitivity, label-free cytokine immuno biosensing device integrating AuNP plasmonic biosensing assemblies on a SiO_2 thin layer and a MoS_2 photoconductive flake. The binding of biomolecules at

the surfaces of antibody-conjugated AuNPs changed the extinction spectrum peak of the SiO_2 thin layer due to a LSPR peak shift between the AuNPs and incident light. We showed that this effect enabled the AuNP-SiO_2 thin layer to act as a tunable optical filter responding to the presence of cytokines in a solution deposited on the device surface. The decoupled device architecture prevented electronic interactions between the photo-excited AuNP assemblies and semiconducting MoS_2 with a physical gap. This arrangement enabled highly stable detection of subtle variations of photocurrent in the MoS_2 layer accompanying changes in the light transmission of the AuNP-SiO_2 film during biomolecule quantification in an aqueous solution. As a result, we were able to detect IL-1β in PBS at a concentration as low as 250 fg/mL (14 fM) while obtaining its surface binding curve. The demonstrated dynamic range was as large as 10^6, which is about two orders of magnitude larger than that of ELISA. Real-time monitoring of the binding curve enabled us to complete the analysis within 10 min without waiting for the biosensing process to reach an equilibrium state, which is at least ~ 50 times faster than gold standard assays. The plasmo-photoelectronic biomolecule detection approach demonstrated in this study makes our device highly poised for standalone operation with its monolithically integrated architecture eliminating the need for an external signal reader, which would reveal a future direction for clinically relevant point-of-care applications. All of these device features represent immunoassay performances superior to those of conventional ELISA-based techniques.

Chapter 4

An Integrated Plasmo-Photoelectronic Biosensor Detects an Infection Biomarker Accompanying Cell Death in Neutrophils

4.1 Introduction

The human society has experienced a number of illnesses caused by bacterial infections throughout its entire history. As a potentially life-threatening form of infectious illness, sepsis causes more than 250,000 annual deaths in the United States alone [139]. Despite significant efforts made for sepsis diagnosis, existing methods still suffer major shortcomings, including a long sample-to-answer time, low sensitivity, and insufficient selectivity. For example, microbial culture to identify the source of infection, which is one of the gold standards of sepsis diagnosis, may take over 48 hours for incubation, and false negative results (over 24%) are very common due to a low density of blood bacteria at the early stage of infection [140]. Without timely diagnosis and treatment, the condition can quickly deteriorate and result in septic shock that causes multiple organ dysfunction syndrome (MODS) or mortality accompanied by severe systemic inflammation (Figure 4.1 (a)). A therapeutic strategy guided by a biomarker accurately reflecting the presence and severity of the disease is a promising approach for sepsis management [141-142].

Neutrophils are essential immune cells to combat microbial infections in the front line of defense [143]. One of the defense mechanisms of neutrophils involves cell death induced by the release of neutrophil extracellular traps (NETs), which form a meshwork of chromatin fibers mixed with granule-derived antimicrobial peptides and enzymes to kill bacteria extracellularly. Citrullination of histone H3 (CitH3), catalyzed by peptidylarginine deiminase (PAD), has recently been identified to be involved in an early step in the NETs-induced cell death (NETosis) in response to severe infection (Figure 4.1 (b)) [144]. Serum levels of CitH3 are significantly elevated with increasing severity of lipopolysaccharide (LPS)-induced septic shock [145]. Circulating CitH3 can be detected early and serve as a selective biomarker of septic shock, and administering a drug that diminishes or abolishes circulating CitH3 improves the survival of septic mice [146]. As such, CitH3 is a more promising biomarker to provide an early sign of septic shock and guide therapy than other biomarkers widely used to monitor severe infection and pro-inflammatory responses, such as procalcitonin (PCT), interleukin (IL-6), and IL-1β. However, timely CitH3-guided sepsis management is prohibited by the lack of a technology enabling quick, sensitive, and accurate detection of the CitH3 biomarker at the point of care (POC).

Researchers have extensively explored POC biomarker analysis techniques using localized surface plasmon resonance (LSPR) sensors incorporating antibody-conjugated metallic nanoparticles [147-148]. These LSPR biosensors are advantageous for POC measurements [149-151] as they are label-free, robust, rapid, cost-effective, and easy to integrate into miniaturized fluidic devices with simple optics [152-154]. They are also attractive for diagnosing and monitoring the trajectory of critically ill patients [154-155]. Our previous study [156] demonstrated that strategically integrating a LSPR biosensing layer above a molybdenum disulfide (MoS_2) photoconductive channel allows for constructing a self-contained photoelectronic protein biosensor. The small device architecture of this biosensor eliminates the need for large-volume off-chip detectors in signal transduction, such as charge-coupled devices (CCDs) and ultrahigh-resolution photospectrometers, thus potentially serving as a POC platform for CitH3-based early infection diagnosis. Unfortunately, this device still faces two major issues; (i) it cannot achieve sufficiently fast speed because of the significantly weak affinity of CitH3 to

antibodies on the commercial market; and (ii) it falls short of reaching the highest sensitivity in CitH3 detection due to the unoptimized structural arrangement of gold nanoparticles on its LSPR biosensing layer.

In this chapter, we report a highly miniature (2.5×2.5 μm^2) biosensor device combining nanoscale plasmonic and photoelectronic effects for detection of the CitH3 infection biomarker (Figure 4.1 (c) and (d)). In this study, we constructed structurally optimized hemispherical gold nanoparticle arrays, namely "gold nanohemispheres (AuNHs)", using a highly scalable self-assembly material synthesis technique. After functionalizing AuNHs with our lab-made high-affinity CitH3 monoclonal antibodies [146], we incorporated them into the aforementioned LSPR-MoS_2 device architecture [156]. The device was newly termed the "integrated nano optoelectronic biosensor (iNOBS)" and was shown to achieve optoelectronic detection of CitH3 and other sepsis-related biomarkers (IL-1β, and PCT) in serum at high sensitivity. The operation of iNOBS was supported by the broadly ranged photoresponsivity of a few-layer MoS_2 photoconductive channel. The AuNH surfaces of iNOBS achieved a large electric field enhancement for incident light at a biologically behind near-infrared (NIR) wavelength of $\lambda = 650$ nm. Taken together, the iNOBS-based label-free binding assay enabled CitH3 detection with a LOD of 0.87 pg/mL (56 fM), which is 250-fold smaller than that of commercial ELISA, a large dynamic range of 10^5, a short sample-to-answer time of 20 min, and a small sample volume of 2.5 μL. The accuracy of our iNOBS-based CitH3 measurement was confirmed by ELISA over a wide range from 10^{-2} to 10^1 ng/mL. With the remarkable label-free biosensor, we established the ability of continuously monitoring the time-varying CitH3 biomarker profiles in the circulation system of a sepsis mouse model.

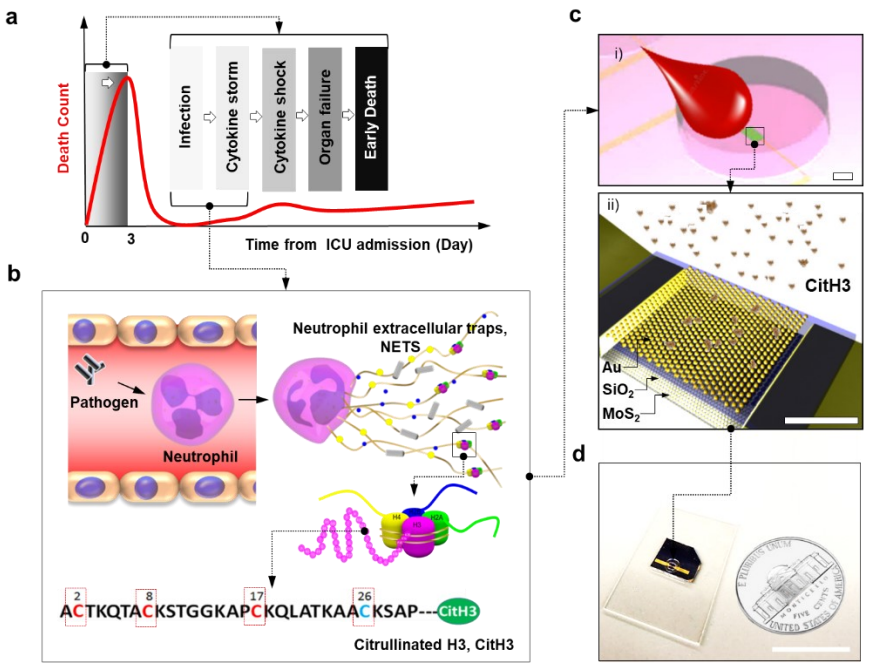

Figure 4.1 Neutrophil extracellular traps (NETs)-induced sepsis biomarker detected by integrated nano optoelectronic biosensor (iNOBS). (a) Death count of patients in septic shock after intensive care unit (ICU) admission. (b) CitH3 released into blood circulation upon neutrophil extracellular trap (NET)-induced immune cell death (NETosis) occurring in response to severe infection. CitH3 serves as a specific sepsis biomarker at an early stage of sepsis development. The 4 unique citrullinated molecular sites (4 Cits) of CitH3 are used for high-affinity binding with the custom-made antibody in this study. (c) Schematic of the iNOBS device architecture and operation; i) loading of a sample (e.g., serum) of small volume (~2.5 mL) onto a polydimethylsiloxane (PDMS) microfluidic well (scale bar = 200 μm), ii) settling of biomarker molecules onto the device surface (scale bar = 500 nm). (d) Photo image of the iNOBS chip (scale bar = 15 mm).

4.2 Experimental Setup for Plasmonic-Photoelectronic Biosensors (iNOBS)

4.2.1 Fabrication and Characterization of Plasmo-Photoelectronic Nanostructures

The iNOBS device architecture has three main components: (i) a bio-tunable nanoplasmonic optical filter (Bio-NOF) layer, which is a thin (100 μm) SiO_2 substrate covered by gold nanoparticles (AuNPs); (ii) a few-layer MoS_2 photoconductive channel underneath the Bio-NOF layer; and (iii) a polydimethylsiloxane (PDMS) layer with a

microfluidic well above the Bio-NOF layer. Only a small fraction of incident light transmits through the Bio-NOF layer initially and reaches the MoS_2 photoconductive channel, which yields a small baseline photocurrent signal (I_{ph_0}) (Figure 4.2 (a)). The resonant behavior of the conduction band electron oscillations near the surface of the optically excited nanoparticles (*i.e.,* LSPR effect) varies with a local refractive index (n_m) change brought by the surface binding of protein molecules.

As illustrated in Figure 4.2 (b), constructing highly packed, uniform AuNPs on the Bio-NOF layer is necessary to achieve high sensitivity in CitH3 measurement. A uniform distribution of AuNPs results in a narrow LSPR spectrum curve. Our previous

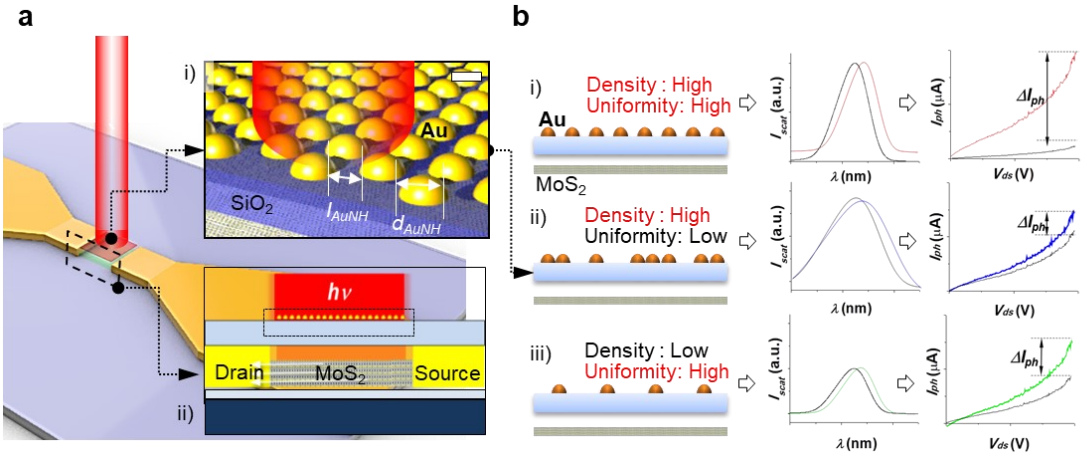

Figure 4.2 Bio-tunable nanoplasmonic optical filter (Bio-NOF). (a) i) Bio-NOF consisting of anti-antibody-conjugated gold nano-hemispheres (AuNHs) on a thin SiO_2 substrate (scale bar = 40 nm), ii) cross-sectional schematic of the iNOBS device architecture. (b) Conceptual illustration showing the impact of the density and uniformity of the gold nanoparticle arrangement on the LSPR spectrum of Bio-NOF and the I_{ph}-V_{ds} curve of iNOBS. i) high-density, high-uniformity arrangement expected to yield a sharp LSPR spectrum curve and a larger photocurrent increase ($\Delta I_{ph} = I_{ph} - I_{ph\_0}$) in response to a local refractive index change. ii) high-density, low-uniformity arrangement expected to yield a broad LSPR spectrum curve and a smaller value of ΔI_{ph} . iii) low-density, high-uniformity arrangement expected to yield weak LSPR-based photoabsorption and a smaller value of ΔI_{ph}.

study [156] detected IL-1β, a pro-inflammatory cytokine, using a similar device to iNOBS. The AuNPs on the Bio-NOF layer in this device were deposited by a simple, cost-effective method of casting a droplet of colloidally suspended nanoparticles (*i.e.,*

drop-casting method). The arrangement of the drop casting-deposited AuNPs showed poor uniformity. However, this was still acceptable in the previous study because strong antigen-antibody affinity is found for IL-1β. In contract, we expect that CitH3 measurement with weak antibody affinity inherently limits a local refractive index shift in the presence of the analyte at a given concentration. To address this issue, we structurally engineered self-assembled AuNH arrays with an optimal interparticle distance and density to maximize the sensitivity of our measurement in this study (Figure 4.3).

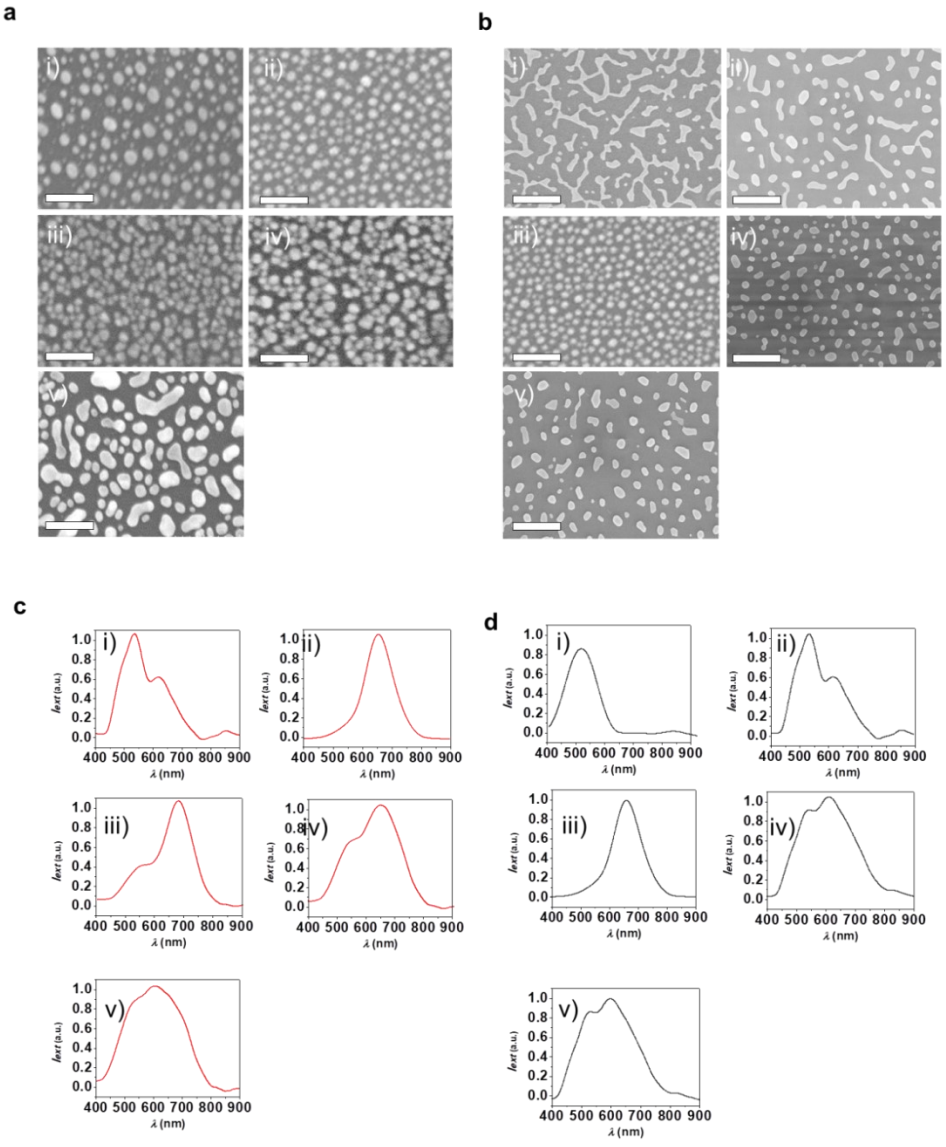

Figure 4.3 Fabrication and characterization of arrayed plasmonic gold nano hemispheres (AuNHs). The arrayed AuNHs were constructed in a controlled

manner by varying the gold layer deposition thickness and the thermal treatment duration. (a) AuNH morphologies (SEM images) resulting from a Au layer deposited with the thickness of 2, 5, 10, 20, and 40 nm, respectively, (scale bar = 250 nm) under the thermal treatment of 30 min at T = 500 °C. (b) AuNH morphologies (SEM images) resulting from the thermal treatment of 10, 30, 60, and 120 min, respectively, at T = 500 °C for a Au layer deposited with the thickness of 5 nm (scale bar = 250 nm). (c) LSPR extinction spectra of AuNHs fabricated with a Au layer deposited with the thickness of 2, 5, 10, 20, and 40 nm, respectively, (scale bar = 250 nm) under the thermal treatment of 30 min at T = 500 °C. and (d) LSPR extinction spectra of AuNHs with a Au layer deposited with the thickness of 5 nm under the thermal treatment of10, 30, 60, and 120 min, respectively, at T = 500 °C (scale bar = 250 nm).

Figure 4.4 (a) shows a scanning electron microscope (SEM) image of the constructed AuNHs with highly enhanced uniformity and density. The arrayed AuNH arrangement has a surface density of D_{AuNH} = ~ 800 particles/μm^2, a particle size of d_{AuNH} = 42 nm ± 10%, and an interparticle distance of l_{AuNH} = ~ 43 nm with a standard deviation less than 30% (Figure 4.4 (b)). Compared to the AuNP arrangement prepared by the

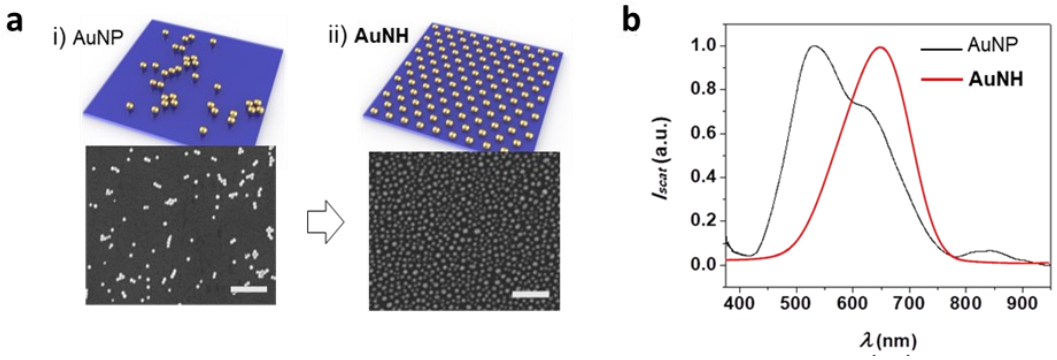

Figure 4.4 (a) Highly scalable self-assembly of optimally engineered gold nanostructural arrays; schematics and scanning electron microscopy (SEM) images of i) drop casting-deposited AuNPs, ii) self-assembled arrayed AuNHs (scale bar = 500nm), (b) Analyzed interparticle distance (I_{AuNH}) and size distribution (d_{AuNH}) of arrayed AuNHs.

drop-casting method, the arrayed AuNH arrangement showed a five times narrower distribution in both particle size and interparticle distance. Our finite element analysis

predicted a strong electric field confined between two neighboring AuNH particles (Figure 4.5). We measured LSPR spectra for both AuNP and AuNH structures with

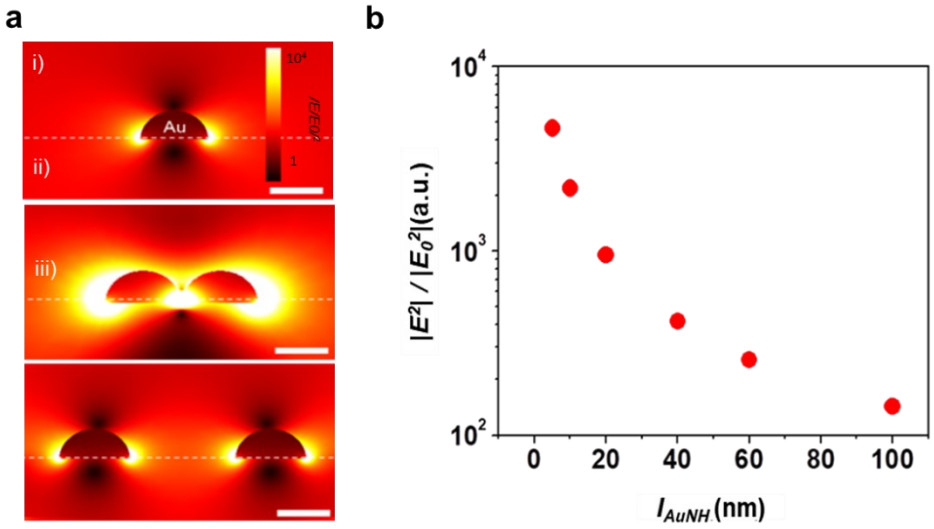

Figure 4.5 Finite element analysis (FEA) of AuNH LSPR substrate. (a) near-field electromagnetic field distributions around i) a single and two neighboring AuNHs with I_{inter} = ii) 10 nm and iii) 100 nm at λ = 650 nm (scale bar = 50nm), (b) E-field enhancement as a function of I_{AuNH}.

similar values of particle density (~ 800 particles/μm^2) (Figure 4.6 (a)). The spectrum of the arrayed AuNH arrangement yielded a narrower LSPR shape with a peak at λ = 650 nm. We measured the base photocurrent I_{ph_0} for two iNOBS devices, one with a Bio-NOF layer incorporating the drop casting-deposited AuNPs and the other with a Bio-NOF layer incorporating the arrayed AuNHs. Under laser light illumination at λ = 650nm, we observed I_{ph_0} = 0.77 μA and I_{ph_0} = 0.1 μA at an voltage applied across the MoS_2 channel (a drain-source voltage) of V_{ds} = 1V for the former (AuNP) and latter (AuNH) devices, respectively (Figure 4.6 (b)). The significantly smaller I_{ph_0} value for the AuNH device indicates that our self-assembly-based structural engineering approach served well for constructing a Bio-NOF layer with much higher nanoplasmonic optical filtration efficiency.

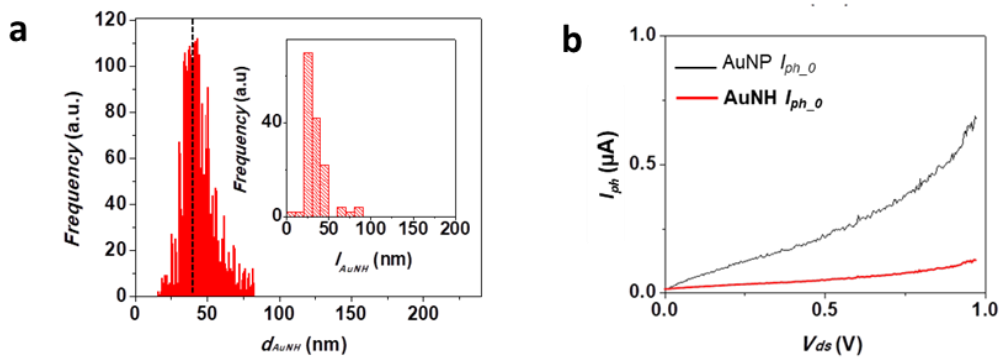

Figure 4.6 (a) LSPR spectra of drop casting-deposited AuNPs and the arrayedAuNHs. (b) I_{ph}-V_{ds} curves for the baseline photocurrent I_{ph_0} of iNOBS with drop casting-deposited AuNPs and arrayed AuNHs of similar particle density (~ 800 particles/μm^2).

4.2.2 Fabrication and Characterization of a Few-Layer MoS_2 Photodetector

We fabricated the photoconductive few-layer MoS_2 channel on a thermally oxidized silicon substrate using our micro-printing method (Figure 4.7 (a)) [56]. A pair of Ti/Au pads laterally sandwiching the MoS_2 channel served as the electrode contacts for reading sensor signals (drain current, I_{ds}) at V_{ds}. The effective channel length was measured to be ~1 μm, which ensured a highly uniform crystal structure for the MoS_2 sensing region. The as-printed MoS_2 channel had a uniform thickness of 14.5 nm with ± 5% tolerance along the path that was determined by atomic force microscopy (AFM) (Figure 4.7 (b)). This allowed us to operate the iNOBS device with the sufficiently high photoresponsivity of the few-layer MoS_2 channel. The laser illumination a λ = 650 nm resulted in 100 times photo-enhancement (Figure 4.8).

We characterized the LSPR shift of the "bare" arrayed AuNHs prior to antibody conjugation in response to the changing n_m of a surrounding medium (glycol-water solution). Additionally, we measured the photoresponsivity (R = I_{ph}/P_{in}, where P_{in} is power density of incident light) spectrum of the MoS_2 channel (Figure 4.9 (a) and Table 4.1). The value of n_m was varied with the glycol-to-water ratio in the medium. We observed a reasonably good overlap between the spectra of the photoresponsivity of the MoS_2 channel and of the LSPR of the arrayed AuNHs, and the illumination optical band

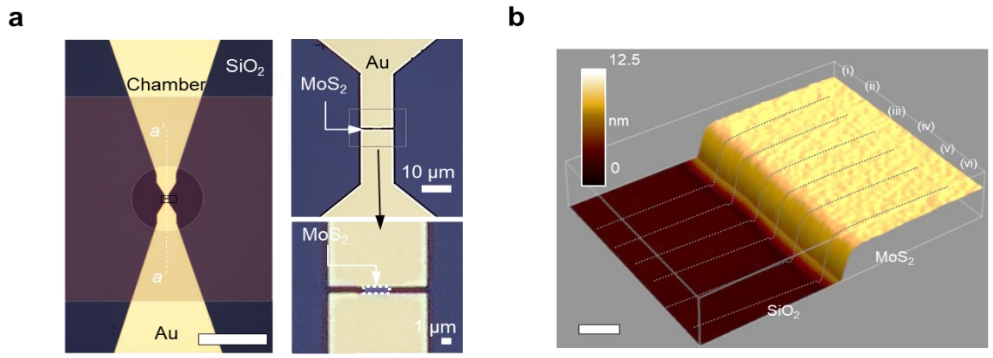

Figure 4.7 Integrated plasmonic nanostructure array and MoS_2 channel. (a) Optical micrographs of a 14 nm thick, 1 μm long MoS_2 channel with electrodes (scale bar = 10μm), (b) Atomic force microscope image of the MoS_2 layer on a SiO_2 layer (100 nm thickness).

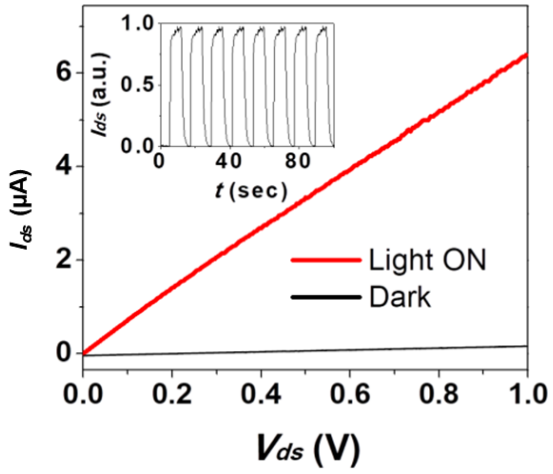

Figure 4.8 I_{ds}-V_{ds} characteristics of the MoS_2 under the dark condition and the light illumination (λ = 650 nm and P= ~ 2.4 mW) (Inset: I_{ds} under alternating Light-ON and OFF states).

(λ = 650 nm ± 10 %). Using an iNOBS device with the bare AuNHs, we measured the variation of I_{ph} with n_m and compared it with the LSPR peak shift ($\Delta\lambda_{max}$) characterized above (Figure 4.9 (b)). The measured I_{ph} linearly correlates to $\Delta\lambda_{max}$ (R^2 = 0.9986), which indeed confirmed that LSPR-shift was responsible for the iNOBS photocurrent signal change.

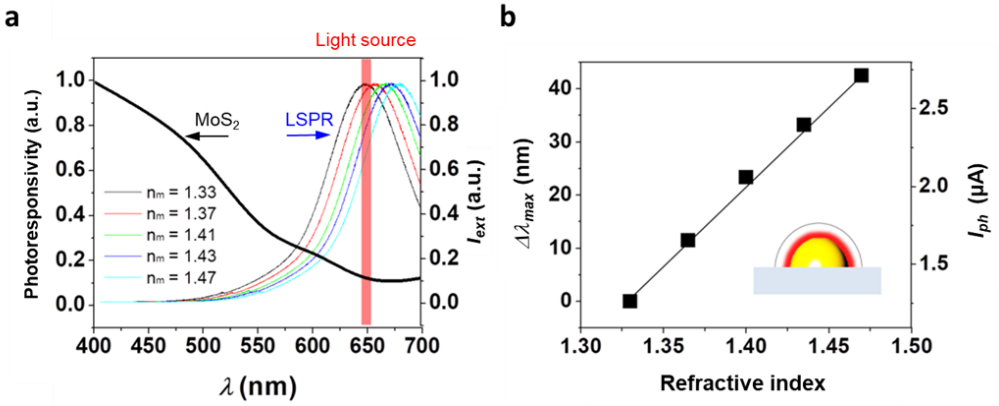

Figure 4.9 (a) LSPR spectra of the Bio-NOF with the arrayed AuNHs (arbitrary unit) for the different values of the environmental (bulk) refractive index (n_m) varying from 1.33 to 1.47 and photoresponsivity spectrum of the MoS_2 photoconductive channel, both compared to the spectral band of the incident light (λ = ~ 650 nm). (b) LSPR peak wavelength shift ($\Delta\lambda$) of the arrayed AuNHs vs. I_{ph} of the MoS_2 photoconductive channel at V_{ds} = 1.0 V as a function of n_m.

Table 4.1 Photoresponsivity Values of MoS_2 Photoedtectors.

Sample	Measurement Conditions	Photoresponsivity
Ref. 1 [157]	V_g = -70 V, V_{ds} = 8 V λ = 561 nm, P = 150 pW	~ 880 A W^{-1}
Ref. 2 [68]	V_g = 37 V, V_{ds} = 2 V White illumination, P = 0.7 mW	~ 11.4 mA W^{-1}
Ref. 3 [158]	V_g = -40 V, V_{ds} = 1 V λ = 520 nm, P = 40 mW	~ 0.25 A W^{-1}
Ref. 4 [159]	V_g = -3 V, V_{ds} = 1 V λ = 633 nm, P = 50 mW	~ 12 mA W^{-1}
Ref. 5 [160]	V_g = 0 and 50 V, V_{ds} = 1 V λ = 550 nm, P = 80 μW	~ 50 μA W^{-1} (at V_g = 0) ~ 7.5 mA W^{-1} (at V_g = 50)
Our MoS_2	V_g = 0 V, V_{ds} = 1 V λ = 650 nm, P = 24 nW	~ 267 A W^{-1}

4.3 Experimental Results

4.3.1 High-performance infection biomarker detection

Our study functionalized the AuNHs of our device with a new CitH3 monoclonal antibody (Figure 4.10). Commercially available CitH3 monoclonal antibodies bind to histone H3 only at N-terminal with 3 citrullinated sites (3 Cits) catalyzed by PAD4 alone. This results in limited antibody affinity. In contrast, our antibody was designed in our lab and synthesized in a custom-made manner so that it can tightly interact with 4 unique molecular sites (4 Cits) citrullinated by PAD4 and PAD2 (Figure 4.1 (b)). Thus, the novel CitH3 antibody has a higher affinity, in addition to specificity, compared to conventional antibodies. Additionally, our recent study shows that our anti-CitH3 antibody can significantly improve survival in a mouse model of sepsis [161].

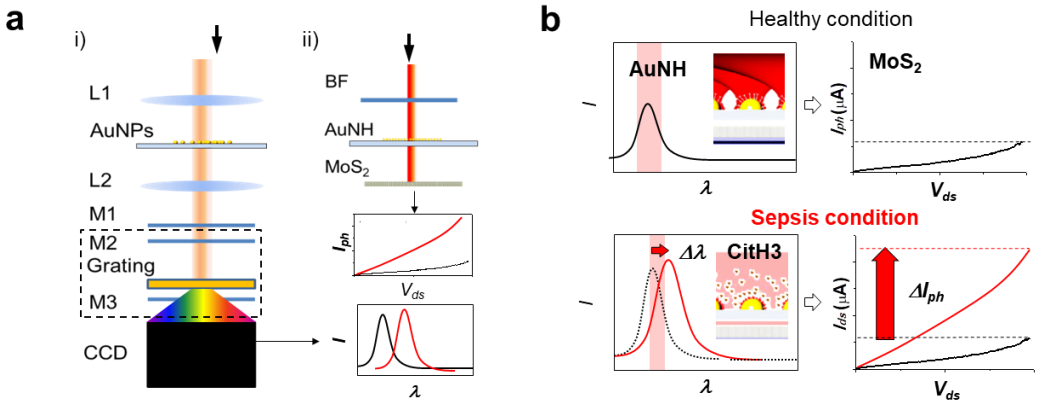

Figure 4.10 Nano-plasmo-photoelectronic detection performance of iNOBS. (a) Setups of i) LSPR spectroscopy measurement (L1: darkfield condenser, L2: objective lens, M1-3: mirror 1-3, CCD: charge-coupled detector, dashed line box: spectrometer) and ii) iNOBS measurement based on LSPR-MoS_2 nano-plasmo-photoelectronic signal transduction (BF: band path filter). (b) Binding of CitH3 antigen molecules onto the antibody-conjugated AuNHs continues to decrease the LSPR-induced absorption of incident light at the Bio-NOF layer until the system reaches equilibrium. This is translated to a photocurrent increase ΔI_{ph} in the MoS_2 channel over time.

The iNOBS device enabled simpler and more miniaturized biomarker detection as compared to a conventional LSPR biosensing setup (Figure 4.10 (a)). Before conducting the iNOBS assay illustrated in Figure 4.10 (b), we first verified the performance of the Bio-NOF layer for CitH3 quantification using a commercial photo spectrometer. In this test, we loaded a CitH3-spiked serum sample onto the Bio-NOF layer with C_{CitH3} varying from 10^{-4} to 10^{1} ng/mL (Figure 4.11). We observed a total peak wavelength shift of $\Delta\lambda_{max}$ ~10 nm when C_{CitH3} decreased from 10^{1} to 10^{-2} ng/mL. This setup detected no noticeable peak wavelength shift for C_{CitH3} <10^{-2} ng/mL. With our observation here, we confirmed that the optical transmission of the Bio-NOF layer was tuned with the LSPR spectral shift accompanying the variation of C_{CitH3}.

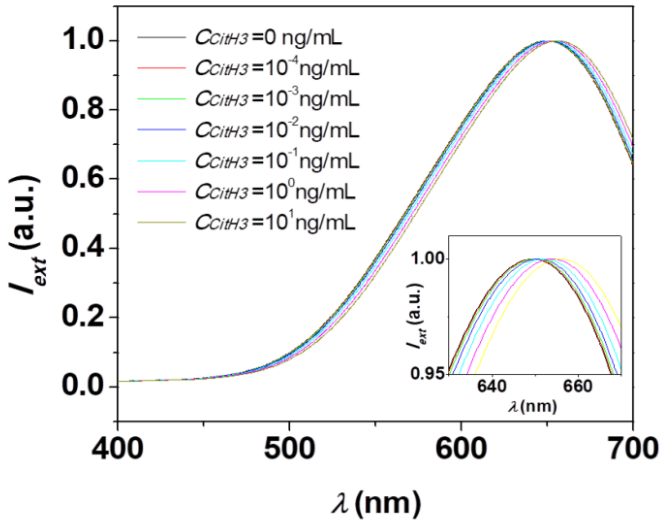

Figure 4.11 LSPR spectral peak shift of the antibody-conjugated Bio-NOF layer with varying C_{CitH3}.

Figure 4.12 (a) plots transient curves of the iNOBS photocurrent signal ΔI_{ph} (t) = I_{ph} (t) - I_{ph0} as functions of the incubation time t measured at V_{ds} = 1.0 V for C_{CitH3} between 10^{-4} and 10^{1} ng/mL (the curve at C_{CitH3} = 0 is the baseline). With C_{CitH3} reaching the lower (10^{-4} ng/mL) and upper (10^{1} ng/mL) bounds, the ΔI_{ph} value saturated at ~1.2 μA and ~1.7 μA, respectively, within 20 minutes after loading a serum sample. The C_{CitH3} value in a given sample can be quantified from the normalized photocurrent

variation $\Delta I_{ph}/I_{ph0}$. Figure 4.12 (b) shows the standard calibration curve of the iNOBS device with C_{CitH3} varying from 10^{-4} to 10^{1} ng/mL. The curve has a sigmoidal shape that is typically observed when antibody-antigen binding reactions are quantified at the full dynamic range [162]. The weak signal at the low concentration range becomes buried in the background noise. The binding sites on the sensor surface becomes saturated with the analyte molecules at the high concentration range. Thus, these two extreme ranges result in the lower and upper saturations of the standard curve. From this curve, we found that the device achieved a LOD of 0.87 pg/mL with a large (10^5) dynamic range. The curve also exhibits a trend similar to that obtained from the LSPR peak position (λ_{LSPR}) measured by the LSPR biosensing setup using the commercial photo spectrometer in Figure 4.11. While this LSPR biosensing setup failed to distinguish the peak shift for C_{CitH3} <10^{-2} ng/mL owing to its limited spectral resolution (~ 0.1 nm), the iNOBS device was still able to capture a noticeable change of I_{ph} resulting from the small LSPR peak shift even at C_{CitH3} <10^{-2} ng/mL.

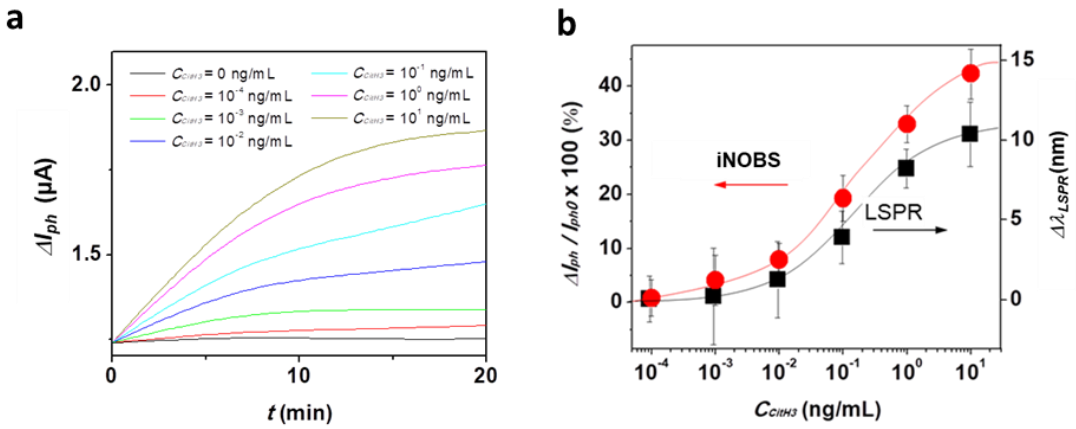

Figure 4.12 (a) ΔI_{ph} at V_{ds} = 1.0 V as a function of the incubation time after sample loading with C_{CitH3} ranging from 10^{-4} to 10^{1} ng/mL. (b) Standard calibration curves (photocurrent change ($\Delta I_{ph}/I_{ph\_0}$) vs. C_{CitH3}) obtained using the iNOBS (LSPR-MoS_2) device and the LSPR spectroscopy setup.

4.3.2 Validation of the iNOBS Assay Using Clinical Samples

Using the iNOBS device, we performed sepsis biomarker analysis for serum samples extracted from living mice (Figure 4.13). A regression line for correlating the results from iNOBS and commercial ELISA assays measuring CitH3 was obtained for the sample samples (Figure 4.13 (a)). The correlation shows a strong linear relationship (R^2 = 0.9968). The iNOBS assay achieved a LOD_{iNOBS} as small as 0.87 pg/mL whereas the ELISA exhibited an LOD_{ELISA} of 232 pg/mL (Table 4.2). Here, the ELISA test employed a commercial CitH3 monoclonal antibody (Cayman Chemical, Ann Arbor, MI, USA). Such a comparison shows that the iNOBS device has a superior concentration sensitivity (or LOD) for CitH3 over 250 times higher than that of the ELISA assay.

Table 4.2 Limit of detection (LOD) resulting from different CitH3 detection methods. We experimentally determined LOD values for the three methods used in the current study to detect CitH3 in serum. Here, the LOD value is given by $3\sigma/k_{slope}$, where σ is the standard derivation of the background noise detected with a blank sample, and k_{slope} is the regression slope extracted by sigmoidal curve-fitting to the standard curve.

	Sample Volume (μL)	Blank S.D. (σ) (%)	Usystem (3σ) (%)	k slope (pg/mL)-1	LOD=3σ/kslope (pg/mL)
iNOBS	2.5	0.00093	0.00280	0.0032	0.87
LSPR	25	0.00236	0.00709	0.0004	17.28
ELISA	150	0.0155	0.0405	0.00175	232

Subsequently, we performed a control experiment to test the iNOBS's selectivity to the target biomarker, *i.e.* CitH3, in comparison with other four different background biomarkers relevant to sepsis (*i.e.*, PCT, IL- 1β, IL-6, and TNF-α) in mouse serum with their concentrations ranging from 10^{-4} to 10^{1} ng/mL all together (Figure 4.13 (b)). In this test, we observed no noticeable changes in $\Delta I_{ph}/I_{ph0}$ with respect to the concentrations of any biomarkers other than CitH3. This result indicates negligible cross-reactivity among

these biomarkers and therefore proves the capability of the iNOBS assay. Our device enabled highly selective detection of target biomarker molecules.

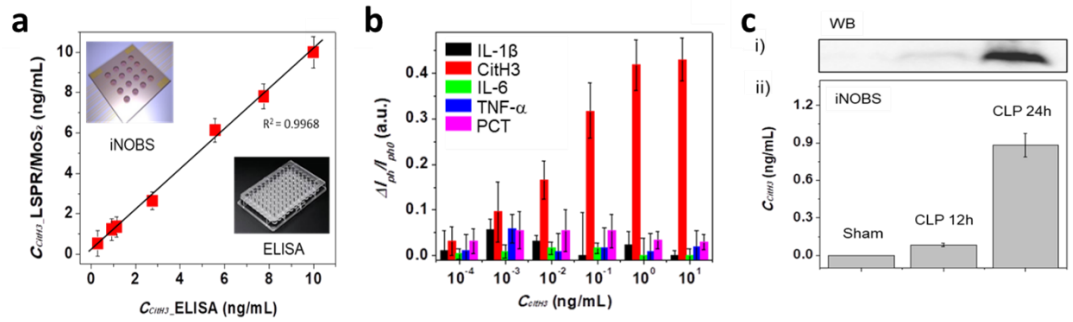

Figure 4.13 iNOBS-based sensitive and selective sepsis biomarker detection using mouse models. (a) Linear regression between iNOBS assay and ELISA data for the same serum samples spiked with CitH3 at $C_{CitH3.}$ ranging from 10^{-2} to 10 ng/mL. The iNOBS assay was performed ~ 20-times faster and 250-times more sensitive than ELISA. (b) Photocurrent signal ($\Delta I_{ph}/I_{ph0}$) data of the iNOBS obtained for a mixture of IL-1β, CitH3, IL-6, TNF-α, and PCT in healthy (sham) mouse serum at various concentrations (n = 6). The concentrations for the background biomarkers: IL-1b; IL-6; TNF-a; and PCT were varied so that their values were identical with that of CitH3 for each measurement. The data show high selectivity of the device to CitH3 as the signal for CitH3 is distinctly higher than those for the other biomarkers with a statistical significance ($p \leq 0.01$). (c) CLP mouse model study. CLP treated mouse as a "gold standard clinical sepsis model" which mimics human sepsis development. Comparison of circulating CitH3 detected by i) western blot and ii) the iNOBS assay at 0, 12 and 24 h after CLP treatment.

Furthermore, we applied the iNOBS device in the measurement of circulating CitH3 in a living mouse treated by cecal ligation and puncture (CLP)-induced sepsis [163-164]. The CLP procedure mimics a ruptured appendix or perforated diverticulitis in human and allows for identifying an irreversible stage of sepsis where the excision of necrotic tissue cannot improve survival [165-166]. Therefore, CLP has been recognized as a standard animal model for sepsis study (Figure 4.13 (c)) [167]. Based on previous studies reporting that mortality was dramatically changed within 24 h [146, 168]. we measured CitH3 for serum samples collected from the mouse at 0, 12, and 24 h after the CLP procedure. For comparison, a western blot was also performed for the same mouse serum samples. The serum collected at 0 h did not show any signature of CitH3 in both the iNOBS assay and the western blot measurement. The CitH3 level in serum reached ~

0.11 ng/mL at 12 h after the CLP insult, and further increased to ~ 0.89 ng/mL at 24 h. The western blot images qualitatively matched the iNOBS assay data. Importantly, our iNOBS assay provided consistent quantitative data with a 100-fold faster measurement speed in comparison with the conventional western blot technique.

4.3.3 Multi-Time Point Measurement of Infection Biomarker Profile for Living Mice

Finally, we demonstrated iNOBS-based multi-time-point detection of biomarkers using different mouse models. We first obtained time-series profiles of CitH3 and two other biomarkers (IL-1β and PCT) for a LPS-injected living mouse over 12 h, at which the animal died (Figure 4.14 (a)). The measurements were repeated with multiple devices (n =5). After the injection of LPS at ~1.2 ng/mL, we observed that C_{CitH3} in the endotoxic mouse monotonically increased over time, rapidly reached a high level over 1 ng/mL at 6 h, and steadily increased to 1.385 ng/mL at 12 h. The PCT concentration (C_{PCT}) was as low as 0.075 ng/ml at 6 h and only increased to 0.078 ng/mL at 12 h (20 times smaller than the C_{CitH3} value*)*. The IL-1β concentration ($C_{IL\text{-}1\beta}$) in the sample was ~1.031 ng/ml at 3 h but finally decreased to ~0.758 ng/mL at 12 h after repeating fluctuations. However, the C_{CitH3} profile followed the endotoxic shock of the host consistently increasing from the initial point of LPS injection up to the endpoint of the animal life. As another approach of demonstration, we also successfully monitored the endotoxemia of another mouse model treated by YW3-56, an anticancer PAD inhibitor, *via* intraperitoneal injection (Figure 4.14 (b)). As expected, our data showed that the treatment with YW3-56 significantly decreased C_{CitH3} and $C_{IL\text{-}1\beta}$ as compared to those insulted only with LPS. Finally, we could monitor the dynamic response of the level of the biomarkers in such a shorter time interval which cannot be achieved by the current gold standard ELISA method.

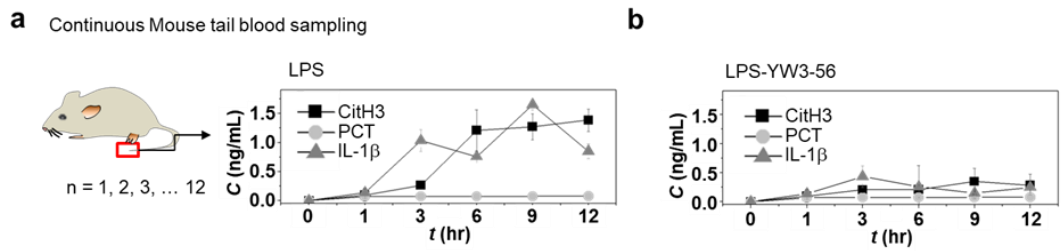

Figure 4.14 Multi-time-point CitH3 measurement for a living mouse with the iNOBS device. (a) Time-course profiles of circulating CitH3, PCT, and IL-1β in a living mouse at 0, 1, 3, 6, 9, and 12 hr. after LPS injection. At each measurement time point, a serum sample with a volume of 7.5 μL was collected from the mouse tail. The values of the biomarker concentrations were extracted from the obtained calibration curve (Figure B.1 and Table B.1 in Appendix B). (b) Time-course profiles of circulating CitH3, PCT, and IL-1β for a living LPS-injected mouse under treatment with YW3-56, an anticancer PAD inhibitor.

Furthermore, we employed two different mouse models for the iNOBS assay: LPS-induced shock (LPSS) as an infectious model and hemorrhagic shock (HS) (30% blood loss) as a non-infectious model, and replicated our recent finding that CitH3 is detected in LPSS but not in HS (Figure 4.15 (a) and (b)) [146]. We measured the level of the target biomarkers in blood samples at 0, 0.5, and 12 h after LPS or HS insult. LPS led to an increase of C_{CitH3} in the LPS-insulted mice from 0.022 to 1.137 ng/ml at 0.5 and 12 h, respectively; while in the HS mice, very low levels of C_{CitH3} (from 0.001 to 0.031 ng/ml) were detected. The C_{CitH3} levels at 0.5 and 12 h clearly distinguished the non-infectious and infectious systemic inflammation development with a high sensitivity. The $C_{IL\text{-}1\beta}$ value also increased distinctively from 0.5 to 12 h after LPS insult. However, we observed in Figure 4.14 (a) that the IL-1β levels showed fluctuation over time. Therefore, IL-1β alone could hardly reflect the course of endotoxic shock. The concentration of PCT was too low to be sensitive for differentiating between LPS-induced endotoxic shock and hemorrhagic shock.

LPS is a central mediator that plays a critical role in the acute pathogenesis of endotoxemia and endotoxic shock [169]. LPS can stimulate nuclear translocation of PAD and induce neutrophil extracellular trap (NET) formation. CitH3, as a component of the NETs, is released into circulation meanwhile. The temporal profile of the CitH3

biomarker measured over the lifetime of the endotoxic mouse model may well represent the time-course development of the biological process responsible for CitH3 release from NETs into circulation. Generally, to provide timely and precise treatment of sepsis, it is critical to discriminate infectious inflammation from non-infectious inflammation at an early stage. However, they both represent alterations during common inflammatory stress responses and can be hardly differentiated well at an early state through conventional assay processes [170]. The iNOBS data obtained for two different types of mouse models indicate that CitH3 measurement can significantly distinguish between infectious and non-inflammatory responses [146, 171].

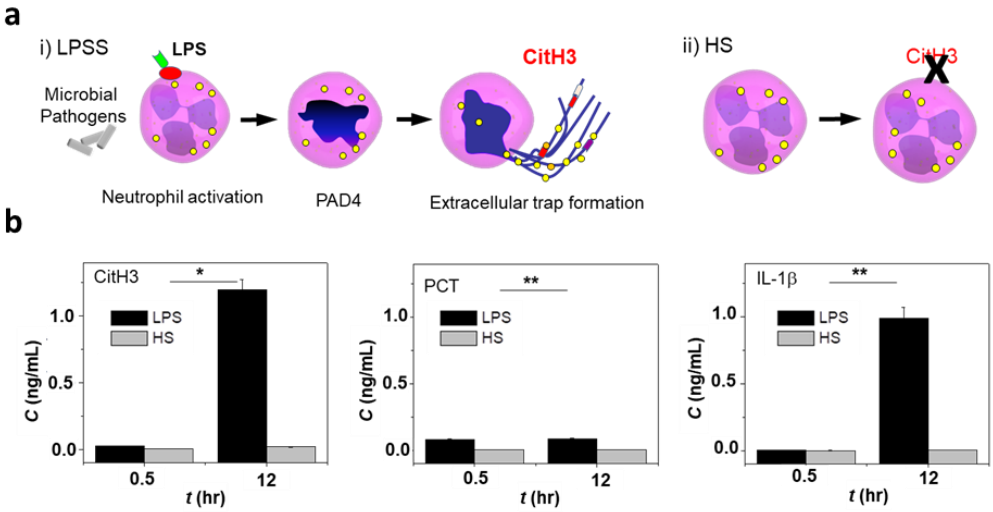

Figure 4.15 (a) Illustration of neutrophil behaviors in LPSS and HS models. CitH3 is a specific biomarker used to distinguish the LPS condition from the HS condition. (b) C_{CitH3}, C_{PCT}, and $C_{IL\text{-}1\beta}$ measured for LPS and HS mouse models (n = 20, $*p < 0.005$ and $**p < 0.05$). In the test, the HS mouse was subjected to 30% blood loss without resuscitation, and its blood samples were collected at 0, 0.5, and 12 h after the HS procedure.

4.4 Summary

Unlike cancer and other chronic diseases, infection-induced sepsis can rapidly and dynamically evolve. Management of severe sepsis imposes stringent requirements on

diagnosis in terms of speed and sensitivity [172]. In this study, we developed a miniaturized biosensor platform for detecting CitH3, a circulating sepsis biomarker released by neutrophils upon the first-line immune defense activity against infection. The biosensor monolithically integrated highly ordered, uniform, and packed self-assembled antibody-functionalized AuNH arrays and a highly photoresponsive few-layer MoS_2 photoconductive channel into a small chip. We functionalized the AuNH arrays with a new high-affinity CitH3 monoclonal antibody developed by our lab. The unique combination of the nanoscale plasmonic structure, antibody, and two-dimensional (2D) material permitted self-contained photoelectronic label-free detection of serum CitH3 with high speed, high sensitivity, high accuracy, and a large detection range. This study applied the remarkable performance of the iNOBS to demonstrate our capability of monitoring circulating CitH3 and other biomarkers *in situ* in a living mouse in the sepsis mouse model after LPS-induced endotoxic shock. From its biological basis and measured time-course profile, CitH3 is expected to provide a more accurate signature of infection-induced inflammation than PCT, which has been used in the conventional clinical diagnosis of sepsis. Recognizing the heterogeneity of septic conditions and inter-patient variability, there is a need for shifting clinical management of infections towards personalized treatment [173-174]. The material processing used for the iNOBS construction is scalable for a fully standalone biosensor module for massively parallel analysis of multiple biomarkers at the point of care. The highly miniature iNOBS device may be eventually incorporated into a fully handheld portable POC diagnostic module without requiring any bulky off-chip signal reader or instrument. This module would enable clinicians to monitor temporal biomarker profiles of patients in real-time and facilitate a biomarker-guided precision/personalized therapy of infections in a timely manner.

Chapter 5

Rubbing-Induced Site-Selective Growth (RISS) of MoS_2 Device Patterns

5.1 Introduction

The interest in emerging 2D-layered transition metal dichalcogenides (TMDCs, *e.g.,* MoS_2, WSe_2, and WS_2) has soared due to their excellent electronic and mechanical properties, which could be exploited to fabricate a wide variety of functional devices with unprecedented and attractive functionalities [175-180]. In the fabrication of TMDC-based devices, the TMDC flakes are mechanically transferred (or printed) from a bulk ingot to the substrate, or the TMDC films are grown on the substrate using deposition methods such as chemical vapor deposition (CVD) and atomic-layer deposition (ALD) [181-187]. However, to manufacture commercially-viable arrays of TMDC devices with consistent characteristics, the sizes and locations of TMDC device features must be well controlled in the fabrication. Therefore, additional resist-based lithography and plasma-based etching processes need to be performed to pattern as-deposited TMDC layers into functional device features. It is worthwhile to note that such device patterning processes inevitably introduce a broad range of contaminants that complicatedly modify and degrade the transport characteristics of electronic devices. The transfer characteristics of TMDC-based devices are especially sensitive to these contaminants because of their

atomically thin structures [52, 188-191]. More seriously, conventional semiconductor cleaning approaches (*e.g.,* RCA and piranha methods) cannot safely eliminate such lithography-introduced contaminants without causing additional chemical/physical damages to TMDC patterns. This is because of the fact that atomically-thin TMDC structures are very fragile in these cleaning reagents, and also because of the fact that most layered materials with 2D surfaces have a weak adhesion to dielectric substrates and are easily peeled off by the bubbling of gases during the cleaning processes [192-193]. Therefore, although deposition-lithography-etching-metallization method is being widely used in the industry for processing conventional semiconductor structures, it is still not suitable for producing 2D-layered semiconductor devices.

To address such a general challenge in the patterning of emerging layered materials, it is highly desirable to develop site-selective growth techniques capable of directly generating TMDC and other layered-material-based device patterns, without need of (or with a minimal usage of) additional lithography and etching processes. Han et al. reported using patterned nucleation seeds to grow MoS_2 crystals at predetermined locations using CVD [194]. Sun et al. demonstrated the site-selective growth of MoS_2 structures within pre-patterned topographical features [195]. More recently, Xiang et al. demonstrated the selective growth of MoS_2 on a chemically treated substrate [196]. In these previously reported methods, some types of guiding features must be introduced onto the substrates for realizing site-selective growth. A potential concern is that these guiding features cannot be removed after the fabrication and might also lead to complicated effects on the device performance. Therefore, additional efforts are needed to explore the viability of a method capable of directly generating MoS_2 patterns without introducing any permanently existing features on the substrates.

In this chapter, we present a rubbing-induced site-selective growth (RISS) method capable of producing few-layer MoS_2 patterns without need of additional patterning steps. Such a lithographic capability for generating MoS_2 device structures has not been reported yet. In a RISS process, a SiO_2 growing substrate is firstly rubbed by a motorized rubbing template bearing topographic structures, which generates surface charge patterns due to the triboelectric effect. Afterwards, the rubbed SiO_2 substrate is loaded into a CVD tube, and few-layer MoS_2 patterns are selectively grown within the rubbed areas on the

SiO_2 substrate. In this work, the fabrication of MoS_2 line/spacing patterns with different periods ranging from 200 nm to 20 μm has been specifically demonstrated. Kelvin probe force microscopy (KPFM) analysis in combination with finite element analysis (FEA) simulation shows that the RISS-produced MoS_2 patterns are well correlated to the triboelectric field distribution within rubbed surface areas. Furthermore, the RISS-produced MoS_2 line/spacing features have been utilized for making arrays of field-effect transistors (FETs) and lateral two-terminal memristors. These devices exhibit a high yield of ~76 % and a good device-to-device consistency in their critical performance parameters. Specifically, the fabricated FETs exhibit reasonably high on/off ratios in the range of 10^3 to ~ 10^6 and an average field-effect mobility of 0.18 ± 0.17 $cm^2/(Vs)$. The memristors made from RISS-produced MoS_2 channels exhibit a low threshold field magnitude (~10^4 V/cm) for initiating memristive switching courses, a high switching ratio of ~ 8, and a small relative standard deviation (~ 3 %) in the set/reset currents measured from multiple memristors.

5.2 Experimental Setup for RISS Process

5.2.1 Design of the Rubbing-Induced Site-Selective (RISS) Growth Process

Figure 5.1 illustrates our setup for demonstrating rubbing-induced site-selective growth (RISS). Specifically, Figure 5.1 (a) schematically illustrates our lab-made tool for generating triboelectric charge patterns on a dielectric substrate through a rubbing process. In such a rubbing process, a rubbing-purposed template bearing topographic features is obliquely mounted on a holding arm. When a mass weight is added to the holding arm, the edge of the rubbing template is brought into contact with the substrate, and the contact force between the template and the substrate can be well controlled by adjusting the mass weight added to the holding arm. Carried by a motorized stage, the substrate moves in respect to the rubbing template, and the topographic features at the template edge gently rub the substrate. In case that the template and the substrate are made from materials with different triboelectricity coefficients, triboelectric charge is

generated within the rubbed regions on the substrate. In principle, this rubbing tool could generate arbitrary triboelectric charge patterns through a combination of the design of the rubbing template features and the control of the stage motion. However, in this work, we specifically use the templates bearing line/spacing features (period: 200 nm - 20 μm; duty cycle: 50%) for experimentally demonstrating RISS and investigating its fundamental processing characteristics, as illustrated by the magnified inset view in Figure 5.1 (a).

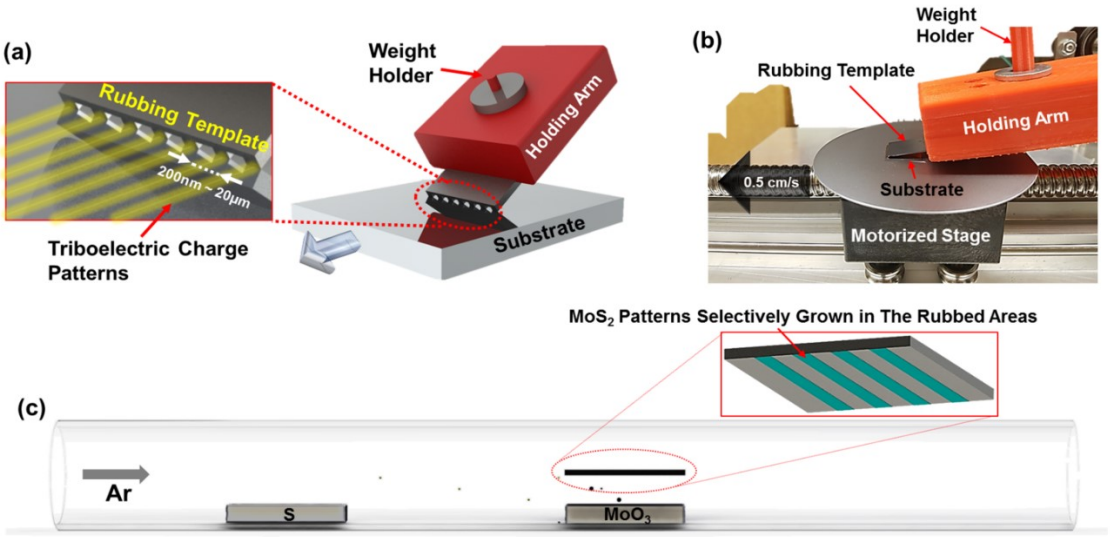

Figure 5.1 Setup of the rubbing-induced site-selective growth (RISS) process: (a) schematic illustration of a rubbing tool for generating triboelectric charge patterns on a target substrate; (b) photography of a lab-made rubbing tool; (c) illustration of the site-selective CVD growth of few-layer MoS_2 patterns on a RISS-processed substrate.

In addition, the line/spacing features can be generically exploited to make a broad range of densely arranged electronic devices, such as thin-film transistors (TFTs), memories, memristors, and multiplexing biosensors. Figure 5.1 (b) shows a photograph of our lab-made rubbing tool. In this rubbing tool, the holding arm is made of polylactic acid (PLA) plastic and fabricated by using a 3D printer. A motorized stage controlled by an Arduino™ microcontroller is used for generating precisely controlled translational motion of the substrate in respect to the rubbing template. The moving speed of the stage is set to 0.5 cm/s during a rubbing process. After a rubbing process, the substrate with

rubbing-induced triboelectric charge patterns is loaded into a chemical vapor deposition (CVD) for performing selective growth of MoS_2 patterns, which is mediated by the electric field generated by the charge patterns, as illustrated in Figure 5.1 (c). RISS is a scalable nanofabrication process and could be used for manufacturing MoS_2 device patterns over large areas.

5.2.2 Fabrication of a Rubbing Template and Chemical Vapor Deposition (CVD) Process

First, a photoresist (SPR 220) layer is spin-coated on a Si substrate. After a baking process at 115 ^{o}C for 5 min, the photoresist-coated Si substrate is aligned with a photomask bearing line/spacing patterns and exposed to UV light by using an aligner (MA6/BA6 mask aligner). After the development process, the Si substrate is etched in a plasma etcher (LAM9400) (Etching condition: RF Power of 600 W, HBr flowrate of 100 sccm, He flowrate of 100 sccm). For all line/spacing patterns, the etching depth is 5 μm. Specifically, Figure 5.3 (a) and (b) display the optical micrograph (OM) and tilted-view scanning electron micrograph (SEM) of a Si-based rubbing template bearing line/spacing features with period of 20 μm, protrusive line width of 10 μm, depth of 5 μm, and duty cycle of 50%, respectively. This template is used for rubbing the substrate and generating triboelectric charge patterns. In our experiments, we found that the rubbing between Cu and SiO_2 surfaces results in very prominent triboelectric effect. This is because Cu and SiO_2 have completely opposite triboelectric polarities and stay quite far away from each other on the triboelectric series, as shown in Figure 5.2. In addition, Cu is chosen as the material for making rubbing templates also because of its high compatibility with low-cost deposition processes, good mechanical and chemical stabilities, as well as large abundance. Therefore, the rubbing template is coated with 5 nm Cu by electron-beam evaporation, aiming to generate prominent and consistent triboelectric charge patterns on SiO_2 substrates.

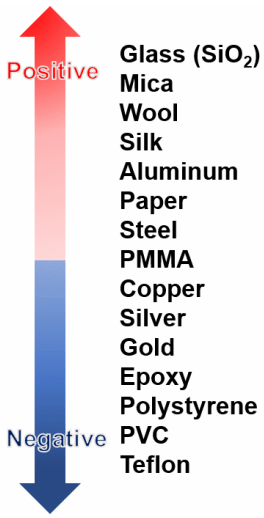

Figure 5.2 Triboelectric series of materials.

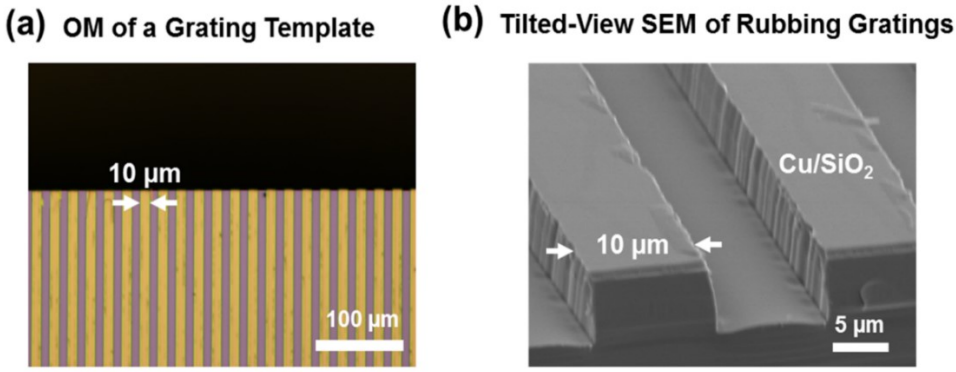

Figure 5.3 (a) optical micrograph (OM) and (b) tilted-view scanning electron micrograph (SEM) of 20 μm period Cu-coated Si rubbing template (protrusive linewidth: 10 μm, feature height: 5 μm).

In a CVD process, 10 mg of Molybdenum trioxide (MoO_3, 99.97%, Sigma Aldrich) and 300 mg of Sulfur (S, 99.5%, Sigma Aldrich) are placed at the center and upstream locations of a 1"-Dia. quartz tube, respectively. The SiO_2 or other dielectric substrates bearing rubbing-induced triboelectric charge patterns serve as the target substrates. These substrates are placed face-down above the MoO_3 source. Ar (99.999%, Cryogenic Gases) is used as the carrier gas, and the gas flow rate is set to 150 sccm during the synthesis course. The temperature of the central area of the furnace chamber rises to 800 °C and maintains the same for 5 min during the MoS_2 synthesis. Afterwards,

the furnace is cooled to the room temperature, and the substrates bearing RISS-produced MoS_2 patterns are taken out from the quartz tube.

5.2.3 Image Processing Steps for Extracting the MoS_2 Cover Ratio from SEM Images

Figure 5.16 demonstrates an image processing course for extracting the MoS_2 cover ratio data from a SEM image of RISS-produced MoS_2 lines. Specifically, the original SEM image is first converted to a gray-scale image using MATLAB™. Each pixel in the converted gray-scale image has an analogue brightness value ranging from 0 (darkest) to 255 (brightest). Afterwards, the gray-scale image is converted to a binary image (*i.e.,* black-and-white image) by using Otsu's algorithm [197]. Specifically, the pixels with brightness values higher and lower than 127 are set to Bit-"1" and Bit-"0", respectively. In the binary image, the Bit value of each pixel is either "1" (*i.e.*, white pixel representing a blank SiO_2 surface pixel) or "0" (*i.e.*, black pixel representing a pixel area covered by RISS-produced MoS_2). A typical binary SEM image consists of 1,280 (width) × 960 (height) pixels, as shown in Figure 5.16. Therefore, there are 1,280 vertical sample lines and each sample line contains 960 pixels in a binary image. Since each pixel on a vertical sample line is set to either "1" or "0", the summation of all pixel values on this vertical line gives out the number of blank SiO_2 surface pixels (N_{SiO2}) for this sample line position. Subsequently, the number of surface pixels covered by RISS-produced MoS_2 (N_{MoS2}) for this sample line can be obtained by subtracting the number of blank SiO_2 surface pixels (N_{SiO2}) from the total number of pixels (N_{Tot}: 960) on this vertical line. The local MoS_2 cover ratio (N_{MoS2}/N_{Tot}) for this vertical sample line is defined as the ratio between N_{MoS2} and N_{Tot} acquired from this line, as denoted in Eqn. 1. For a typical binary SEM image, totally 1,280 cover ratio (N_{MoS2}/N_{Tot}) values are calculated and plotted as the function of 1,280 vertical sample line positions.

$$\text{Cover Ratio (\%)} = \frac{N_{MoS2}}{N_{Tot}} \times 100 = \frac{N_{Tot}\text{-}N_{SiO2}}{N_{Tot}} \times 100 \qquad (1)$$

5.3 Experimental Results of the RISS Method and Its Applicational Devices

5.3.1 Analysis of the Rubbing Process of the RISS Method

Figure 5.4 shows the Kelvin probe force microscopy (KPFM) characterization of the triboelectric charge pattern formed on a SiO_2 substrate. the substrate is rubbed by the line/spacing template under a contact force of 100 mN (the corresponding contact gauge pressure is 443.5 MPa, which is estimated using the method described below). Figure 5.4 (a) displays the topographic atomic force microscopy (AFM) image of the rubbed area on

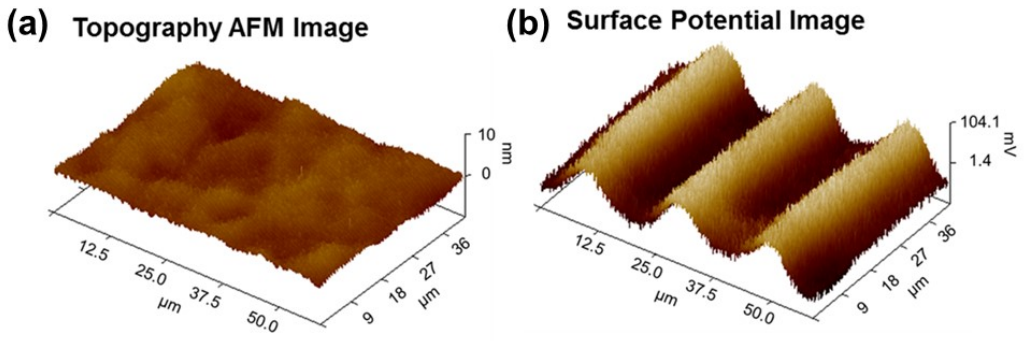

Figure 5.4 (a) topography AFM image of the SiO_2 surface area rubbed by the rubbing template under a contact pressure of 443.5 MPa, which does not show any visible rubbing-induced damage to the surface; (b) KPFM image (*i.e.,* surface potential image) of the same surface area, which clearly exhibits a high-contrast grating-like potential profile, highly correlated to the features on the rubbing template.

the SiO_2 substrate, which does not exhibit any rubbing-induced mechanical damage to the SiO_2 surface. Figure 5.5 shows that the root-mean-square (RMS) values of surface roughness (R_q) measured from both rubbed and un-rubbed areas on a SiO_2 surface do not exhibit a statistical difference. Figure 5.6 displays the energy-dispersive X-ray spectra (EDS) (Figure 5.6 (a)) and contact angle measurement results (Figure 5.6 (b)) acquired from a SiO_2 surface before and after rubbed by a Cu rod template (the rubbing pressure is ~500 MPa). These additional surface characterizations show that the rubbing process does not result in a noticeable Cu contamination or modification of surface wettability.

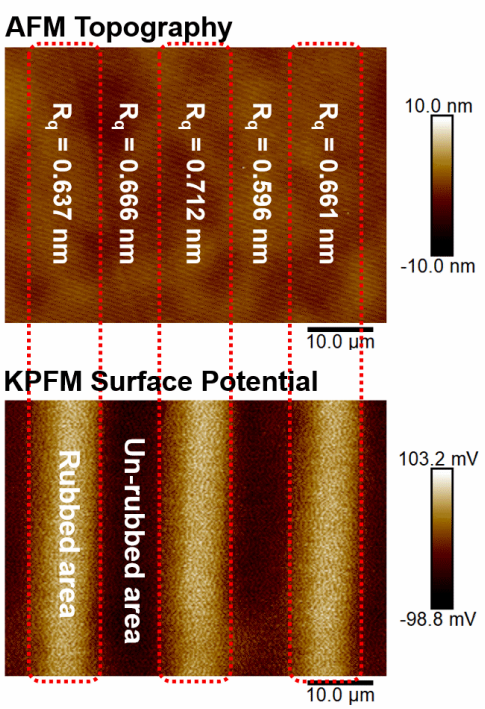

Figure 5.5 Root mean square roughness (R_q) values measured from rubbed and un-rubbed areas on a SiO_2 surface.

Figure 5.4 (b) shows the KPFM image (*i.e.,* surface potential image) of the same rubbed area on the substrate. This KPFM image clearly shows a grating-like pattern of electric potential, which is highly consistent with the line/spacing feature on the rubbing template and is reasonably attributed to the triboelectric charge induced by the rubbing between

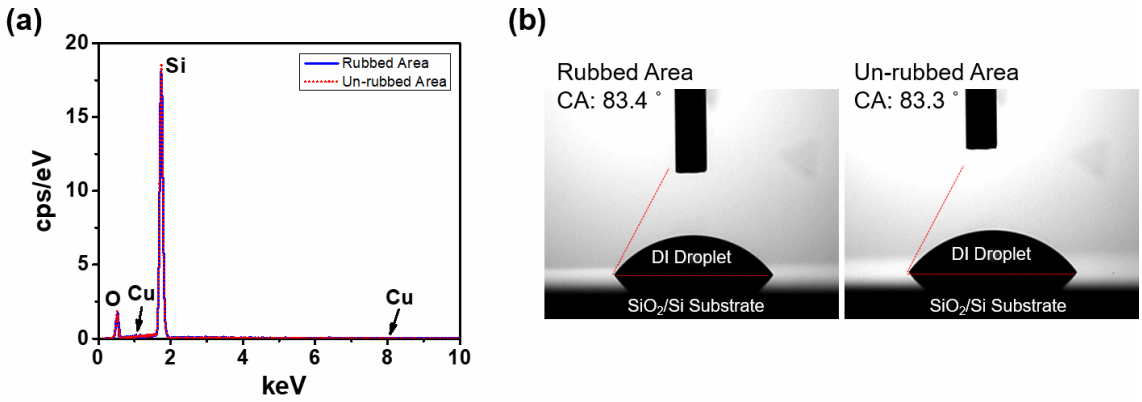

Figure 5.6 Surface characterizations of a SiO_2 surface rubbed by a Cu rod template: (a) EDS spectra and (b) water contact angles measured from the SiO_2 surface before and after rubbed by the Cu rod template.

the Cu-coated line/spacing template and the SiO_2 substrate [22]. In this rubbing test, the resulted peak-to-valley amplitude of potential fluctuation on the SiO_2 substrate is measured to be ~ 100 mV, which is the typical condition for the subsequent site-selective CVD growth of MoS_2 patterns. We further investigated the effect of heat treatment on the surface potential induced by triboelectric effect. Figure 5.7 shows the KPFM surface potential images of a rubbed SiO_2 surface captured before and after heat treatment. Specifically, Figure 5.7 (a) shows the photograph of a CVD furnace tube (filled with 150 sccm of Ar gas), in which a SiO_2 substrate rubbed by a Cu rod template is subjected to a heat treatment process at 800 ºC for 3 min. Figure 5.7 (b) shows the KPFM surface potential image of the SiO_2 surface before heat treatment. In Figure 5.7 (b), the white line denotes a potential profile, from which the peak value of surface potential is measured to be ~ 56.1 mV. Figure 5.7 (c) displays the KPFM surface potential image of the same SiO_2 surface after heat treatment. Figure 5.7 (c) shows that after heat treatment, the peak value of surface potential is measured to be ~15.6 mV, which is ~70 % lower than that measured before heat treatment. Such a heat-induced reduction of surface potential is attributed to the thermally enhanced diffusion of charged carriers on the SiO_2 surface. Nevertheless, the rubbing-induced surface potential, even after heat treatment at a typical growth temperature (~800 ºC), is still prominent and can serve as effective triboelectric charge patterns for inducing selective MoS_2 growth.

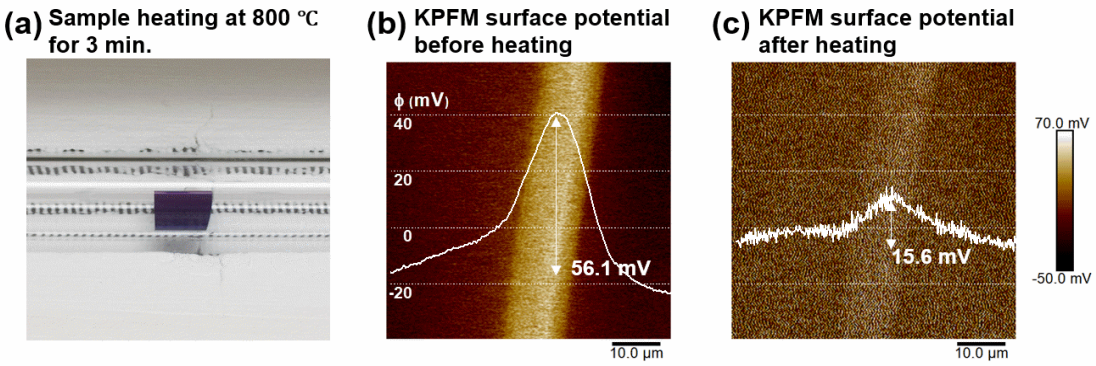

Figure 5.7 Effect of heat treatment on triboelectric field: (a) photography of a SiO_2 substrate loaded into a CVD tube (heating temperature: 800 ºC); (b) KPFM surface potential image of a as-rubbed SiO_2 surface before heat treatment (the white line denotes a potential profile); (c) KPFM surface potential image of the same SiO_2 surface after heat treatment.

Given the template/substrate materials that rub to each other, the resulted triboelectric charge density, field magnitude, or surface potential on the dielectric substrate are expected to depend on the applied contact force (or gauge pressure) between the template and the substrate [198-199]. To obtain a precise control of the RISS processes, we investigated the functional relationship among surface potential (φ), contact force (F), and contact pressure (P) through KPFM analysis in combination with finite element analysis (FEA) modeling. Specifically, in this study we used a cylindrical Cu rod (diameter: 0.5 mm) instead of the line/spacing structures as the rubbing template. This is because the mechanical deformation of a cylindrical rod template can be easily simulated for precisely quantifying the effective contact area (A) as well as gauge pressure (P) between the template and the substrate. We assume that the φ – P relationship acquired from this cylindrical Cu rod template is also applicable to other Cu-coated templates. Figure 5.8 (a) displays a series of KPFM images captured from the SiO_2 surface areas rubbed by the same Cu rod exerted with different contact forces (*i.e.,* F = 29.4, 73.5, 140.2 and 242.3 mN). The resulted surface potential (φ) values are extracted from these KPFM images and plotted as a function of contact forces in Figure 5.8 (b). Because during the rubbing experiment, it was extremely hard to directly measure the effective contact area (A) between the rod template and the substrate, we established a FEA model and used a commercial FEA software package (ABAQUS^{TM}) to evaluate the effective contact area values under different contact forces. Figure 5.8 (c) illustrates the FEA model, in which the cylindrical Cu rod template (diameter: 0.5 mm) is inclined by 45˚ and its edge is in contact with the underlying SiO_2 surface. This model is consistent with the corresponding experimental setup. Figure 5.8 (d) shows a representative FEA result of the gauge pressure distribution at the template/substrate interface under a contact force of 29.4 mN. The corresponding contact area (A) and average contact pressure (P) between the template and the substrate can be extracted from such a FEA result. Figure 5.8 (e) plots the FEA-calculated contact areas (A) with respect to the corresponding contact forces (F) applied in the experiment, from which the corresponding average contact pressures (P) can be also calculated. Figure 5.8 (f) plots KPFM-measured surface potential (φ) values versus FEA-calculated contact pressures (P). Such φ-P data can be tentatively fitted by an empirical polynomial function ($\varphi = 6 \times 10^{-6} P^3 - 0.0048 P^2 + 1.44$

P - 119.9), as denoted by the red dashed line in Figure 5.8 (f). This φ-P curve could be used for determining the contact gauge pressure required for generating the triboelectric charge pattern with a given surface potential and also determining if such a rubbing condition induces any damage to the substrate. For example, in this work we identified that the triboelectric charge patterns with surface potential of 100 mV can result in effective site-selective growth of MoS_2 patterns. Based on the φ-P curve in Figure 5.8 (f),

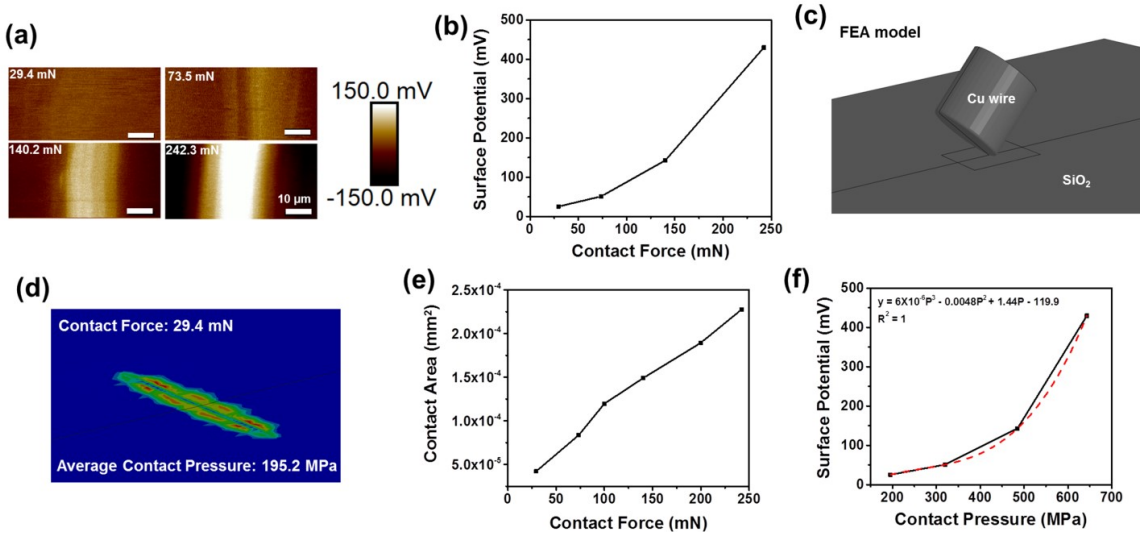

Figure 5.8 KPFM analysis in combination with finite element analysis (FEA) to investigate the functional relationship among surface potential (φ), contact force (F), and contact pressure (P): (a) KPFM images captured from SiO_2 surface areas, which were rubbed by a Cu rod template under different contact forces of 29.4, 73.5, 140.2, and 242.3 mN, respectively; (b) KPFM-measured surface potentials (φ) *versus* corresponding applied contact forces (F); (c) illustration of the FEA model for simulating the contact between the Cu rod template and the SiO_2 surface; (d) FEA-calculated distribution of the gauge pressure at the Cu/SiO_2 interface under a contact force of 29.4 mN; (e) FEA-calculated effective contact areas (A) plotted as a function of contact forces (F); (f) KPFM-measured surface potentials (φ) plotted as a function of corresponding FEA-calculated contact pressures (P), which can be fitted by an empirical polynomial function ($\varphi = 6 \times 10^{-6} P^3 - 0.0048 P^2 + 1.44 P - 119.9$), as denoted by the red line.

the gauge pressure required for performing the rubbing process to generate such charge patterns is estimated to be 443.5 MPa. This pressure value is about a quarter of magnitude lower than the compressive strength of SiO_2 and does not cause serious

damage to the SiO_2 substrate, as indicated by the AFM result in Figure 5.4 (a). The contact pressure exerted during a rubbing process cannot exceed the compressive strength (σ_c) of the substrate (*e.g.,* for a SiO_2 substrate, σ_c is the range of 1.1 ~ 1.6 GPa). Given such a maximum possible contact pressure value, the corresponding maximum surface potential can be estimated by using our empirical polynomial function discussed above (*i.e.*, $\varphi = 6 \times 10^{-6} P^3 - 0.0048 P^2 + 1.44 P - 119.9$). Using this empirical function, the maximum surface potential value is estimated to be around 3.6 V.

5.3.2 RISS-Produced MoS_2 Line/Spacing Patterns

Figure 5.9 displays the SEM images of a series of RISS-produced few-layer MoS_2 line/spacing patterns with different periods/effective linewidths ((a) 20 μm/10 μm, (b) 10 μm/5 μm, (c) 2.5 μm/~450 nm, (d) 2 μm/~290 nm, and (e) ~250 nm/not applicable). Here, the effective linewidth of a RISS-produced MoS_2 line is defined as the average linewidth of the region, in which MoS_2 grains are connected to each other to form a continuous channel line, not including the dispersed MoS_2 grains around this continuous line. For all MoS_2 line/spacing patterns, their periods are consistent with the periods of the corresponding rubbing template features. This indicates that in a RISS process, the rubbing by the Cu-coated template can induce site-selective growth of MoS_2 features on the rubbed SiO_2 substrate. The grain sizes of RISS-produced few-layer MoS_2 line/spacing patterns are in the range of 200 ~ 300 nm, as indicated by the SEM images in Figure 5.10. Such relatively small grain sizes are attributed to the abundant nucleation sites within the rubbed areas on the SiO_2 surface, which limits the average range of lateral epitaxial growth of MoS_2 features [196, 200]. The average thickness of RISS-produced MoS_2 lines is 3.55±0.67 nm, which is measured from the MoS_2 lines distributed over a ~ 0.25 cm^2 area by using atomic force microscopy (AFM). The representative AFM image and the extracted statistical thickness data are presented in Figure 5.11. Figure 5.12 further shows Raman characterization results of few-layer MoS_2 lines produced by a RISS process. Specifically, Figure 5.12 (a) displays the optical micrograph of RISS-produced MoS_2 lines with period/linewidth of 10μm/5μm. Figure 5.12 (b) displays the Raman spectrum

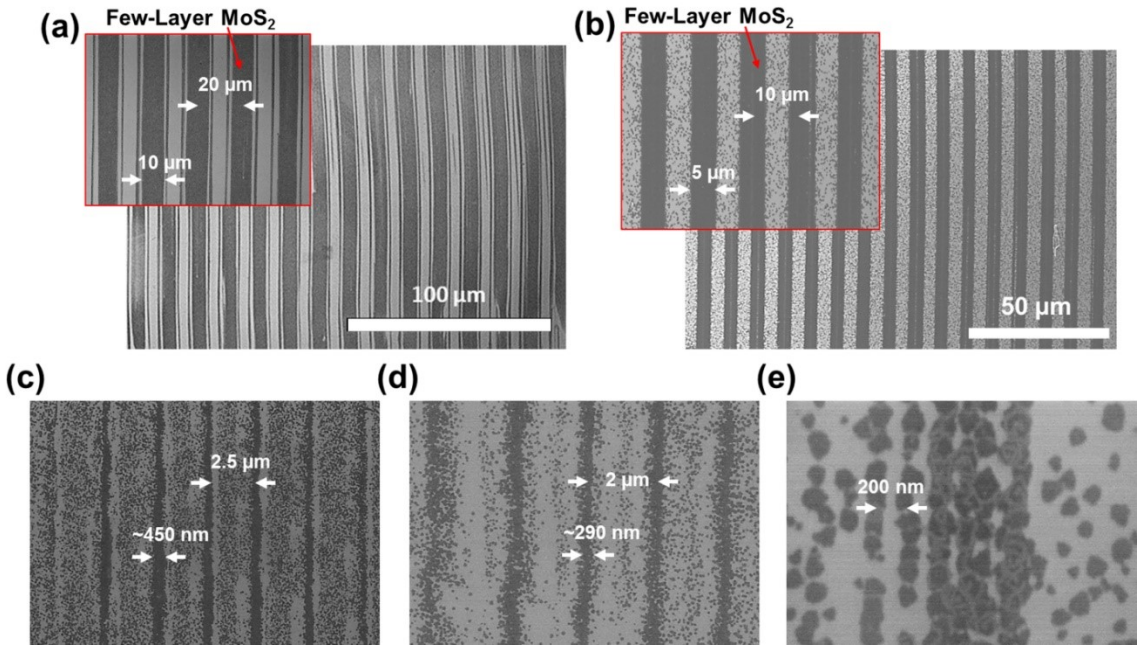

Figure 5.9 SEM images of representative RISS-produced few-layer MoS_2 lines with different periods/linewidths of (a) 20µm/10µm, (b) 10µm/5µm, (c) 2.5µm/~450nm, (d) 2µm/~290nm, and (e) ~250 nm/not applicable.

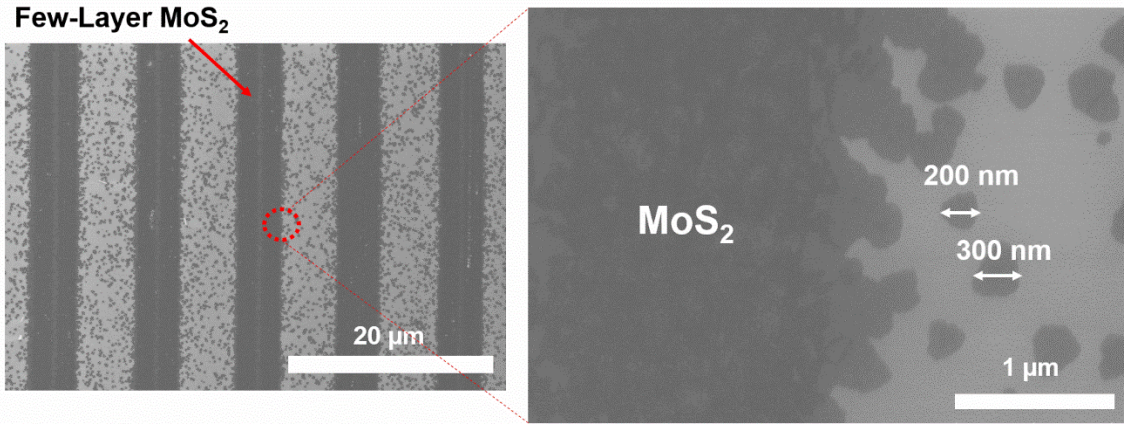

Figure 5.10 SEM images of RISS-produced MoS_2 lines with period/linewidth of 10µm/5µm. The zoomed SEM image shows the edge of a representative MoS_2 line, where MoS_2 grain sizes are measured to be in the range of 200 ~ 300 nm.

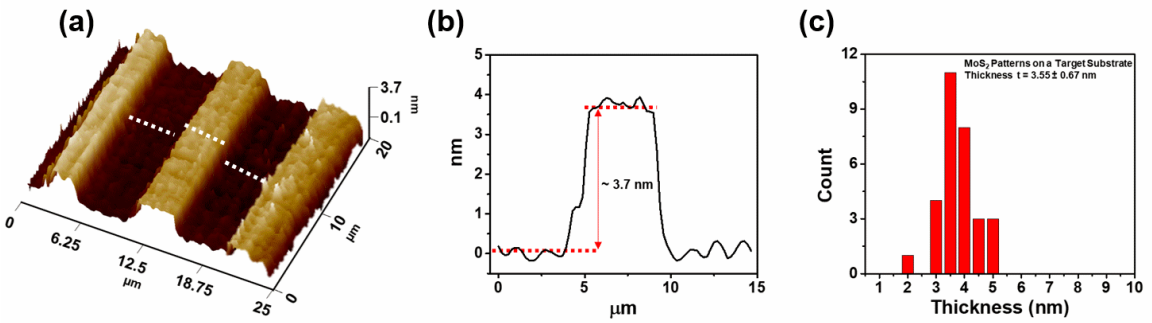

Figure 5.11 (a) Representative AFM topography image of a set of MoS_2 lines with average linewidth of 5μm; (b) scanline profile of a representative MoS_2 line; (c) stacked column chart of the statistical thickness data obtained from 30 MoS_2 lines grown over a ~ 0.25 cm^2 area on the SiO_2 surface.

acquired from the central region of a MoS_2 line (excitation laser wavelength: 532 nm), which exhibits two Raman scattering peaks associated with two characteristic phonon modes of MoS_2 layers (*i.e.*, E^1_{2g} and A_{1g} peaks appearing at ~ 383 cm^{-1} and ~ 407 cm^{-1}, respectively). Based on the spacing between these two peaks (~ 24 cm^{-1}) in combination with their positions, the thicknesses of RISS-produced MoS_2 lines are estimated to be in the range of 4 – 5 layers [201-202], which is in good agreement with our AFM-measured thickness data shown in Figure 5.11. Figure 5.12 (c) and (d) display the Raman mapping images of MoS_2 lines based on E^1_{2g} and A_{1g} modes, respectively. These two images show that strong E^1_{2g} and A_{1g} scattering signals only appear within the rubbed areas. This result further indicates the selective growth capability of RISS. The same Raman spectrum is also plotted with the full Raman shift range in Figure 5.13. This spectrum does not exhibit prominent peaks at 149, 195, 280, 344, 650, and 820 cm^{-1}, which are characteristic features associated with the stretching and bending vibration modes of Mo=O and O-Mo-O bonds [203]. The lack of such modes in combination with the prominent E^1_{2g} and A_{1g} features strongly indicate that most precursor molecules have been well converted to MoS_2 layers in our CVD growth [203].

In this prototype demonstration work, the processing area of our RISS system is at the mm^2 scale, which is mainly limited by the size of the rubbing templates but could be further increased by using larger templates and optimizing the template/substrate contact. Currently, our CVD system cannot enable the precise control of the number of MoS_2

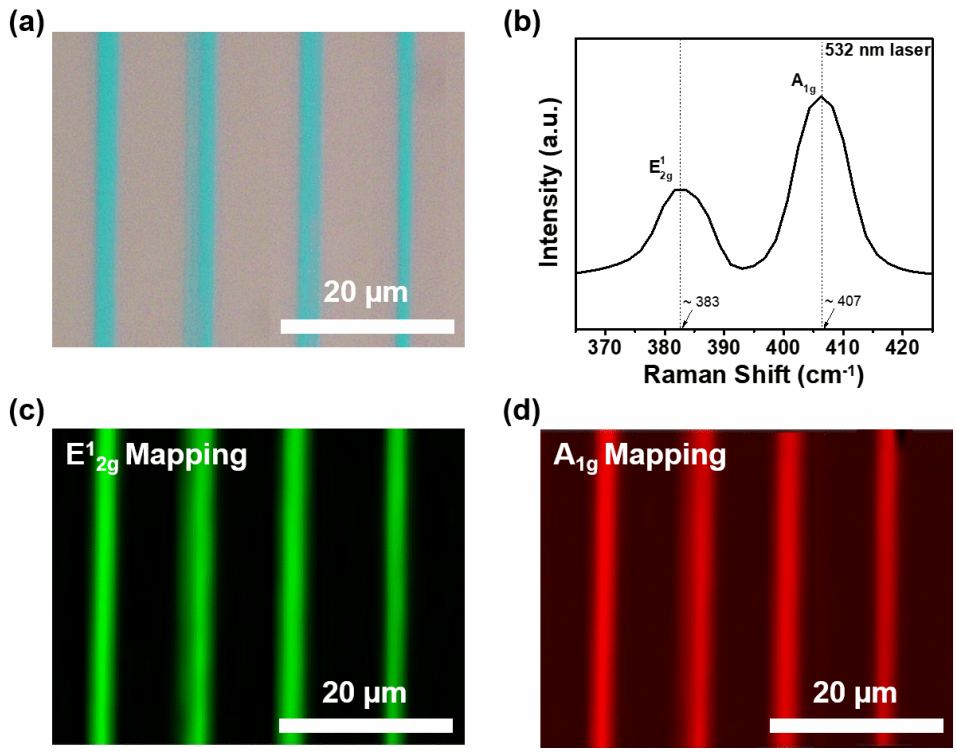

Figure 5.12 Raman characterizations of RISS-produced MoS_2 line structures: (a) Optical micrograph of MoS_2 lines with period/linewidth of 10μm/5μm; (b) Raman spectrum acquired from the central region of a MoS_2 line; (c) and (d) display the Raman mapping images of MoS_2 lines based on E^1_{2g} and A_{1g} modes, respectively.

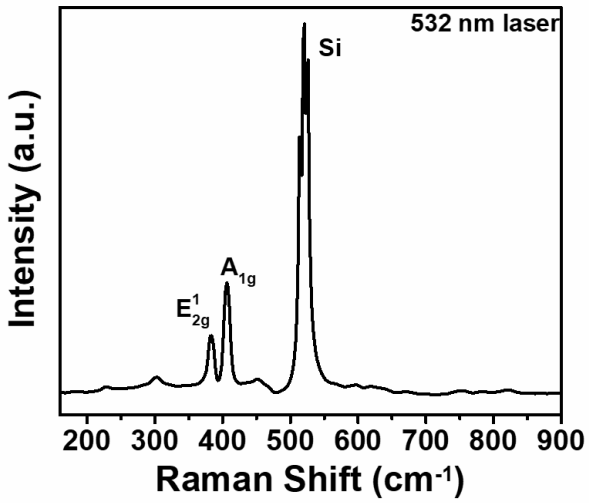

Figure 5.13 Raman spectrum obtained from RISS-produced MoS_2 line structures, which is plotted with the full Raman shift range.

layer. However, such a concern is from a generic challenge about the CVD process and is not directly associated with our RISS method. As demonstrated above, our current RISS process can produce few-layer MoS_2 lines with an average thickness of 3.55±0.67 nm . Such few-layer MoS_2 structures are already useful for a series of device applications, such as thin-film transistors, photodetectors, memories, memristors, and biosensors [176, 180, 204].

5.3.3 Cover Ratio Analysis for Relatively Narrow RISS-Produced MoS_2 Lines

To evaluate the morphological characters of RISS-produced MoS_2 lines, we introduce a specific cover ratio parameter that is defined as the percentage of the local area covered by as-grown MoS_2 layers (or grains). Figure 5.9 shows that for a RISS-produced MoS_2 line, the cover ratio of its central area is high and usually in the range of 80 – 100%, whereas its edge regions exhibit a gradual variation of the cover ratio. For the MoS_2 lines produced by the rubbing features with linewidths larger than 2 μm (*e.g.,* the samples shown in Figure 5.9 (a) and (b)), such a gradual variation of the cover ratio at the feature edges does not significantly affect their effective linewidths, and the effective linewidths of these relatively wide MoS_2 lines are mainly determined by the linewidths of the rubbing template features. However, for the MoS_2 lines produced by the rubbing features with relatively smaller linewidths (*e.g.,* those shown in Figure 5.9 (c), (d), and (e)), such a gradual variation of cover ratio at feature edges results in significantly smaller effective linewidths in comparison with the corresponding linewidths of the rubbing features. As shown in Figure 5.9 (e), the MoS_2 lines produced by a rubbing template with feature period of 200 nm and linewidth of 100 nm are not even continuous due to the overly dispersive variation of MoS_2 cover ratio at the edges.

Such a gradual variation of MoS_2 cover ratio at the edges of RISS-produced features is attributed to the net effect of (1) the field magnitude distribution within rubbing-induced triboelectric charge patterns and (2) the diffusion of nucleated MoS_2 domains from triboelectric charge pattern areas [205]. To quantitatively correlate the spatial distribution of rubbing-induced triboelectric field and the distribution of resulted MoS_2 cover ratio, we used a FEA model to simulate the electric field associated with the

triboelectric charge on a SiO_2 surface and compared this simulated field distribution to the MoS_2 cover ratio profile measured from the SEM image of the corresponding MoS_2 sample. Specifically, a MATLAB^{TM}-based imaging tool was used for processing SEM images and measuring MoS_2 cover ratio profiles, and a COMSOL^{TM} software package

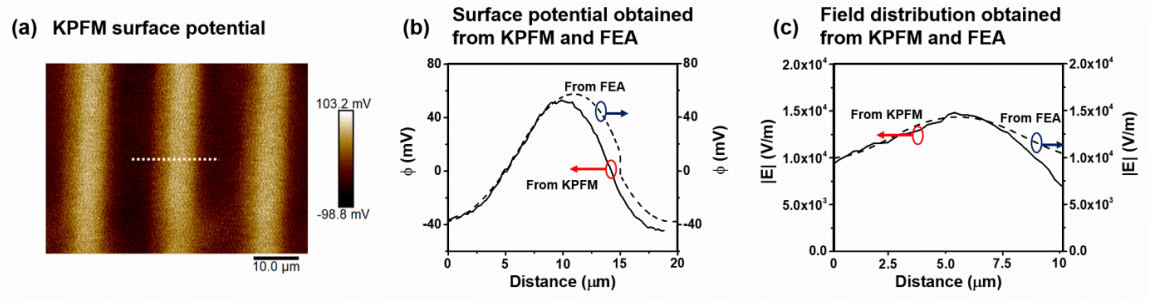

Figure 5.14 Comparison between the electric field distribution measured by KPFM and that simulated by FEA: (a) KPFM image of a SiO_2 surface rubbed by a line/spacing template with period/linewidth of 20μm/10μm; (b) surface potential profiles acquired from KPFM and FEA; (c) field magnitude distribution profiles obtained from KPFM and FEA.

was used for FEA simulation. Figure 5.14 shows the comparison between the electric field distribution measured by KPFM and that simulated by FEA. Specifically, Figure 5.14 (a) shows the KPFM image of a SiO_2 surface rubbed by a line/spacing template with period/linewidth of 20μm/10μm. This KPFM image displays a grating-like surface potential distribution with period of 20 μm. A surface potential profile is captured from the location denoted by a dashed line and plotted as the solid curve in Figure 5.14 (b). In Figure 5.14 (b), the surface potential profile simulated by FEA (dashed curve) is also plotted and compared to that obtained by KPFM. Based on these two surface potential profiles, the profiles of field magnitude distribution obtained from KPFM and FEA are calculated and plotted together in Figure 5.14 (c). Figure 5.14 (b) and (c) indicate that the electric field distribution measured by KFPM is in good agreement with that obtained from FEA simulation. This comparison shows that FEA can serve as a valid tool for simulating and analyzing the electric field involved in a RISS process. Figure 5.15 displays a representative analysis for the MoS_2 lines shown in Figure 5.9 (d), which were produced by using a rubbing template with period of 2 μm and linewidth of 1 μm.

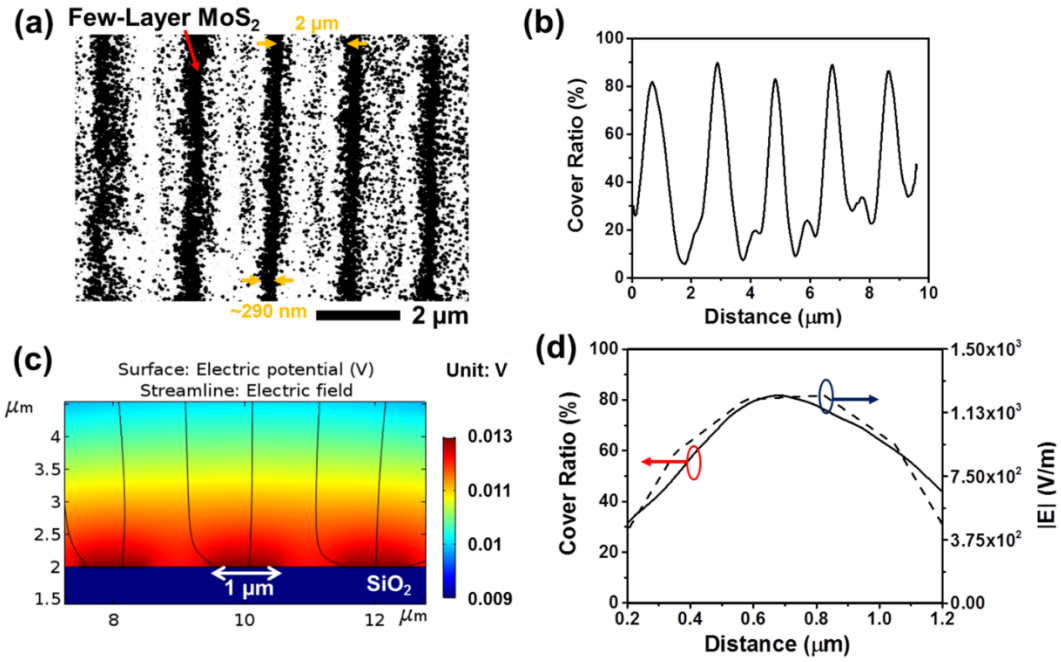

Figure 5.15 Cover ratio analysis for relatively narrow RISS-produced MoS_2 lines (period/linewidth: 2μm/~290nm): (a) binary SEM image of the MoS_2 lines; (b) MoS_2 cover ratio profile across the MoS_2 lines, which are extracted from the binary SEM image; (c) FEA-simulated electric field associated with the corresponding rubbing-induced triboelectric charge pattern (*i.e.*, line/spacing charge pattern with period/linewidth of 2 μm/1 μm); (d) FEA-simulated triboelectric field magnitude profile (dashed line) and SEM-measured MoS_2 cover ratio profile (solid line) around a triboelectric charge line area.

Figure 5.15 (a) shows the binary SEM image processed from Figure 5.9 (d), from which the MoS_2 cover ratio profile across the MoS_2 lines is extracted and plotted in Figure 5.15 (b). Figure 5.16 shows the image processing process to calculate the cover ratio of RISS-produced MoS_2 lines. Specifically, the original SEM image of MoS_2 lines is processed into a binary image using Otsu's algorithm and the local pixels covered by MoS_2 (*i.e.,* the dark pixels shown in the binary SEM image) are counted [197]. The detailed process for extracting the cover ratio profile is described in the supporting information. Figure 5.15 (b) shows that the MoS_2 cover ratio distribution across these relatively narrow MoS_2 line features have a sine-like profile with peak values in the range of 80 – 92 % (*i.e.,* the cover ratios measured from the central regions of the MoS_2 lines) and valley values in the range of 6 – 30 % (*i.e.,* the cover ratios measured from the central regions of the unrubbed

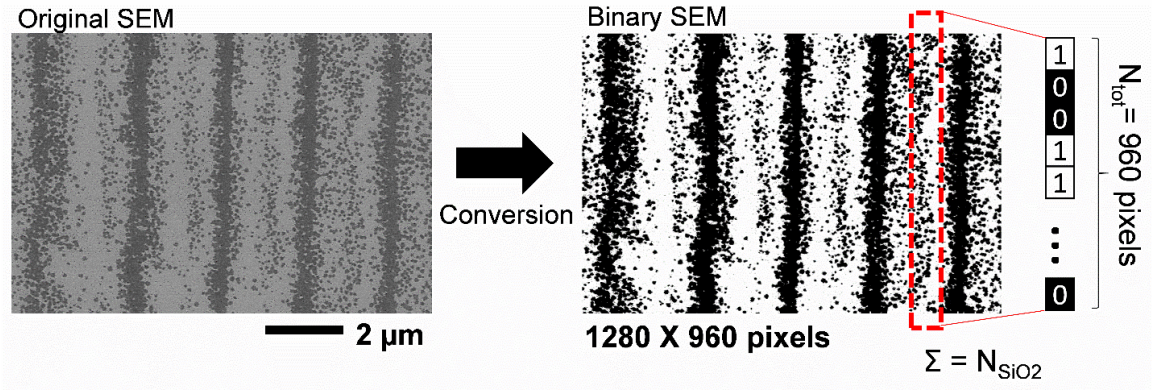

Figure 5.16 Image processing for extracting MoS_2 cover ratio data from a representative SEM image of RISS-produced MoS_2 lines: In the derived binary SEM image, Bit-"1" represents a blank SiO_2 surface pixel (White), and Bit-"0" represents a pixel area covered by RISS-produced MoS_2 (Black).

areas). Figure 5.15 (c) shows the FEA-simulated electric field from the triboelectric charge regions on a SiO_2 surface. In this FEA simulation, we assume a uniform charge density within the rubbed areas, which are 2 μm period, 1 μm wide lines. The value of the charge density is set so that the potential at the central areas of the lines is 100 mV, which is consistent with the potential measured by KPFM, as shown in Figure 5.4 (b). From Figure 5.15 (c), the field magnitude profile around a single charge line is extracted and plotted as a dashed line in Figure 5.15 (d). For comparison, the cover ratio profile measured around a representative MoS_2 line in Figure 5.15 (a) is also plotted as a solid line in Figure 5.15 (d). Figure 5.15 (d) indicates that the spatial distribution profiles of field magnitude and MoS_2 cover ratio around a triboelectric charge line area have very similar shapes and exhibit a strong correlation to each other. Quantitatively, the field magnitude in the middle of a rubbed line is ~ 1.2×10^3 V/m that leads to a local RISS-produced MoS_2 cover ratio of ~ 80 %, whereas the field magnitude at the edges of the rubbed line is ~ 450 V/m that leads to a relatively low cover ratio of 30 – 45%.

5.3.4 Cover Ratio and Thickness Analysis for Relatively Wide RISS-Produced MoS_2 Lines

Figure 5.17 further shows the analysis results for the MoS_2 lines produced by using a rubbing template with period of 10 μm and linewidth of 5 μm (*i.e.,* the sample shown in Figure 5.9 (b)). Figure 5.17 (a) and (b) show the binary SEM image and the extracted MoS_2 cover ratio profile across multiple lines, respectively. These two figures show that for such relatively wide MoS_2 lines (typically those produced by the rubbing features with linewidths larger than 2 μm), the MoS_2 cover ratio is ~ 100 % for the almost entire rubbed area. Such a high contrast of MoS_2 patterns is expected as a result of the high contrast distribution of field magnitude within the rubbed line areas. Figure 5.17 (c) displays the FEA-calculated electric field associated with the triboelectric charge within the 5 μm wide rubbed line areas on a SiO_2 surface. Other simulation parameters are the same as those for the one shown in Figure 5.15 (c). From Figure 5.17 (c), the field magnitude profile across a single 5 μm wide charge line is extracted and plotted as a dashed line in Figure 5.17 (d). This field distribution profile is compared with the cover ratio profile measured around a MoS_2 line shown in Figure 5.17 (a) (*i.e.,* the solid line in Figure 5.17 (d)). Different from the field magnitude profile around a 1 μm wide rubbed SiO_2 line (see Figure 5.15 (c)), the field distribution around a 5 μm wide rubbed line exhibits two peaks at the line edges. The presence of these two peaks makes the electric field magnitude over the entire rubbed area higher than 1.5×10^3 V/m, which results in a high cover ratio of ~100% for almost the whole rubbed area. Figure 5.17 (d) also shows that triboelectric field magnitude and RISS-produced MoS_2 cover ratio exhibit a strong correlation, which is consistent with the field/cover-ratio correlation observed in Figure 5.15 (d) for the relatively narrower MoS_2 lines. This implies that in a RISS process, the local triboelectric field magnitude is a key factor affecting the nucleation of precursor molecules and therefore the local MoS_2 cover ratio.

It is further noted that although a local triboelectric field magnitude higher than 1.5×10^3 V/m makes the local MoS_2 cover ratio saturate to ~100%, different field magnitudes above this saturating value still result in different local MoS_2 thicknesses.

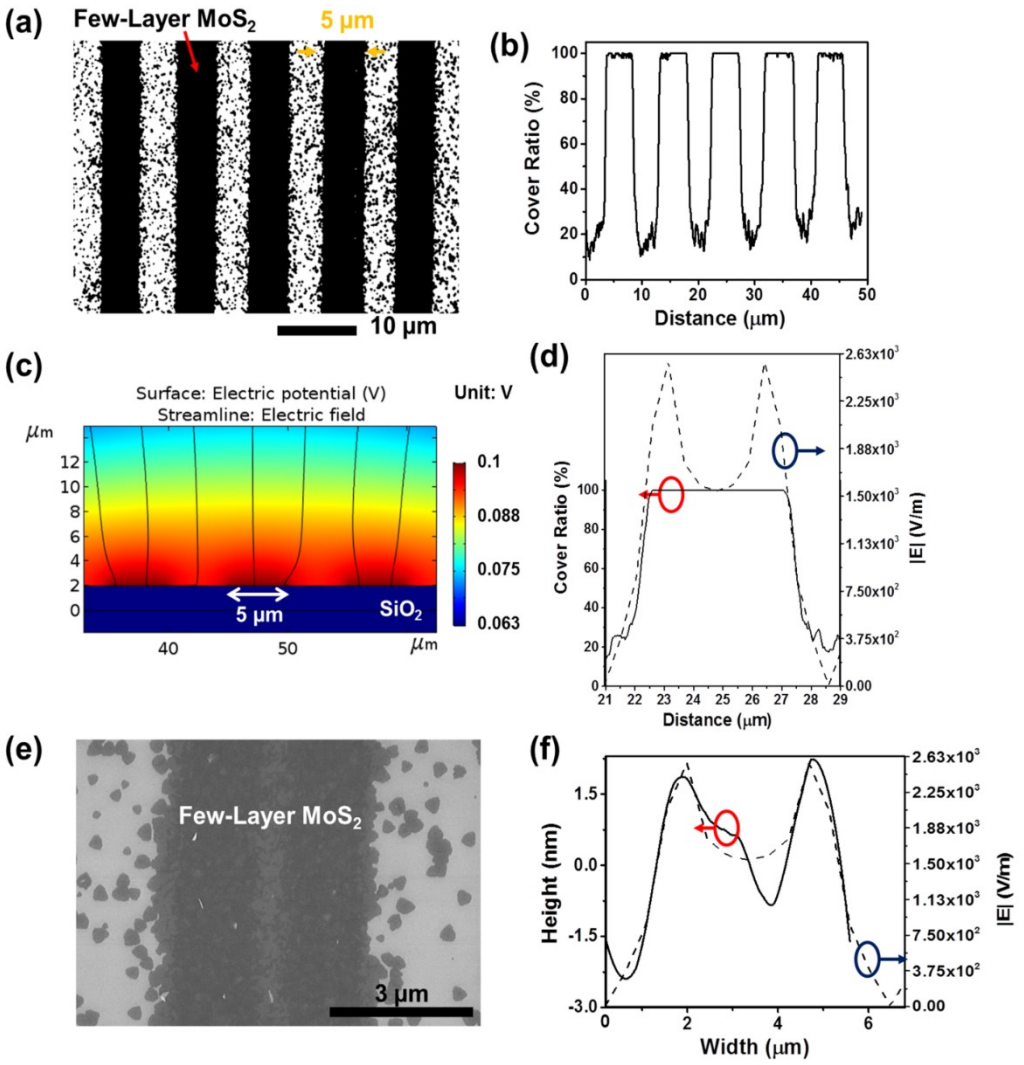

Figure 5.17 Cover ratio and thickness analysis for relatively wide RISS-produced MoS_2 lines (period/linewidth: 10 μm/5 μm): (a) binary SEM image of the MoS_2 lines; (b) MoS_2 cover ratio profile across the MoS_2 lines, which are extracted from the binary SEM image; (c) FEA-simulated electric field associated with the corresponding rubbing-induced triboelectric charge pattern (*i.e.*, line/spacing charge pattern with period/linewidth of 10μm/5μm); (d) FEA-simulated triboelectric field magnitude profile (dashed line) and SEM-measured MoS_2 cover ratio profile (solid line) around a triboelectric charge line area; (e) zoomed SEM image of a 5 μm wide RISS-produced MoS_2 line; (f) AFM-measured height profile (solid line) of the MoS_2 line and FEA-simulated triboelectric field magnitude profile (dashed line).

Specifically, Figure 5.17 (e)shows a zoomed SEM image of a 5 μm wide RISS-produced MoS_2 line. In this SEM image, the darkness distribution across the MoS_2 line implies that

the edge areas of the MoS_2 line are relatively thicker than its central area. This has been further verified by our AFM characterization. Figure 5.17 (f) plots an AFM height profile curve (solid line) acquired across the MoS_2 line as well as a FEA-calculated field magnitude profile. The AFM profile curve specifically indicates that from the center of the MoS_2 line to its edges, the MoS_2 thickness varies from 1.5 nm (~two layers) to 3 nm (~four layers). Such a variation profile for MoS_2 thickness has a very similar shape as that of the field magnitude profile. This further supports our conclusion that in a RISS process, the local triboelectric field magnitude is the key factor affecting the nucleation rate of precursor molecules. Here, it should be also noted that, as shown in Figure 5.17 (a), the MoS_2 cover ratio measured from the unrubbed areas between continuous MoS_2 lines is ~ 20 %, although the triboelectric field magnitude in such unrubbed areas is estimated to be negligible. Therefore, the MoS_2 grains observed in the unrubbed areas are mainly attributed to the lateral diffusion of the MoS_2 grains from the rubbed areas.

5.3.5 Demonstration of an Array of Field-Effect-Transistors (FETs) on RISS-Produced MoS_2 Lines

To evaluate the large-area uniformity of RISS-produced few-layer MoS_2 structures in their electronic properties, we fabricated FET arrays based on RISS-produced MoS_2 lines. To make such a FET array, 22 MoS_2 lines with effective linewidth of ~ 1 μm are produced on a p^+-type Si substrate coated with 300 nm thick thermally grown SiO_2 using RISS. These MoS_2 lines have a large inter-line spacing of ~200 μm to provide footprint areas for Ti/Au contacts. Using our current mask set, 11 FETs with channel length of 5 μm are fabricated on a single MoS_2 line. Therefore, an as-fabricated FET array consists of totally 242 FETs. The p^+-type Si substrate serves as the common back gate for these FETs. Other details about the FET fabrication are described in the Methods and Materials Section. Figure 5.18 (a) shows the optical micrograph of three representative FETs fabricated on a 1 μm wide MoS_2 line. Figure 5.18 (b) plots the transfer characteristic curve (*i.e.,* drain-source current (I_{ds}) versus gate voltage (V_g) curve) measured from a representative back-gated MoS_2 FET. This FET exhibits a typical n-type

transport behavior and its on-off ratio is ~ 10^5. The FETs shown in Figure 5.18 (b) exhibit relatively low mobility and ON current values, which are attributed to the relatively narrow MoS_2 channel width (~ 1 μm). Figure 5.19 (a) shows the optical micrograph of a set of FETs made from a 15 μm wide RISS-produced MoS_2 line (for all FETs, the channel length is still 5 μm), and Figure 5.19 (b) displays the transfer characteristic curve of a representative FET. The ON current of such a relatively wider FET measured under a given condition is about two orders of magnitude higher than that of a 1 μm wide FET.

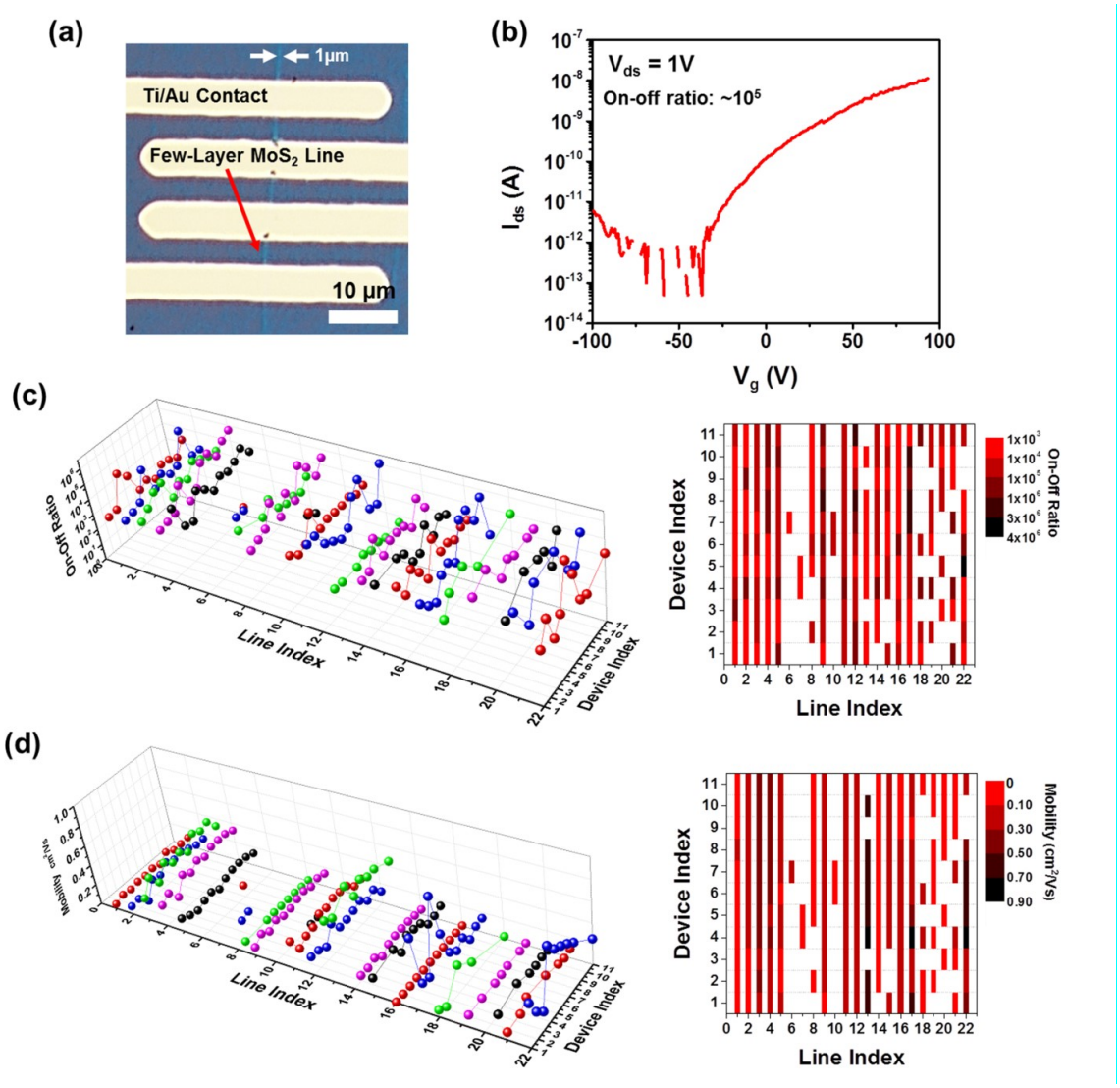

Figure 5.18 Demonstration of an array of working FETs fabricated on RISS-produced few-layer MoS_2 lines: (a) optical micrograph of three representative back-gated MoS_2 FETs fabricated on a MoS_2 line (FET channel length: 5 μm, width: ~1 μm); (b) transfer characteristic (or I_{ds}-V_g) curve of a representative MoS_2 FET; (c) 3D (left) and 2D top-view (right) plots of the on-off ratio data measured from 184 working FETs on the same substrate as the function of line

and device indexes; (d) 3D (left) and 2D top-view (right) plots of the field-effect mobility data measured from 184 working FETs as the function of line and device indexes.

The mobility values of such wider FETs are extracted to be higher than 1 cm^2/Vs, and they are comparable with the mobility values of recently reported FETs made from CVD-grown MoS_2 films [206-208]. In the future, the mobility and ON current values of RISS-produced MoS_2 FETs are anticipated to be further improved through optimization of CVD conditions. Totally, 184 out of 242 as-fabricated FETs are properly working devices, and the fabrication yield is ~ 76 %. This yield could be further improved through optimization of RISS and device fabrication processes. Figure 5.18 (c) displays the on/off ratio data measured from these 184 FETs, which are plotted as the function of their line and device indexes. In Figure 5.18 (c), the left inset is the 3D plot, and the right inset is the 2D top-view plot that provides a clear view for the location distribution of working FETs in the array. On-off ratios measured from these FETs are in the range of 10^3 to ~ 3 × 10^6, which are reasonably high for most switching device applications. Figure 5.18 (d) shows the 3D (left) and 2D (right) plots of the field-effect mobility data extracted from the transfer characteristics of the FETs. Specifically, the field-effect mobility of a FET is extracted by using Eqn. 2, where ε_0 is the vacuum permittivity, $\varepsilon_r \approx 3.9$ is the relative permittivity of the SiO_2 dielectric layer, C_{ox} is the gate capacitance, and W/L is the width/length ratio of the MoS_2 FET channel.

$$\mu = \frac{1}{C_{ox}\frac{W}{L}V_{ds}}\left(\frac{dI_{ds}}{dV_g}\right) \qquad C_{ox} = \frac{\varepsilon_0\varepsilon_r}{d} \qquad (2)$$

Figure 5.18 (d) shows that the mobility values of the FETs range from 0.1 to 1 $cm^2/(Vs)$ (mean value: 0.18 ± 0.17 cm^2/Vs). Such relatively low mobility values are attributed to the relatively small average grain size within the MoS_2 channel lines [196, 200]. During a site-selective growth process, the nucleation sites are highly localized and concentrated within the target growth areas. This results in very limited free space for a MoS_2 grain to grow before the local MoS_2 cover ratio reaches to 100 % [196, 200].

Future research effort will seek to identify the CVD mechanisms capable of addressing this generic challenge for site-selective growth of layered materials. Here, it is also noted that as shown in Figure 5.18 (c) and (d), the on/off ratio and mobility data measured from the FETs on the same MoS_2 line (*i.e.,* the FETs with the same line index) exhibit a relatively smaller variance in comparison with those measured from the FETs on the different MoS_2 lines. Such a relatively large variance in the FET performance among lines is attributed to the variances in morphological parameters among RISS-produced MoS_2 lines, which could be further reduced by optimizing the large-area distribution of rubbing stress during the RISS processes.

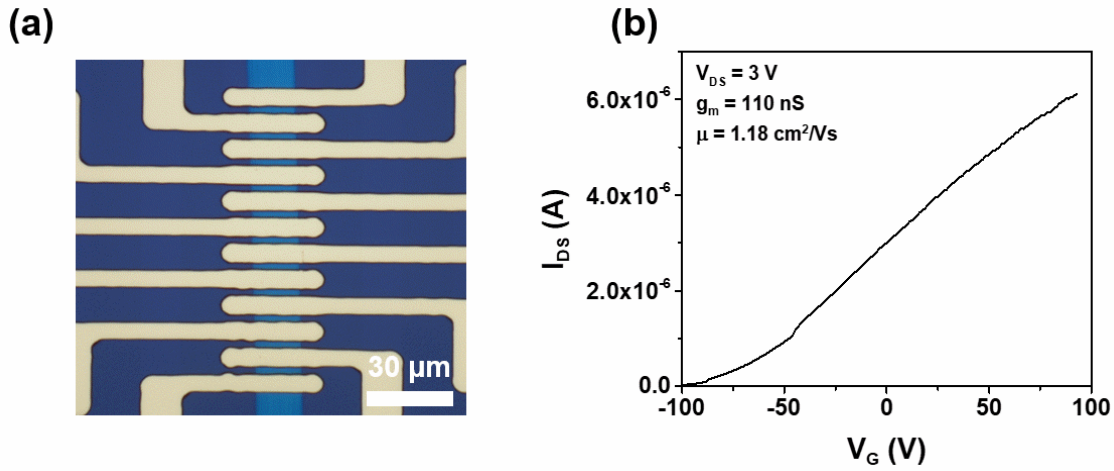

Figure 5.19 (a) Optical micrograph of a set of FETs made from a 15 μm wide RISS-produced MoS_2 (For all FETs, the channel length is 5 μm); (b) transfer characteristic curve of a representative 15 μm wide FET.

5.3.5 Demonstration of an Array of Memristors on RISS-Produced MoS_2 Lines

Although the relatively small crystalline MoS_2 grains in RISS-produced MoS_2 lines result in relatively low field-effect mobility and are not very suitable for high-speed FET applications, they can form a 2D channel rich in movable defects (*e.g.,* sulfur vacancies, molybdenum vacancies, antisites, and impurities) and potentially enable a niche application of RISS-produced MoS_2 structures in memristive electronics [209]. The areal density of sulfur vacancies in a MoS_2 layer is ~ 10^{13} cm^{-2}, which is about two orders of magnitude higher than that of other movable defects [210]. Therefore, sulfur vacancies

are expected to be the dominant movable defects responsible for the observed memristive behavior. Although in a polycrystalline MoS_2 channel the long-distance migration of movable defects could be blocked by grain boundaries, the local migration of such defects around MoS_2/metal interfaces is still expected to result in an effective modulation of the Schottky barriers at MoS_2/metal interfaces and induces memristive switching processes [211]. To preliminarily demonstrate such a potential application, we fabricated and characterized memristor arrays based on RISS-produced MoS_2 lines, which have the same device structure as the FET array shown in Figure 5.18.

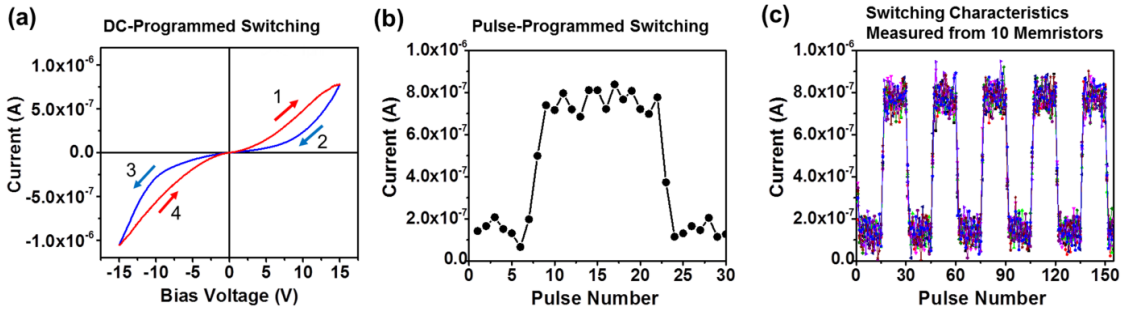

Figure 5.20 Demonstration of working memristors fabricated on RISS-produced few-layer MoS_2 lines: (a) DC-programmed switching characteristic curve (or hysteretic I-V curve) measured from a representative MoS_2 memristor; (b) pulse-programmed switching characteristic curve measured from the same memristor (set process: 10 -30V, 5µs pulse; reset process: 10 +30V, 5µs pulses); and (c) pulse-programmed switching characteristic curves measured from 10 different memristors, which are plotted together to demonstrate a high device-to-device consistency in their switching characteristics.

Figure 5.20 shows the switching characteristics measured from such memristors. Specifically, Figure 5.20 (a) shows the DC-programmed switching characteristic curve (*i.e.,* hysteretic I-V curve) measured from a representative MoS_2 memristor, which exhibits a prominent memristive switching behavior. Additionally, such MoS_2 memristors exhibit a low threshold field magnitude for initiating memristive switching (~ 10^4 V/cm), which is about two orders of magnitude lower than that of the conventional memristors based on transition metal oxides [209, 212]. Figure 5.20 (b) plots the pulse-programmed switching characteristic curve (*i.e.,* current under a fixed voltage of 1 V *versus* number of applied pulses) measured from the same memristor (set process: 10 -30

V, 5 μs pulse; reset process: 10 +30 V, 5 μs pulses). During such a pulse-programmed switching cycle, the memristor current (measured under 1 V bias) gradually varies from ~ 100 nA to ~ 800 nA, indicating a switching ratio of ~8. Such prominent memristive switching characteristics observed in our MoS_2 memristors are attributed to the high concentration of movable defects in RISS-produced MoS_2 channel lines that can dynamically modify the Schottky barriers at the MoS_2/contact interfaces and therefore modulate the conductance states of the memristors [211]. Figure 5.20 (c) plots the pulse-programmed switching characteristic curves measured from ten memristors in the same array. These curves are also individually plotted in Figure 5.21. These ten MoS_2 memristors exhibit a high device-to-device consistency in their memristive switching characteristics (the relative standard deviation in their set/reset currents is ~3%) and could be further exploited for constructing neural network devices for neuromorphic computing applications. This result also indicates that RISS-produced MoS_2 channel lines exhibit a high uniformity in their concentrations of movable vacancies.

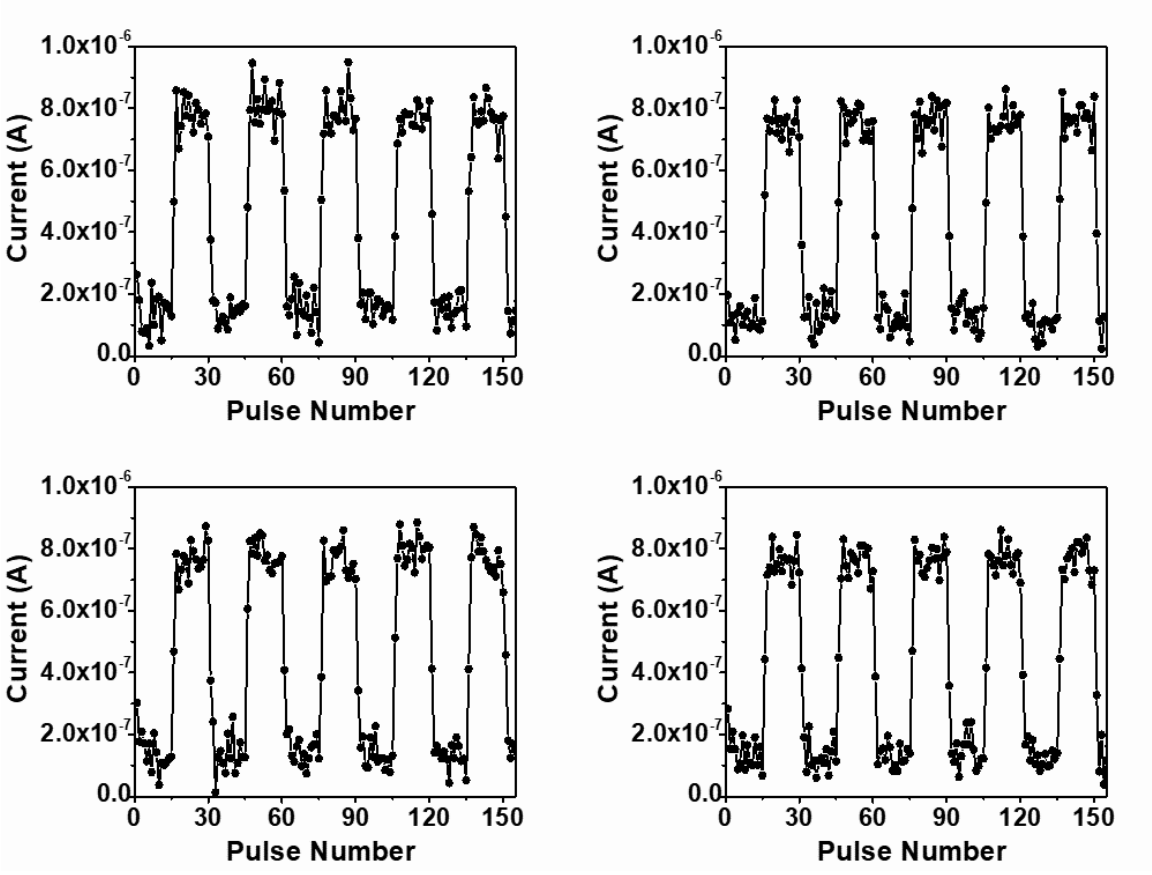

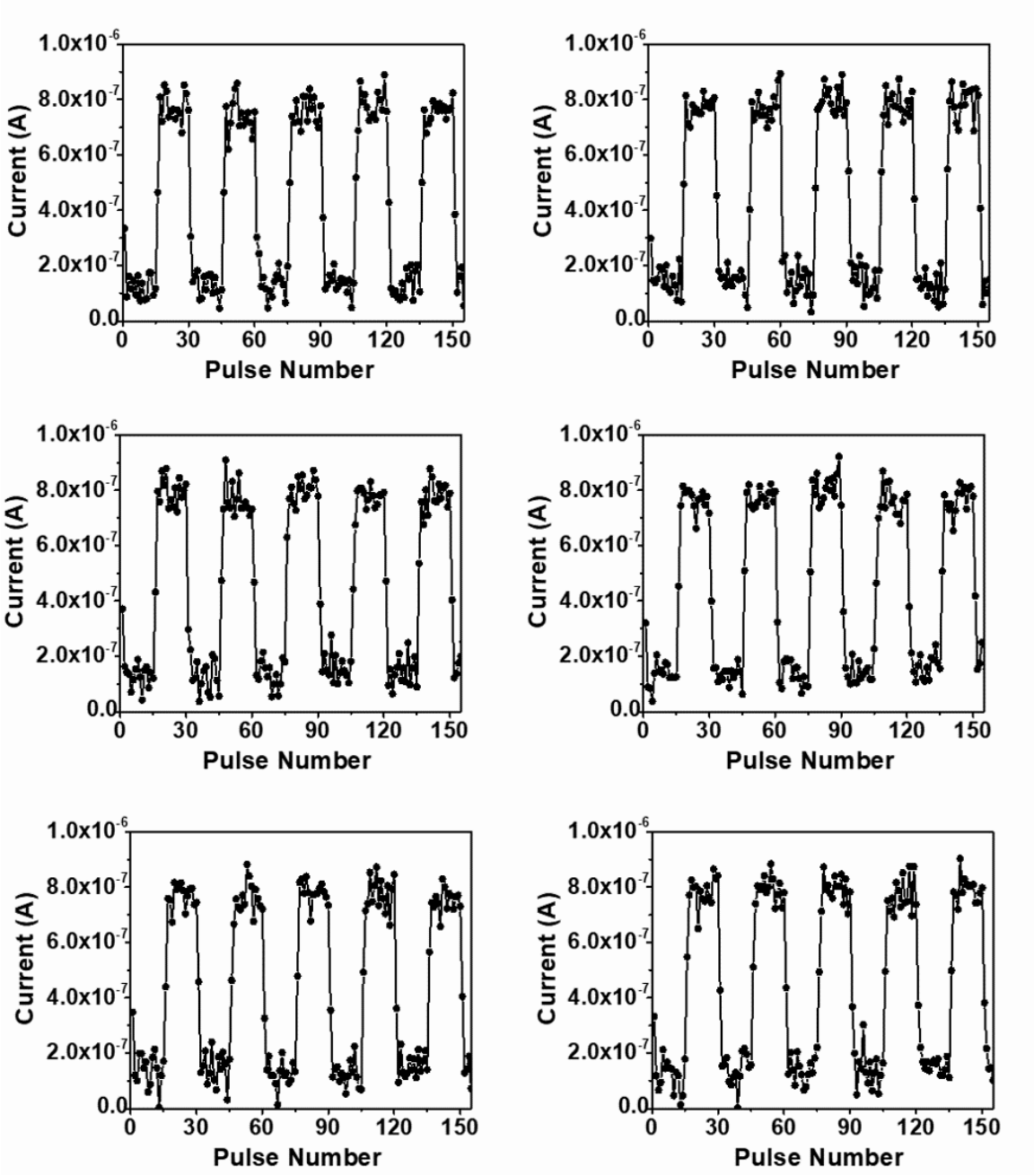

Figure 5.21 Pulse-programmed switching characteristic curves (set process: 10 -30V, 5μs pulse; reset process: 10 +30V, 5μs pulses) measured from 10 different memristors made from RISS-produced MoS_2 lines. The switching ratio is measured to be ~ 8.

5.4 Summary

We developed and systematically studied a rubbing-induced site-selective growth (RISS) method, which can enable scalable fabrication of few-layer MoS_2 device patterns without need of additional patterning processes. In a RISS process, triboelectric charge patterns are generated on a target dielectric substrate surface by a template-based rubbing process and serves as highly preferential nucleation sites for CVD growth of MoS_2 structures. Using RISS, we have specifically demonstrated the fabrication of MoS_2 line/spacing patterns with various periods and linewidths. Our microscopy characterization in combination with FEA simulation implied that the morphologies of RISS-produced MoS_2 patterns are strongly correlated with the field magnitude distribution within rubbing-generated triboelectric charge patterns. Finally, RISS-produced MoS_2 lines were used for making arrays of FETs and memristors, in which the yield of working devices was evaluated to be ~76 %, and both types of the devices exhibited a good device-to-device consistency. Specifically, the MoS_2 FETs showed reasonably high on/off ratios in the range of 10^3 to 3×10^6 and exhibited an average field-effect mobility of 0.18 ± 0.17 $cm^2/(Vs)$. For the MoS_2 memristors, a large switching ratio of ~ 8 and a low threshold field magnitude (~10^4 V/cm) for initiating memristive switching are demonstrated. The presented RISS method could be further developed into a cost-efficient scalable nanomanufacturing technique capable of producing commercially-viable device patterns based on various layered materials.

Chapter 6

Inkjet-Defined Site-Selective (IDSS) Synthesis of MoS_2 Features with Rich Out-of-Plane Edges for Lithium Storage Applications

6.1 Introduction

Recently, the demands for miniaturized lithium batteries that could be integrated with functional devices at the chip level have been increasing at a rapid rate in step with technological advances in miniaturized electronic devices and systems, such as wearable bioelectronic units, pacemakers, smartphones, electric micro-drones and micro-robots [213-216]. In accordance with these circumstances, Molybdenum disulfide (MoS_2) has been in the spotlight due to its fascinating electrical and electrochemical properties, high abundance, and two-dimensionally (2D) layered structure, which could enable lithium-ion uptake [217-218]. Especially, lithium storage capacity of MoS_2 is 670 mAh/g, which is about twice of magnitude higher than those of currently commercialized carbonaceous anode materials (*e.g.,* graphite: 372 mAh/g) [219-220]. However, in spite of the growing interest in MoS_2 as a promising anode material for making microscale lithium-ion batteries (LIBs), the current research society still lacks appropriate scalable microfabrication approaches capable of producing MoS_2-based microscale anode structures for building microscale lithium batteries on a chip. Such a fabrication-oriented challenge indeed breaks down into two more specific technical demands. First, such

desired microfabrication approaches need to be able to lithographically generate orderly arranged microscale MoS_2 anode structures, but they should not involve any resist-based lithography or plasma-based etching processes. This is because of the fact that these processes bring about a wide range of contaminants that complicatedly change or degrade electrical and electrochemical properties of MoS_2 structures. Such contaminants are much more detrimental to the properties of MoS_2 than to those of bulk materials because of the atomically layered structures of MoS_2 and other relevant 2D materials [52, 188-191]. More seriously, state-of-the-art wafer cleaning techniques (*e.g.,* piranha and RCA methods) cannot clean up these process-introduced contaminants without accompanying serious chemical or physical damages to MoS_2 structures. Such a difficulty in sample cleaning is due to the fact that atomically layered MoS_2 structures, which are formed by van de Waals force, are vulnerable in such cleaning solutions, and also due to the fact that MoS_2 and other van de Waals solids with relatively inertial surfaces have a relatively weak bonding strength to the hosting wafer and are easily delaminated by the cavitation in a cleaning route [192-193]. Second, the demanded microfabrication method should be able to produce microscale MoS_2 anode structures rich of out-of-plane edges. Recent works have shown that MoS_2 anodes with abundant out-of-plane edges exhibits the much higher charge-discharge rate and cycling reversibility in comparison with in-plane MoS_2 microstructures because out-of-plane MoS_2 structures allow more accessible pathways for lithiation processes [221-223]. Currently, hydrothermal synthesis is one of the widely used methods for producing out-of-plane MoS_2 structures, but it can hardly guarantee controllable structures of MoS_2 due to its complicate chemical reactions with lots of process variables such as molar ratios of chemicals, starting materials, hydrothermal temperature and time [224-226]. In addition, hydrothermal synthesis has a poor compatibility with planar lithography techniques that are required for making microscale battery structures on a chip. Chemical vapor deposition (CVD) can generate uniform MoS_2 films over large areas, which are compatible with planar lithography processes, but special growth schemes need to be incorporated into CVD processes to result in a high abundance of out-of-plane MoS_2 edges [189, 193, 227]. In addition, as mentioned above, CVD-grown MoS_2 films need to be subsequently patterned into microscale battery anode features by the lithography processes without involving strong chemical or plasma

treatments. Therefore, it is highly desirable to develop a scalable fabrication technique without involving resist and plasma, capable of producing orderly arranged MoS_2 microstructures rich of out-of-plane edges.

In this chapter, we develop an inkjet-defined site-selective growth (IDSS) method, which takes advantage of inkjet printing and CVD processes, capable of growing both in-plane and out-of-plane MoS_2 structures in a controllable fashion at deterministic locations on a chip substrate. An IDSS process mainly includes two steps: (i) inkjet dispensing of solution droplets (*e.g.,* deionized water (DI) or graphene ink) followed with drying of the droplets to predefine the target locations on a substrate for growing MoS_2 features, and (ii) site-selective CVD growth of in-plane or out-of-plane MoS_2 structures at the substrate locations, where droplets are inkjet-dispensed. Such a selective growth scheme in IDSS is attributed to the fact that dried solution droplets leave behind little amount of residues (*e.g.,* impurities or graphene flakes), which could lead to local topography change within droplet-covered regions and serve as effective nucleation seeds during the CVD process [194, 205]. More importantly, in addition to enable site-selective growth, IDSS is also able to produce MoS_2 microstructures with different crystal morphologies in a controllable fashion. Specifically, if using DI water droplets to define growth locations, the IDSS process dominantly produces in-plane MoS_2 features. We have demonstrated fabrication of an array of the working transistors based on such in-plane MoS_2 features, which exhibit a good uniformity in their transfer characteristics. If using graphene ink droplets to define growth locations, the process dominantly produces out-of-plane MoS_2 features selectively nucleated on top of inkjet-deposited graphene flakes. Such a hierarchical structure of out-of-plane MoS_2/graphene is rich of exposed edges and could serve as an efficient lithium-ion battery anode structure, which could provide high storage density of lithium ions, high charge/discharge rates, as well as small footprint size on a chip. Using IDSS-produced out-of-plane structures, we have demonstrated the fabrication of miniaturized lithium-ion batteries, with a footprint size of ~1mm and good discharge/charge capacity parameters (206 $\mu Ah/cm^2$ / 113 $\mu Ah/cm^2$ at 55 $\mu A/cm^2$ current density).

6.2 Experimental Setup for IDSS Process and Its Applicational Devices

6.2.1 Design of the Inkjet-Defined Site-Selective (IDSS) Synthesis Process

Figure 6.1 illustrates the inkjet-defined site-selective growth (IDSS) method for growing an array of in-plane and out-of-plane MoS_2 features on a target substrate. Following the sequence of processing steps, Figure 6.1 (a) schematically shows the inkjet printing step for dispensing an array of solution droplets (*e.g.,* DI water or Graphene ink) on the target substrate. The dispensed droplets predefine the locations, where MoS_2 features are to be nucleated in the subsequent steps. Generally, inkjet printing can dispense a broad variety of liquid solutions into various array patterns through programming of the dispensing courses. The inkjet printer used for this work can dispense a minimum droplet volume of ~10 pL, which typically deposits droplets on a SiO_2/Si substrate with an average footprint diameter of about tens of micrometers [228]. This inkjet printer can also print out droplet arrays with droplet-to-droplet spacings ranging from tens to hundreds of micrometers. In this work, DI water and graphene ink are used to induce site-selective growth of in-plane and out-of-plane MoS_2, respectively. As illustrated in Figure 6.1 (b), as-deposited droplets of DI water or graphene ink (solvent part) evaporate quickly on the target substrate. During the drying process, DI water and graphene ink droplets leave behind DI water residues and Graphene flakes on the substrate, respectively, which can serve as effective nucleation seeds for the subsequent CVD process [205, 229]. Figure 6.1 (c) illustrates the site-selective CVD of MoS_2 features on the substrate, and Figure 6.1 (d) illustrates as-grown MoS_2 features with two different types of crystal morphologies. Specifically, in-plane MoS_2 features, whose crystal grains dominantly grow along the substrate surface, are synthesized at the spots covered by DI water droplets. More interestingly, as to be shown in our following experimental results, out-of-plane MoS_2 features, whose crystal grains are not on the horizontal substrate surface, are selectively synthesized on top of the graphene flakes deposited through inkjet printing.

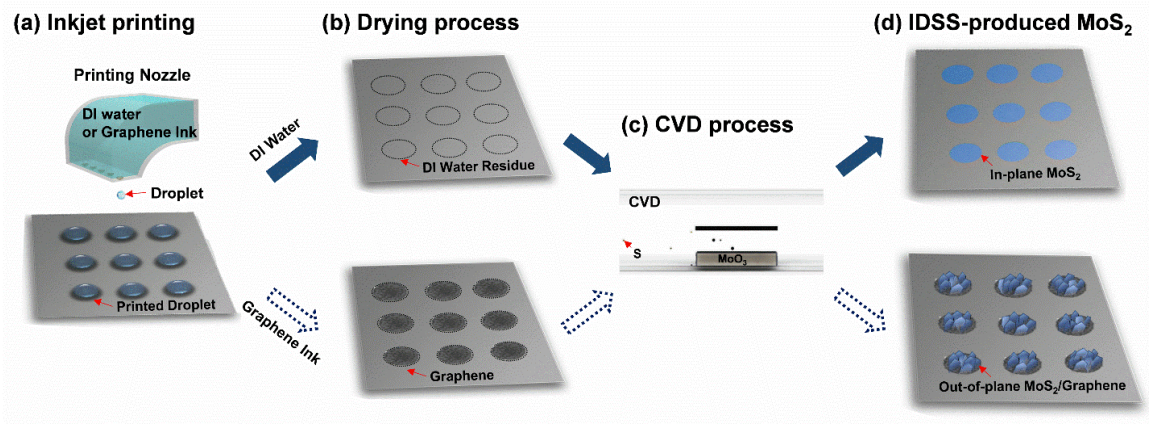

Figure 6.1 Setup of the IDSS process: (a) schematic illustration of inkjet printing step for dispensing an array of DI water or Graphene ink solution droplets on the dielectric substrate; (b) drying the droplet patterns before loading the sample into CVD quartz tube; (c) site-selective CVD growth of MoS_2 patterns; (d) IDSS-produced MoS_2 features with two different types of crystal morphologies.

6.2.2 Fabrication of FETs and On-Chip Batteries on IDSS-Produced MoS_2

The back-gate FETs are fabricated on IDSS-produced in-plane MoS_2 pixels. Two metal contacts with thickness of 5 nm Ti/50 nm Au are photolithographically patterned and deposited. Characteristic curves of FETs are measured using a Keithley 4200 semiconductor parameter analyzer.

To fabricate the on-chip battery with IDSS-produced out-of-plane MoS_2/Graphene pixels, C-shaped metallic pads (100nm Ti) are deposited through the aligned polyimide shadow mask. Afterwards, the polypropylene reservoir is attached with UV curable glue such that it can contain the liquid electrolyte and limit the electrochemical reaction of the cell to the pixel. Cells are prepared in the Ar-filled glove box, where the oxygen and H_2O levels are controlled below 0.5ppm. MoS_2/Graphene pixel and Li wire are used as the cathode and counter electrode respectively, and 1M $LiPF_6$ in a (1:1 volume ratio) mixture of ethylene carbonate (EC)/ ethyl methyl carbonate (EMC) is used as electrolyte. The electrochemical property of on-chip battery is measured using potentiostat (Biologic, SP-200) and the lab-made probe setup. Charge/discharge of the cell is tested in the 0.05-3V voltage window at 55μA/cm^2 current

density for 3 cycles each. Cyclic voltammogram (CV) measurement is performed at a scan rate of 0.5 mV/s in the same voltage range. Impedance plot is obtained in the frequency of 0.5 Hz - 1 MHz by applying 5 mV amplitude AC voltage, and EC-lab software is used to fit the impedance spectra to the equivalent circuit model.

6.3 Experimental Results of IDSS Method

6.3.1 Fabrication and Characterization of In-Plane MoS_2 Arrays Using IDSS

Figure 6.2 shows the optical micrographs (OMs) of several representative arrays of in-plane MoS_2 pixel features produced by IDSS processes. In this process, DI water was used as the dispensed material for inducing site-selective growth of in-plane MoS_2. Figure 6.2 (a), (b), (c) and (d) display as-grown MoS_2 feature arrays with various periods (or pixel-to-pixel spacings) of 200, 350, 500 and 650 μm, respectively. Such well-defined MoS_2 feature patterns are generated with no need of any extra resist-based lithography or chemical/plasma-based etching processes. Furthermore, Figure 6.2 (e) shows an IDSS-produced MoS_2 pixel pattern, which forms an alphabetical character 'M'. This shows that IDSS can generate arbitrary array patterns of MoS_2 pixels. Figure 6.2 (f) displays the zoomed OM of a representative MoS_2 pixel in the pattern array, which has an average diameter of ~ 90 μm. Such a MoS_2 pixel exhibits a smooth and round boundary, which is faithfully consistent with the area profile of the inkjet-deposited droplet, and there are no MoS_2 domains observed around the pixel. This indicates that the dispensed DI droplets can induce a high selectivity for MoS_2 growth on the substrate.

To further evaluate the growth selectivity of IDSS processes, we further performed Raman and atomic force microscopy (AFM) characterizations for IDSS-produced in-plane MoS_2 pixel features. Figure 6.3 (a) shows the Raman spectrum analyzed from the central spot of a representative MoS_2 pixel. This spectrum clearly exhibits two characteristic peaks of MoS_2, which are E^1_{2g} and A_{1g} observed at ~ 383 and ~ 407 cm^{-1}, respectively. Figure 6.3 (b) plots 16 Raman spectra captured from the 16 MoS_2 pixels in an array. All of these Raman spectrum curves exhibit very similar line

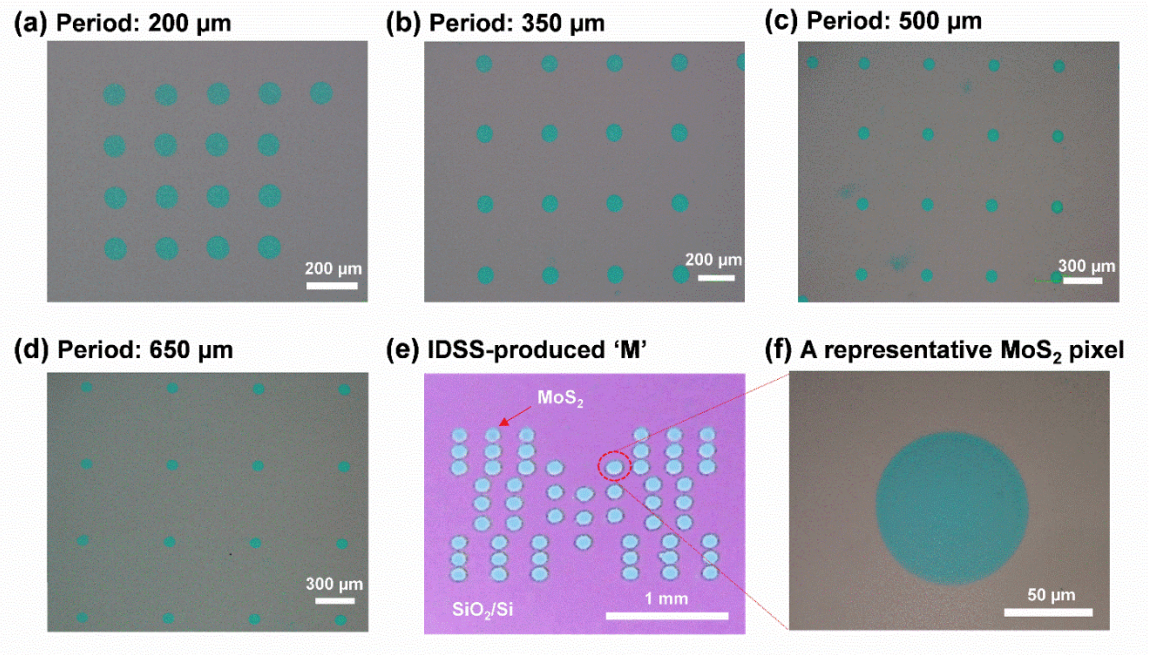

Figure 6.2 Optical micrographs of IDSS-produced in-plane MoS_2 pixel features with various periods of (a) 200 µm, (b) 350 µm, (c) 500 µm, and (d) 650 µm; (e) optical micrograph of an IDSS-produced MoS_2 pixel pattern forming an alphabetical character 'M'; (f) Zoomed optical micrograph of a representative MoS_2 pixel in the array, exhibiting the pixel diameter of ~ 90 µm.

shapes, and their E^1_{2g} and A_{1g} characteristic peaks are observed at almost the same positions. This implies a good uniformity of IDSS-produced MoS_2 pixel features. Here, the specific peak spacing between E^1_{2g} and A_{1g} peaks is measured to be ~ 24 cm^{-1}, which typically indicates the formation of few-layer MoS_2 with a thickness corresponding to 4 ~ 5 layers [201-202, 227]. Figure 6.3 (c) further shows the spatial mappings of the E^1_{2g} and A_{1g} characteristic peaks measured over a representative MoS_2 pixel, which are labelled with red and green colors, respectively. As shown in Figure 6.3 (c), both E^1_{2g} and A_{1g} Raman features only appear within the pixel area previously covered with the liquid droplet, and there is no any detectable E^1_{2g} or A_{1g} feature outside the pixel region. Such a high spatial contrast of Raman feature distribution further verifies the high growth selectivity of IDSS. To precisely quantify the thickness of IDSS-produced in-plane MoS_2 pixels, a substrate bearing MoS_2 pixels was mechanically agitated in a sonication bath to intentionally induce partial delamination for some MoS_2 pixel layers, as shown in Figure

6.3 (d). Figure 6.3 (e) shows the AFM topography image captured over the broken edge of a representative in-plane MoS_2 pixel, which is denoted with a dashed line (*i.e.*, Line 'a') in Figure 6.3 (d). Figure 6.3 (f) also plots the scanline along Line "a", which shows an average MoS_2 thickness of ~ 3.48 nm, which is consistent with the average thickness value (*i.e.*, 4 ~ 5 layers) estimated from Raman results.

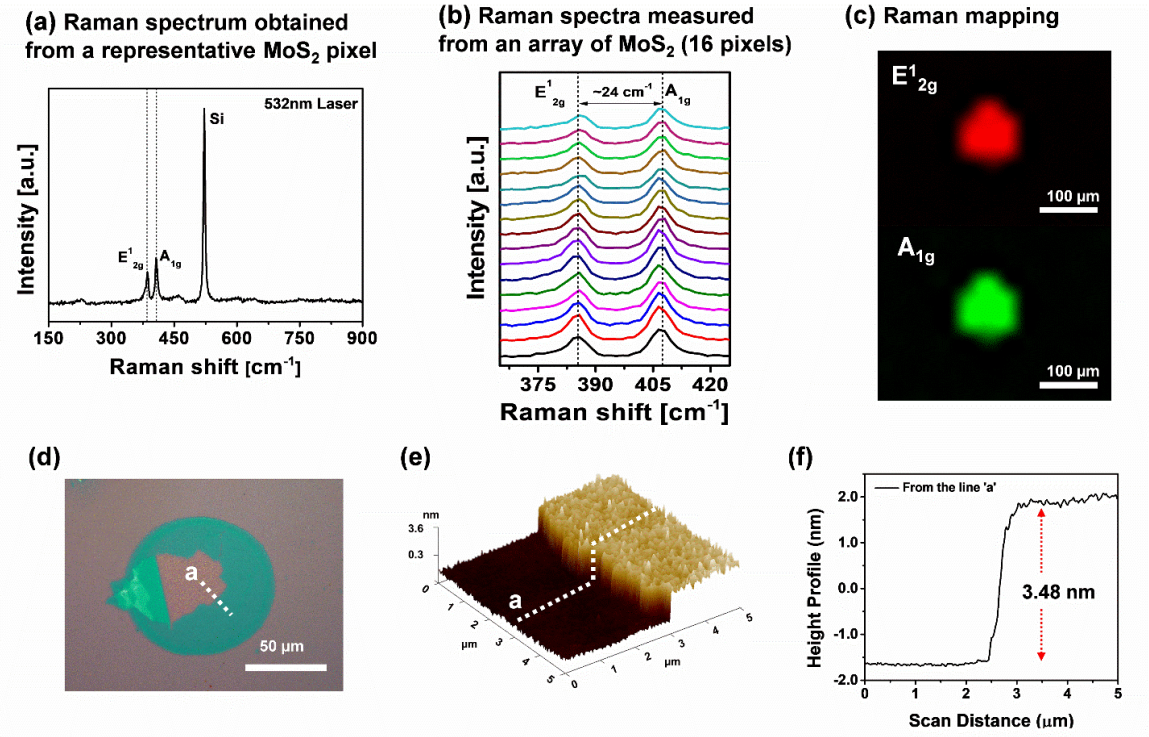

Figure 6.3 Characterizations of IDSS-produced in-plane MoS_2 pixel features: (a) Raman spectrum measured from the central region of a representative MoS_2 pixel; (b) 16 Raman spectra with their E^1_{2g} and A_{1g} characteristic peaks, obtained from the 16 MoS_2 pixels in an array; (c) Spatial Raman mappings of the E^1_{2g} and A_{1g} characteristic peaks measured over a representative MoS_2 pixel. (d) optical micrograph of a representative in-plane MoS_2 pixel with induced partial delamination for AFM measurement; (e) AFM topography image captured over a broken edge of a representative in-plane MoS_2 pixel; (f) AFM scanline along Line "a" of a few-layer MoS_2 pixel.

6.3.2 Demonstration of FETs Fabricated on the IDSS-Produced MoS_2 Array

To evaluate the electronic properties of IDSS-produced in-plane MoS_2 features, an array of field effect transistors (FETs) based on such MoS_2 pixel features were fabricated and characterized. Figure 6.4 (a) shows the optical microscopy (OM) image of an array of FETs made on a set of IDSS-produced in-plane MoS_2 pixels. For each FET, the channel length and average channel width are 2 and 50 μm, respectively. Figure 6.4 (b) displays the transfer characteristic curve acquired by measuring a representative MoS_2 FET, which is plotted in linear (Black) and semi-logarithmic (Red) scales. A typical n-type transport behavior is shown from the FET. Under the given measurement condition (V_{ds} = 3 V, V_g = -40 to 40 V), the FET exhibits on-off switching ratio larger than 10^4 and field-effect mobility of ~0.15 $cm^2/(Vs)$, respectively. The transfer characteristic curves measured from representative 3 MoS_2 FETs in the same array are plotted in Figure 6.5. The field-effect mobility values measured from these FETs are comparable to those of recently reported FETs fabricated by using the as-grown MoS_2 flakes grown by CVD and other site-selective approaches [196, 200, 227].

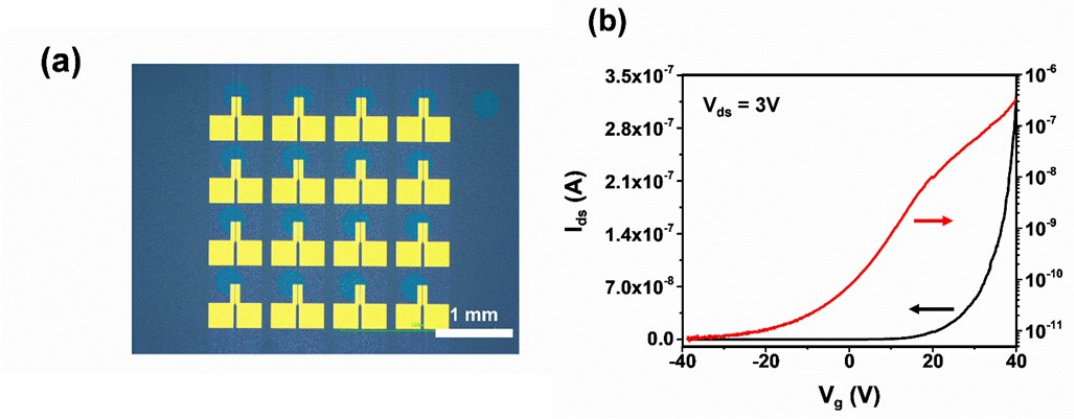

Figure 6.4 Measurement of electronic properties of IDSS-produced in-plane MoS_2 features: (a) optical micrograph of an array of FETs fabricated on a set of IDSS-produced in-plane MoS_2 pixels (channel length: 2 μm, channel width: 50 μm, Source/Drain contacts: 50 nm-thick Au with a 5 nm-thick Ti adhesion layer); (b) a transfer characteristic curve obtained from a representative MoS_2 FET, which is plotted in linear (Black) and semi-logarithmic (Red) scales.

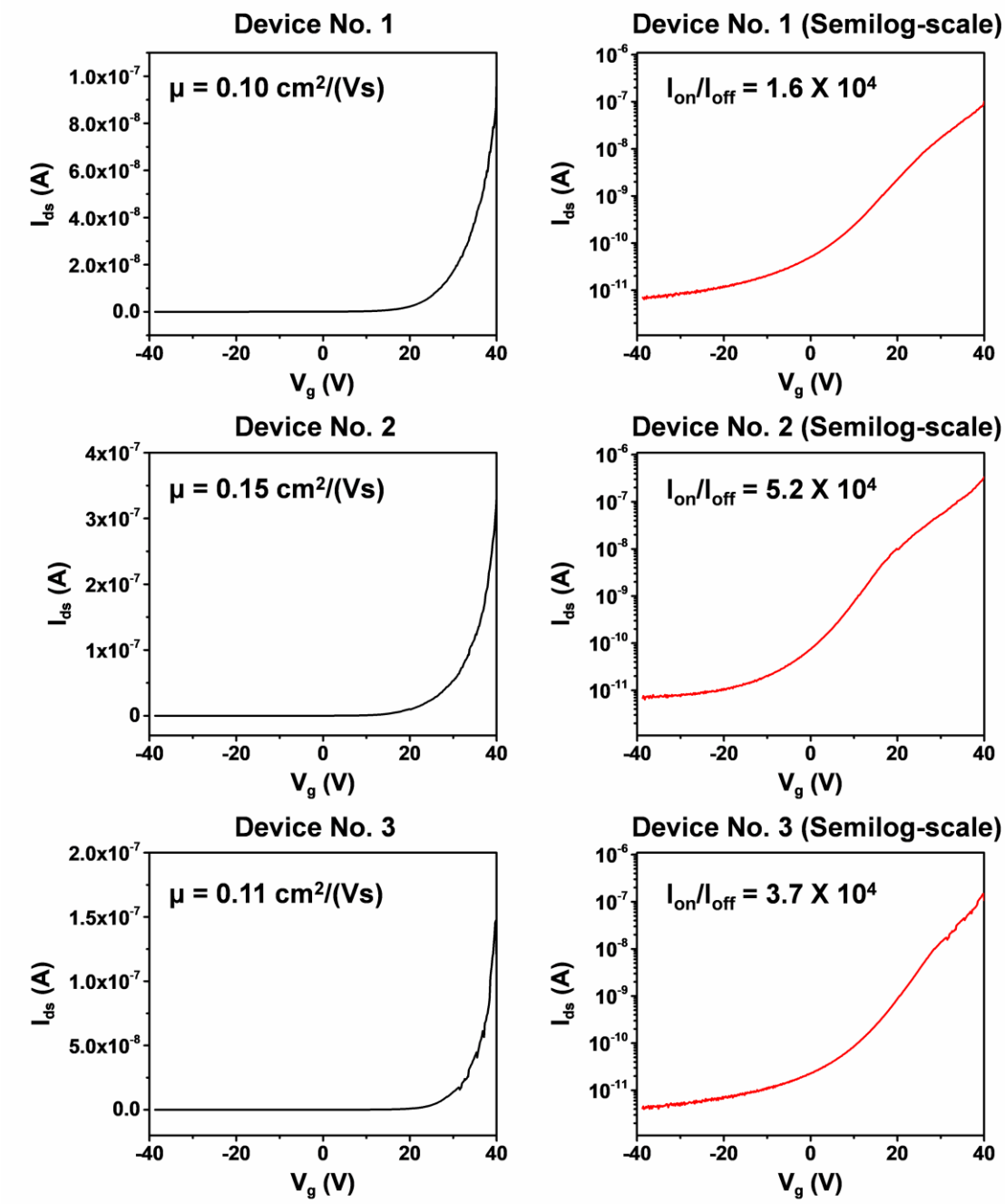

Figure 6.5 Transfer characteristic curves measured from representative 3 MoS_2 FETs made from IDSS-produced in-plane MoS_2 pixel arrays. (V_{ds} = 3 V, V_g = -40 to 40 V).

6.3.3 Fabrication and Characterization of IDSS-Produced Out-of-Plane MoS_2

To leverage IDSS-produced MoS_2 structures for electrochemical applications such as catalyst and lithium-ion battery (LIB), it is highly desirable to explore the applicability about using IDSS to generate MoS_2 structures rich of out-of-plane edges [230-231]. In this work, we specifically explore the IDSS processing conditions capable of generating MoS_2 pixel features rich of out-of-plane edges, which could be used as the anode structures for LIBs. After testing different inkjet-dispensed liquid droplets in IDSS processes, we found that droplets of graphene ink solution on a SiO_2/Si substrate can lead to a high yield of out-of-plane MoS_2 structures during CVD. Such out-of-plane MoS_2 structures are expected to provide much more accessible pathways for sustaining lithiation processes in comparison with in-plane MoS_2 structures [221, 223]. Specifically, Figure 6.6 (a) shows the optical micrographs of an array of as-dispensed graphene ink droplets (pixel diameter ~90 μm; pixel-to-pixel spacing ~200 μm). To demonstrate inkjet dispensing of graphene ink droplets with various sizes, a relatively large graphene ink droplet (pixel diameter ~ 1 mm) was dispensed and also shown in Figure 6.6 (a). After the subsequent CVD process, out-of-plane MoS_2 structures are selectively synthesized on top of the inkjet-dispensed graphene pixel features. Figure 6.6 (b) shows the scanning electron micrographs (SEMs) of a representative as-grown MoS_2/graphene pixel feature. The magnified SEM image in Figure 6.6 (b) clearly shows that such a pixel feature is dominantly composed of out-of-plane MoS_2 flakes, which are randomly arranged along various out-of-plane orientations. Figure 6.6 (c) shows the Raman spectrum measured from a representative out-of-plane MoS_2/graphene pixel. Two characteristic peaks (E^1_{2g} and A_{1g}) of MoS_2 are observed at ~ 381 and ~ 407 cm^{-1}, respectively. The Raman intensity ratio between in-plane Mo-S phonon mode (E^1_{2g}) and out-of-plane Mo-S phonon mode (A_{1g}) peaks is 1:3, which also strongly implies the abundance of out-of-plane MoS_2 flakes in the pixel [232]. Furthermore, characteristic Raman peaks (D, G, and 2D) of graphene are also observed at the larger Raman shifts. The D band at ~ 1353 cm^{-1} is attributed to disordered structures or defects associated with sp^2 carbon rings, which is typically observed in the graphene flakes deposited from graphene inks [233]. G and 2D bands, which are associated with vibrational mode of sp^2 hybridized carbon atoms,

appear around ~ 1581 and ~ 2711 cm^{-1}, respectively. The relatively low intensity ratio between 2D and G peaks (*i.e.*, I_{2D}/I_G = ~ 0.5) also indicates defect-rich graphene structures [234]. Such graphene structures provide a large number of out-of-plane edge states, which are expected to serve as effective seeding promoters for inducing site-selective nucleation of out-of-plane MoS_2 grains [229]. Figure 6.6 (d) and (e) show the energy-dispersive X-ray spectroscopy (EDS) mapping images for displaying the spatial distributions of Mo and S atoms around a MoS_2/graphene pixel. Such EDS results show that Mo/S signals are highly localized within the pixel feature area, and therefore IDSS can also result in a high site selectivity for growing out-of-plane MoS_2 structures.

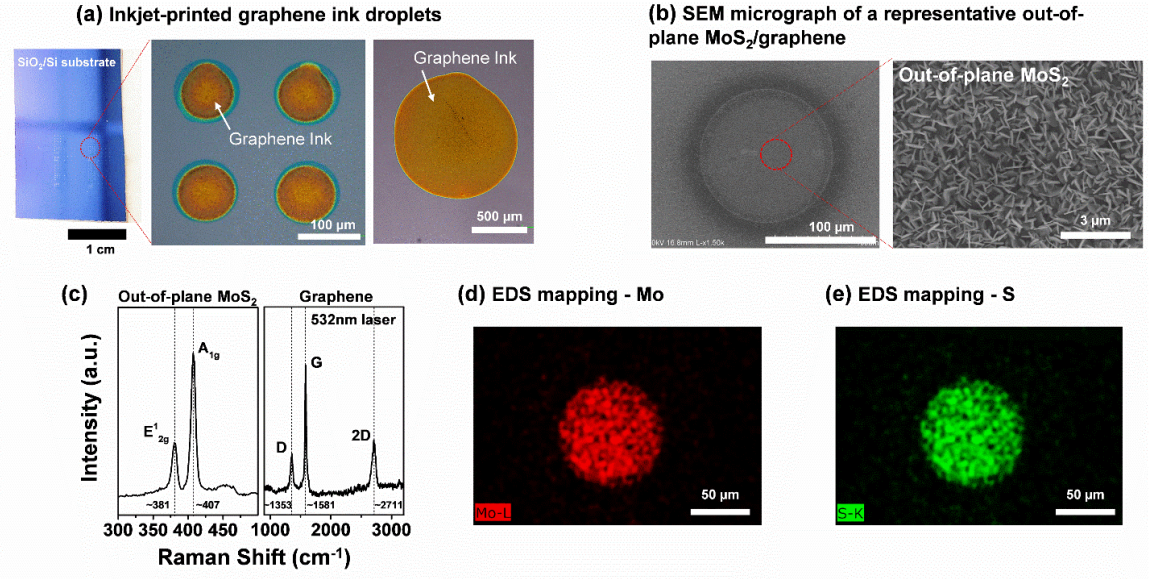

Figure 6.6 Characterizations of IDSS-produced out-of-plane MoS_2 pixel features: (a) optical micrographs of as-dispensed graphene ink droplets; (b) SEM images of a representative as-grown MoS_2/graphene pixel feature; (c) Raman spectrum from a representative out-of-plane MoS_2/graphene pixel, which exhibits characteristic peaks of both MoS_2 (E^1_{2g} and A_{1g}) and graphene (D, G, and 2D); (d) and (e) show the EDS mapping images of the spatial distribution of Mo and S atoms around a MoS_2/graphene pixel.

6.3.4 Demonstration of a Li-Ion Battery Using IDSS-Produced Out-of-Plane MoS_2/Graphene Heterostructure

To evaluate the electrochemical properties of IDSS-produced out-of-plane MoS_2/graphene structures, we performed a half-cell battery test. Figure 6.7 (a) schematically illustrates the test setup of a mini-size LIB, in which an out-of-plane MoS_2/graphene pixel serves as the electrode component. To make such a half-cell battery, graphene ink droplets with average footprint diameter of ~1 mm are dispensed on a SiO_2 substrate by inkjet printing, and then an IDSS process is conducted to produce out-of-plane MoS_2/graphene pixel features. Such pixel features also have an average footprint diameter of ~1 mm, which can result in charge-discharge characteristic current signals measurable for our current battery characterization tool. The smaller MoS_2/graphene pixel features could be used for making batteries if the characterization tools with improved measurement limits are implemented. However, our current ~1 mm size MoS_2/graphene pixel features are already small enough for on-chip battery applications. After the IDSS process, a mini-size well made of polypropylene (PP) is placed on top of the MoS_2/graphene pixel and filled with electrolyte (Lithium hexafluorophosphate, $LiPF_6$). The out-of-plane MoS_2 and graphene flakes in the pixel serve as the cathode and the current collector, respectively. In addition, 100 nm-thick Ti, which does not react with the electrolyte, is deposited as an external electrode. A Li metal wire is used as the counter electrode (anode), and half of the wire is immersed into the electrolyte. This Li wire is placed close to the MoS_2/graphene pixel, but there is a gap of ~30μm in between to prevent short circuit.

Figure 6.7 (b) shows the lithiation (discharge) and delithiation (charge) profiles of MoS_2/graphene electrode *vesus* Li/Li^+ measured in the PP reservoir. The test was carried out in the sweep voltage range of 0.05 – 3 V at a constant current density of 55 $\mu A/cm^2$. On the 1st discharge curve, the plateau appearing at 1.1 V is attributed to Li intercalation into MoS_2 layers and formation of Li_xMoS_2 ($0 \leq x \leq 4$). Another plateau at 0.6 V on the same curve is attributed to the conversion reaction, which is described by $MoS_2 + 2xLi^+ + 2xe^- \rightarrow Mo + xLi_2S$. The plateau in the voltage regime lower than 0.2 V is attributed to the lithiation of graphene, which could form LiC_x ($0 \leq x \leq 6$). In the 2nd

and 3rd discharge profiles, the plateau at 1.1 V disappears because of the irreversibility of conversion reaction. On the other hand, during three times charging processes, all profiles display one plateau at 2.3 V, which indicates delithiation of Li_2S and generation of S. Areal capacities of the first discharge and charge are evaluated to be 206 μAh/cm^2 and 113 μAh/cm^2, respectively. Considering the similar current density (50 μA/cm^2) set in the study by He *et al.*, areal discharge capacity obtained from our mini-size LIB is estimated to be comparable to that measured from R2032 type coin cells (~180 μAh/cm^2) [231]. During the first charge/discharge cycle, coulombic efficiency (CE) is initially low (~55 %), which could be ascribed to the electrolyte decomposition or irreversible reaction processes [231]. However, CE increases to 80 % and 84 % in the 2nd and 3rd cycles, respectively, and it is expected to further rise with increasing the number of cycles, as reported in the previous studies [231, 235-236]. This result suggests that IDSS-produced MoS_2/graphene pixel structures can be used for making miniaturized on-chip battery electrodes with good lithium storage properties.

To further analyze the electrochemical reaction properties of IDSS-produced MoS_2/graphene electrodes, cyclic voltammograms (CVs) of the half-cell battery were measured in the voltage range of 0.05 – 3 V at a constant scan rate of 0.5 mV/s and plotted in Figure 6.7 (c). The CV curve in the first cathodic sweep shows two peaks at 1.1 V and 0.6 V, which indicate the intercalation and conversion reactions, respectively. In the following cathodic scans, these two peaks at 1.1 V and 0.6 V disappear as a result of the irreversible conversion reaction, whereas a small peak emerges at ~ 1.8 V arising from the Li_2S formation [236-238]. In the anodic sweeps, the peak at 1.7 V is attributed to the removal of Li^+ ions pertaining to the Mo reduction [235, 239], and the peak at 2.3 V is associated with the oxidation of Li_2S to form S. Additionally, during the discharge/charge process, the peaks at ~ 0.2 V shows the lithiation/delithiation of graphene features [235, 240]. All potential peak locations are well consistent with the plateau voltages acquired in the charge/discharge characterizations.

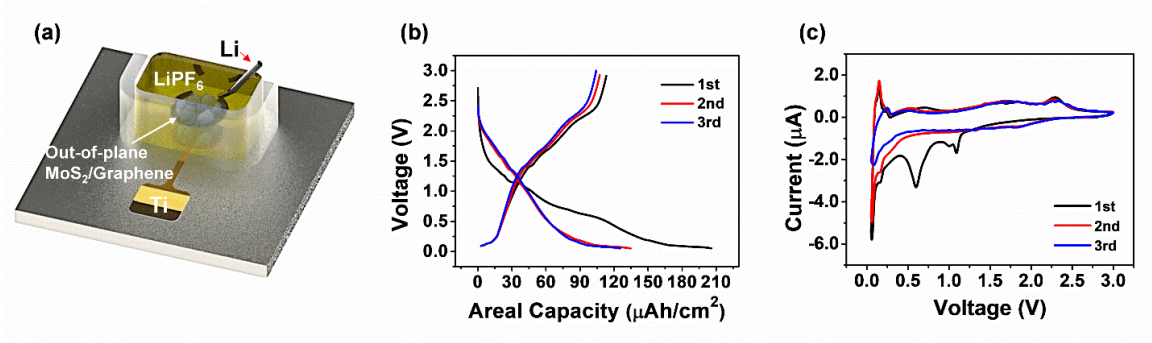

Figure 6.7 Measurement of electrochemical properties of IDSS-produced out-of-plane MoS_2/graphene pixel electrode: (a) schematic illustration of the half-cell Li-ion battery test setup; (b) discharge/charge profiles of MoS_2/graphene electrode measured in 0.05 – 3 V at 55 μA/cm^2 current density; (c) Cyclic voltammograms obtained from a MoS_2/graphene pixel electrode in the range of 0.05 – 3 V at the 0.5 mV/s scan rate.

6.4 Seek an Origin of Site-Selective Growth Capability of IDSS Method

Finally, to further reveal the scientific mechanism responsible for the site-selective growth capability of IDSS, additional comparison test results are presented in Figure 6.8. Figure 6.8 (a) shows the AFM topography image of a cleaned SiO_2/Si surface, which serves as a control substrate. The root mean squared surface roughness (R_q) of this control substrate is measured to be ~ 0.26 nm, which is normal for a cleaned SiO_2/Si substrate. After a CVD process, this cleaned substrate surface is covered by a continuous MoS_2 film, which does not show any spatial selectivity for MoS_2 nucelation, as shown in Figure 6.8 (b). Figure 6.8 (c) displays the AFM topography image of a dry SiO_2/Si substrate area ever covered by an inkjet-dispensed DI water droplet. The surface roughness (R_q) of this substrate area is measured to be ~ 4.73 nm that is about 20 times larger than that of the control substrate area. This indicates that even Type 1 ASTM DI water droplets still contain minuscule residues that are deposited on the substrate after the drying of droplets [241]. Such residues increase the local surface roughness and are expected to result in an enhanced affinity (or spatial selectivity) for MoS_2 nucleation during CVD [205]. Figure 6.8 (d) shows an in-plane MoS_2 pixel synthesized at the designated location by IDSS. Figure 6.8 (e) further shows the AFM topography image of

a substrate area ever covered by an inkjet-dispensed graphene ink droplet. The surface roughness (R_q) of this area is measured to be ~ 43.2 nm, which is ~166 times and ~9 times larger than those of the control and DI-water-deposited substrate areas, respectively. Such a large surface roughness is due to the graphene flakes left within the droplet-covered spot after drying of the graphene ink droplets. In combination with such enhanced surface roughness, the carbon contained in graphene flakes could significantly promote the reduction of MoO_3 precursors and therefore accelerate the sulfurization process, which is expected to result in the formation of out-of-plane MoS_2 features [229, 242]. Figure 6.8 (f) shows the SEM images of an IDSS-produced out-of-plane MoS_2 pixel feature on top of the inkjet-dispensed graphene flakes.

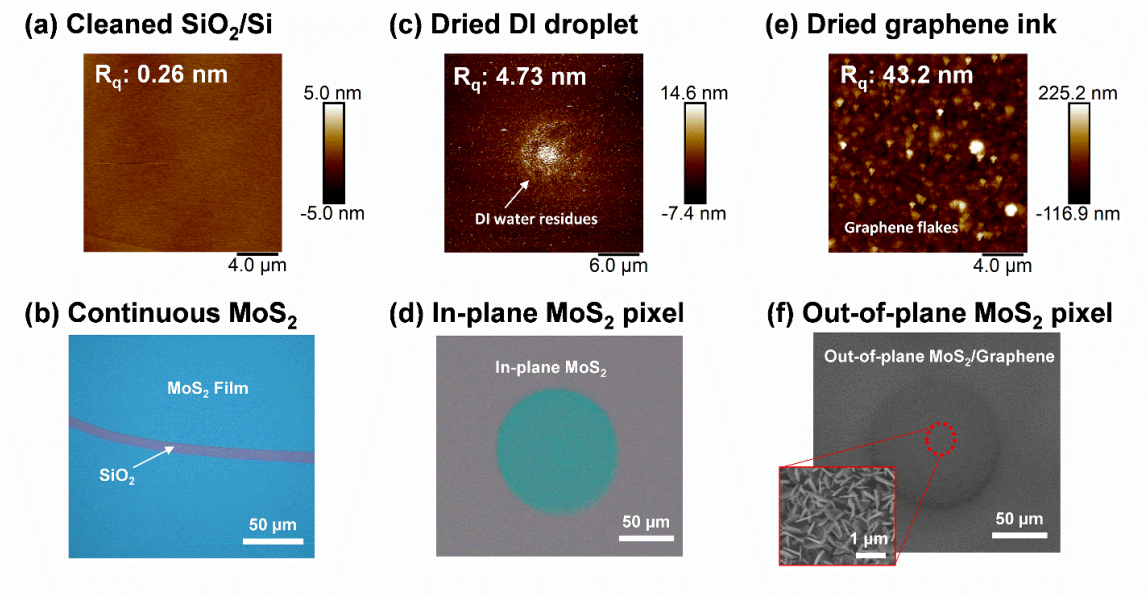

Figure 6.8 A comparison test performed with different IDSS printing materials: a control substrate without IDSS process; (a) AFM image of cleaned SiO_2/Si substrate; (b) optical micrograph of CVD-grown continuous MoS_2 film, DI water-based IDSS process; (c) AFM image of a dry SiO_2/Si substrate area ever covered by an inkjet-dispensed DI water droplet; (d) optical micrograph of IDSS-produced in-plane MoS_2 pixel, graphene ink-based IDSS process; (e) AFM image of a SiO_2/Si substrate area ever covered by inkjet-dispensed graphene ink droplet; (f) SEM images of IDSS-produced out-of-plane MoS_2/graphene pixel.

6.5 Summary

In this study, we developed an IDSS method, which enables scalable fabrication of MoS_2 structures at designated locations on a chip substrate without requiring additional lithography and etching processes. In the IDSS process, inkjet-dispensed microscale liquid droplets (*i.e.* DI water or graphene ink) first predefine the target locations on a substrate and in-plane or out-of-plane MoS_2 structures are subsequently synthesized at the defined locations on the substrate during the site-selective CVD process. We attributed such selective growth capability of IDSS to local topography change within droplet-covered regions, which serves as effective nucleation seeds during the CVD process. Especially, as well as the site-selective capability, IDSS can also be a facile and controllable method to produce MoS_2 microstructures bearing different crystal morphologies. By depositing DI water droplets during the IDSS process, in-plane MoS_2 features are dominantly synthesized at defined locations. Such in-plane MoS_2 features fabricated into an array of the working transistors exhibit a good uniformity in their transfer characteristics. Furthermore, graphene ink droplets applied during the IDSS process dominantly induce out-of-plane MoS_2 features selectively synthesized on top of inkjet-printed graphene flakes. Such a hierarchical structure of out-of-plane MoS_2/graphene was fabricated and demonstrated into a miniaturized lithium-ion battery electrode structure, which exhibits appealing electrochemical characteristics because of abundant edges in the out-of-plane MoS_2 in combination with efficient charge collecting and delivering by the graphene. The IDSS method could be a promising cost-efficient scalable nanomanufacturing technique, which can pave the way to the development of a new generation miniaturized on-chip energy storage devices.

APPENDICES

Appendix A

IL-1β Quantification in Serum Using Standard ELISA

Figure A.1 (a) and (b) plot such an ELISA-measured correlation curve in linear and semilogarithmic scales, respectively. Figure A.1 (c) displays a photograph of the ELISA wells used for obtaining the correlation curve. Figure A.1 (b) shows that, for IL-1β concentrations less than 1 pM, the ELISA signals can be hardly resolved from the zero concentration baseline, and the LOD of the standard ELISA for IL-1β quantification in serum is estimated to be ~1 pM.

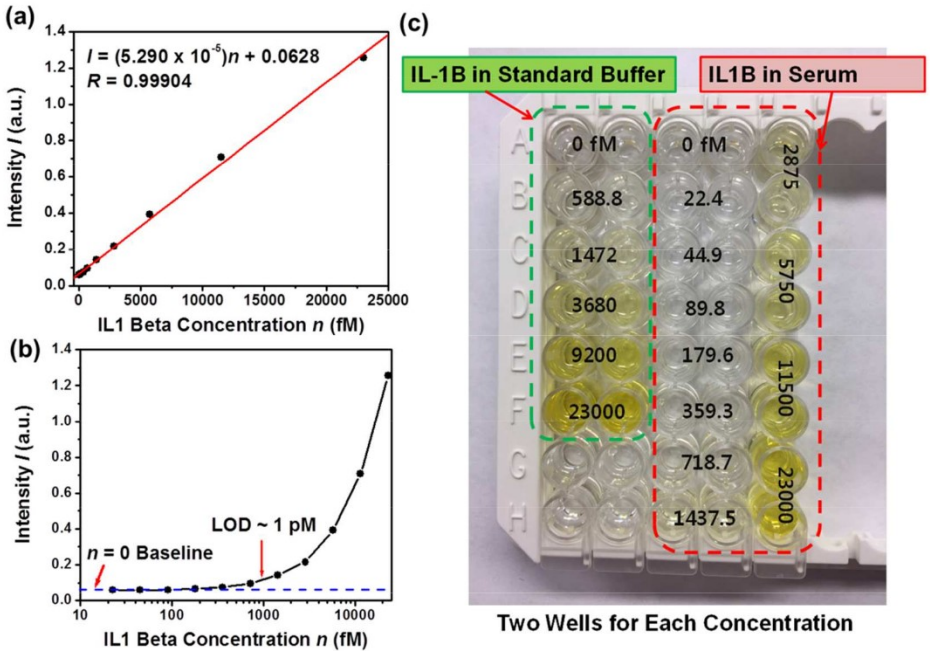

Figure A.1 IL-1β quantification in serum obtained by using standard ELISA: (a) and (b) display the ELISA-measured correlation curve for IL-1β quantification in serum, plotted in linear and semilogarithmic scales, respectively; (c) a photograph

of the ELISA wells used for obtaining the correlation curves for IL-1β quantification in serum and standard buffer.

A comparison of the LOD and incubation time parameters obtained by the presented IFDM cycle-wise method based on MoS_2 sensors, other representative FET biosensors, and advanced ELISA

Table A.1 Comparison of Limit-of-Detection and Incubation Time Parameters Obtained by Cycle-Wise Method Based on MoS_2 Field-Effect Transistors (FETs), Other Representative FET Biosensors, and Advanced ELISA Method.

Devices or Methods	**Target Molecules**	**Limit of Detection (LOD) or The Reported Lowest Analyte Concentration**	**Incubation Time for Quantifying Femtomolar (or The Reported Lowest) Analyte Concentration**
MoS_2 FETs [35]	Streptavidin	100 fM	N.A.
MoS_2 FETs [95]	Prostate specific antigen (PSA)	375 fM	N.A.
Graphene FETs [92]	Deoxyribonucleic acids (DNAs)	100 fM	~ 1 hour
Si Nanowire FETs [94]	Prostate specific antigen (PSA)	10 nM	~ 50 minute
Si Nanowire FETs [93]	DNA	3 nM	~ 83 minute
Advanced ELISA [98]	Interleukin 1-β	10 fM	Several Hours
Our work: MoS_2 FETs + IFDM Cycle	Interleukin 1-β	1 fM	~ 20 minute

Appendix B

Calibration Curves of IL-1β and PCT.

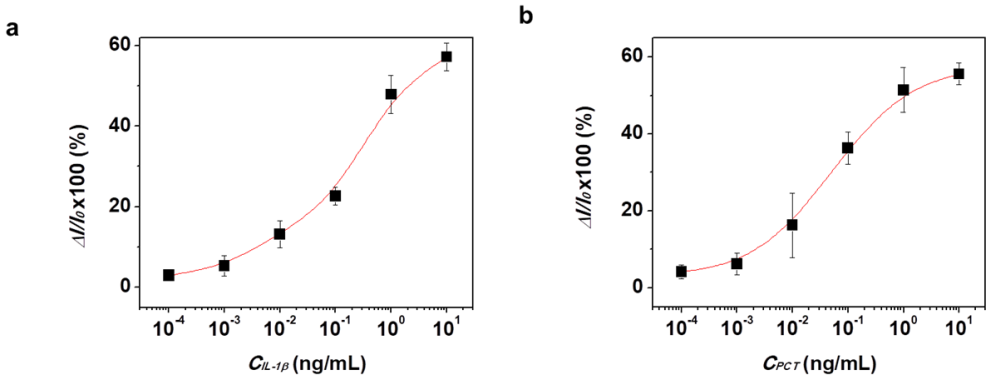

Figure B.1 Calibration curves of (a) $C_{IL\text{-}1\beta}$ and (b) C_{PCT} in sham. The value of $\Delta I/I_0$ x100 represents the photocurrent variation in % at 10 min. All the detections were performed at λ = 650nm and P = 2.4 mW/cm^2. The estimated K_d values are 0.572 ng/mL, 0.717 ng/mL, and 0.658 ng/mL for CitH3, PCT, and IL-1β, respectively.

Limit-of-Detections of Sepsis Biomarkers.

Table B.1 Estimated LOD for IL-1β and PCT in sham mice serum using the iNOBS device. We experimentally determined the LOD values for the three sepsis-related biomarkers in serum samples from sham mice.

	Blank S.D. (σ) (%)	**Usystem (3σ) (%)**	**k slope (pg/mL)-1**	**LOD=3σ/kslope (pg/mL)**
CitH3	0.00093	0.00280	0.0032	0.87
IL-1β	0.00176	0.0052784	0.0043	1.22
PCT	0.00197	0.00591	0.0036	1.64

Bibliography

[1] K. S. Novoselov, A. K. Geim, S. V. Morozov, D. Jiang, Y. Zhang, S. V. Dubonos, I. V. Grigorieva, and A. A. Firsov, "Electric Field Effect in Atomically Thin Carbon Films," *Science,* vol. 306, pp. 666-669, 2004.
[2] P. Miro, M. Audiffred, and T. Heine, "An Atlas of Two-Dimensional Materials," *Chemical Society Reviews,* vol. 43, pp. 6537-6554, 2014.
[3] C. Lee, X. D. Wei, J. W. Kysar, and J. Hone, "Measurement of The Elastic Properties and Intrinsic Strength of Monolayer Graphene," *Science,* vol. 321, pp. 385-388, 2008.
[4] G. Tsoukleri, J. Parthenios, K. Papagelis, R. Jalil, A. C. Ferrari, A. K. Geim, K. S. Novoselov, and C. Galiotis, "Subjecting a graphene monolayer to tension and compression," *small,* vol. 5, pp. 2397-2402, 2009.
[5] A. K. Geim, and K. S. Novoselov, The rise of graphene. In *Nanoscience and technology: a collection of reviews from nature journals*, World Scientific: 2010; pp 11-19.
[6] K. S. Novoselov, A. K. Geim, S. V. Morozov, D. Jiang, M. I. Katsnelson, I. V. Grigorieva, S. V. Dubonos, and A. A. Firsov, "Two-Dimensional Gas of Massless Dirac Fermions in Graphene," *Nature,* vol. 438, pp. 197-200, 2005.
[7] L. Li, Y. Yu, G. J. Ye, Q. Ge, X. Ou, H. Wu, D. Feng, X. H. Chen, and Y. Zhang, "Black Phosphorus Field-Effect Transistors," *Nature Nanotechnology,* vol. 9, pp. 372-377, 2014.
[8] L. Song, L. Ci, H. Lu, P. B. Sorokin, C. Jin, J. Ni, A. G. Kvashnin, D. G. Kvashnin, J. Lou, B. I. Yakobson, and P. M. Ajayan, "Large Scale Growth and Characterization of Atomic Hexagonal Boron Nitride Layers," *Nano Letters,* vol. 10, pp. 3209-3215, 2010.
[9] R. F. Frindt, "Single Crystals of MoS_2 Several Molecular Layers Thick," *Journal of Applied Physics,* vol. 37, pp. 1928-1929, 1966.
[10] C. Donnet, J. Martin, T. Le Mogne, and M. Belin, "Super-low friction of MoS2 coatings in various environments," *Tribology International,* vol. 29, pp. 123-128, 1996.
[11] B. Radisavljevic, A. Radenovic, J. Brivio, V. Giacometti, and A. Kis, "Single-Layer MoS_2 Transistors," *Nature Nanotechnology,* vol. 6, pp. 147-150, 2011.
[12] K. F. Mak, C. Lee, J. Hone, J. Shan, and T. F. Heinz, "Atomically thin MoS 2: a new direct-gap semiconductor," *Physical review letters,* vol. 105, pp. 136805, 2010.
[13] G. Frey, S. Elani, M. Homyonfer, Y. Feldman, and R. Tenne, "Optical-absorption spectra of inorganic fullerenelike M S 2 (M= Mo, W)," *Physical Review B,* vol. 57, pp. 6666, 1998.
[14] T. Roy, M. Tosun, J. S. Kang, A. B. Sachid, S. B. Desai, M. Hettick, C. C. Hu, and A. Javey, "Field-effect transistors built from all two-dimensional material components," *ACS nano,* vol. 8, pp. 6259-6264, 2014.
[15] A. Castellanos-Gomez, M. Poot, G. A. Steele, H. S. Van Der Zant, N. Agraït, and G. Rubio-Bollinger, "Elastic properties of freely suspended MoS2 nanosheets," *Advanced Materials,* vol. 24, pp. 772-775, 2012.
[16] S. Bertolazzi, J. Brivio, and A. Kis, "Stretching and Breaking of Ultrathin MoS_2," *ACS Nano,* vol. 5, pp. 9703-9709, 2011.
[17] R. Cheng, S. Jiang, Y. Chen, Y. Liu, N. Weiss, H.-C. Cheng, H. Wu, Y. Huang, and X. Duan, "Few-layer molybdenum disulfide transistors and circuits for high-speed flexible electronics," *Nature communications,* vol. 5, pp. 1-9, 2014.

[18] D. Akinwande, N. Petrone, and J. Hone, "Two-dimensional flexible nanoelectronics," *Nature communications,* vol. 5, pp. 1-12, 2014.
[19] S. W. Wang, F. Tristan, D. Minami, T. Fujimori, R. Cruz-Silva, M. Terrones, K. Takeuchi, K. Teshima, F. Rodriguez-Reinoso, M. Endo, and K. Kaneko, "Activation Routes for High Surface Area Graphene Monoliths from Graphene Oxide Colloids," *Carbon,* vol. 76, pp. 220-231, 2014.
[20] P. Afanasiev, G.-F. Xia, G. Berhault, B. Jouguet, and M. Lacroix, "Surfactant-Assisted Synthesis of Highly Dispersed Molybdenum Sulfide," *Chemistry of Materials,* vol. 11, pp. 3216-3219, 1999.
[21] H. Li, Z. Y. Yin, Q. Y. He, H. Li, X. Huang, G. Lu, D. W. H. Fam, A. I. Y. Tok, Q. Zhang, and H. Zhang, "Fabrication of Single- and Multilayer MoS_2 Film-Based Field-Effect Transistors for Sensing NO at Room Temperature," *Small,* vol. 8, pp. 63-67, 2012.
[22] W. J. Zhou, Z. Y. Yin, Y. P. Du, X. Huang, Z. Y. Zeng, Z. X. Fan, H. Liu, J. Y. Wang, and H. Zhang, "Synthesis of Few-Layer MoS_2 Nanosheet-Coated TiO_2 Nanobelt Heterostructures for Enhanced Photocatalytic Activities," *Small,* vol. 9, pp. 140-147, 2013.
[23] J. Kibsgaard, Z. B. Chen, B. N. Reinecke, and T. F. Jaramillo, "Engineering The Surface Structure of MoS_2 to Preferentially Expose Active Edge Sites for Electrocatalysis," *Nature Materials,* vol. 11, pp. 963-969, 2012.
[24] M.-L. Tsai, S.-H. Su, J.-K. Chang, D.-S. Tsai, C.-H. Chen, C.-I. Wu, L.-J. Li, L.-J. Chen, and J.-H. He, "Monolayer MoS_2 Heterojunction Solar Cells," *Acs Nano,* vol. 8, pp. 8317-8322, 2014.
[25] J. A. Wilson, and A. D. Yoffe, "The Transition Metal Dichalcogenides Discussion and Interpretation of The Observed Optical, Electrical and Structural Properties," *Advances in Physics,* vol. 18, pp. 193-335, 1969.
[26] Mattheis.Lf, "Band Structures of Transition-Metal-Dichalcogenide Layer Compounds," *Physical Review B,* vol. 8, pp. 3719-3740, 1973.
[27] N. V. Podberezskaya, S. A. Magarill, N. V. Pervukhina, and S. V. Borisov, "Crystal Chemistry of Dichalcogenides MX_2," *Journal of Structural Chemistry,* vol. 42, pp. 654-681, 2001.
[28] Q. H. Wang, K. Kalantar-Zadeh, A. Kis, J. N. Coleman, and M. S. Strano, "Electronics and Optoelectronics of Two-Dimensional Transition Metal Dichalcogenides," *Nature Nanotechnology,* vol. 7, pp. 699-712, 2012.
[29] S. Z. Butler, S. M. Hollen, L. Cao, Y. Cui, J. A. Gupta, H. R. Gutiérrez, T. F. Heinz, S. S. Hong, J. Huang, A. F. Ismach, E. Johnston-Halperin, M. Kuno, V. V. Plashnitsa, R. D. Robinson, R. S. Ruoff, S. Salahuddin, J. Shan, L. Shi, M. G. Spencer, M. Terrones, W. Windl, and J. E. Goldberger, "Progress, Challenges, and Opportunities in Two-Dimensional Materials Beyond Graphene," *Acs Nano,* vol. 7, pp. 2898-2926, 2013.
[30] H. Li, G. Lu, Z. Y. Yin, Q. Y. He, H. Li, Q. Zhang, and H. Zhang, "Optical Identification of Single- and Few-Layer MoS_2 Sheets," *Small,* vol. 8, pp. 682-686, 2012.
[31] D. J. Late, B. Liu, H. S. S. R. Matte, C. N. R. Rao, and V. P. Dravid, "Rapid Characterization of Ultrathin Layers of Chalcogenides on SiO_2/Si Substrates," *Advanced Functional Materials,* vol. 22, pp. 1894-1905, 2012.
[32] W. Ying Ying, G. Ren Xi, N. Zhen Hua, H. Hui, G. Shu Peng, Y. Huan Ping, C. Chun Xiao, and Y. Ting, "Thickness Identification of Two-Dimensional Materials by Optical Imaging," *Nanotechnology,* vol. 23, pp. 495713, 2012.

[33] K. Kalantar-zadeh, and J. Z. Ou, "Biosensors based on two-dimensional MoS2," *Acs Sensors,* vol. 1, pp. 5-16, 2016.
[34] G. Yang, C. Zhu, D. Du, J. Zhu, and Y. Lin, "Graphene-like two-dimensional layered nanomaterials: applications in biosensors and nanomedicine," *Nanoscale,* vol. 7, pp. 14217-14231, 2015.
[35] D. Sarkar, W. Liu, X. Xie, A. C. Anselmo, S. Mitragotri, and K. Banerjee, "MoS2 field-effect transistor for next-generation label-free biosensors," *ACS nano,* vol. 8, pp. 3992-4003, 2014.
[36] Q. H. Wang, K. Kalantar-Zadeh, A. Kis, J. N. Coleman, and M. S. Strano, "Electronics and optoelectronics of two-dimensional transition metal dichalcogenides," *Nature nanotechnology,* vol. 7, pp. 699, 2012.
[37] K. Kalantar-zadeh, J. Z. Ou, T. Daeneke, M. S. Strano, M. Pumera, and S. L. Gras, "Two-dimensional transition metal dichalcogenides in biosystems," *Advanced Functional Materials,* vol. 25, pp. 5086-5099, 2015.
[38] E. Stern, R. Wagner, F. J. Sigworth, R. Breaker, T. M. Fahmy, and M. A. Reed, "Importance of the Debye screening length on nanowire field effect transistor sensors," *Nano letters,* vol. 7, pp. 3405-3409, 2007.
[39] H. Nam, B.-R. Oh, P. Chen, J. S. Yoon, S. Wi, M. Chen, K. Kurabayashi, and X. Liang, "Two different device physics principles for operating MoS2 transistor biosensors with femtomolar-level detection limits," *Applied Physics Letters,* vol. 107, pp. 012105, 2015.
[40] L. Britnell, R. M. Ribeiro, A. Eckmann, R. Jalil, B. D. Belle, A. Mishchenko, Y. J. Kim, R. V. Gorbachev, T. Georgiou, S. V. Morozov, A. N. Grigorenko, A. K. Geim, C. Casiraghi, A. H. C. Neto, and K. S. Novoselov, "Strong Light-Matter Interactions in Heterostructures of Atomically Thin Films," *Science,* vol. 340, pp. 1311-1314, 2013.
[41] Y. Park, B. Ryu, Q. Deng, B. Pan, Y. Song, Y. Tian, H. B. Alam, Y. Li, X. Liang, and K. Kurabayashi, "An Integrated Plasmo-Photoelectronic Nanostructure Biosensor Detects an Infection Biomarker Accompanying Cell Death in Neutrophils," *Small,* vol. 16, pp. 1905611, 2020.
[42] R. De La Rica, and M. M. Stevens, "Plasmonic ELISA for the ultrasensitive detection of disease biomarkers with the naked eye," *Nature nanotechnology,* vol. 7, pp. 821, 2012.
[43] E. Engvall, and P. Perlmann, "Enzyme-linked immunosorbent assay (ELISA)," *Protides of the biological fluids,* vol., pp. 553-556, 1971.
[44] B.-R. Oh, N.-T. Huang, W. Chen, J. H. Seo, P. Chen, T. T. Cornell, T. P. Shanley, J. Fu, and K. Kurabayashi, "Integrated nanoplasmonic sensing for cellular functional immunoanalysis using human blood," *Acs Nano,* vol. 8, pp. 2667-2676, 2014.
[45] B. Berg, B. Cortazar, D. Tseng, H. Ozkan, S. Feng, Q. Wei, R. Y.-L. Chan, J. Burbano, Q. Farooqui, and M. Lewinski, "Cellphone-based hand-held microplate reader for point-of-care testing of enzyme-linked immunosorbent assays," *ACS nano,* vol. 9, pp. 7857-7866, 2015.
[46] B. Ryu, H. Nam, B.-R. Oh, Y. Song, P. Chen, Y. Park, W. Wan, K. Kurabayashi, and X. Liang, "Cyclewise operation of printed MoS2 transistor biosensors for rapid biomolecule quantification at femtomolar levels," *ACS sensors,* vol. 2, pp. 274-281, 2017.
[47] A. Gao, N. Lu, Y. Wang, and T. Li, "Robust ultrasensitive tunneling-FET biosensor for point-of-care diagnostics," *Scientific reports,* vol. 6, pp. 22554, 2016.

[48] T.-W. Lin, P.-J. Hsieh, C.-L. Lin, Y.-Y. Fang, J.-X. Yang, C.-C. Tsai, P.-L. Chiang, C.-Y. Pan, and Y.-T. Chen, "Label-free detection of protein-protein interactions using a calmodulin-modified nanowire transistor," *Proceedings of the National Academy of Sciences,* vol. 107, pp. 1047-1052, 2010.
[49] C. Zhang, J.-Q. Xu, Y.-T. Li, L. Huang, D.-W. Pang, Y. Ning, W.-H. Huang, Z. Zhang, and G.-J. Zhang, "Photocatalysis-induced renewable field-effect transistor for protein detection," *Analytical chemistry,* vol. 88, pp. 4048-4054, 2016.
[50] Y. Huang, E. Sutter, N. N. Shi, J. Zheng, T. Yang, D. Englund, H.-J. Gao, and P. Sutter, "Reliable exfoliation of large-area high-quality flakes of graphene and other two-dimensional materials," *ACS nano,* vol. 9, pp. 10612-10620, 2015.
[51] S. Li, Y.-C. Lin, X.-Y. Liu, Z. Hu, J. Wu, H. Nakajima, S. Liu, T. Okazaki, W. Chen, and T. Minari, "Wafer-scale and deterministic patterned growth of monolayer MoS 2 via vapor–liquid–solid method," *Nanoscale,* vol. 11, pp. 16122-16129, 2019.
[52] R. Addou, S. McDonnell, D. Barrera, Z. Guo, A. Azcatl, J. Wang, H. Zhu, C. L. Hinkle, M. Quevedo-Lopez, and H. N. Alshareef, "Impurities and electronic property variations of natural MoS2 crystal surfaces," *ACS nano,* vol. 9, pp. 9124-9133, 2015.
[53] M. Amani, M. L. Chin, A. L. Mazzoni, R. A. Burke, S. Najmaei, P. M. Ajayan, J. Lou, and M. Dubey, "Growth-substrate induced performance degradation in chemically synthesized monolayer MoS2 field effect transistors," *Applied Physics Letters,* vol. 104, pp. 203506, 2014.
[54] L. Wang, Y. Wang, J. I. Wong, T. Palacios, J. Kong, and H. Y. Yang, "Functionalized MoS_2 Nanosheet-Based Field-Effect Biosensor for Label-Free Sensitive Detection of Cancer Marker Proteins in Solution," *Small,* vol. 10, pp. 1101-1105, 2014.
[55] D. Sarkar, W. Liu, X. J. Xie, A. C. Anselmo, S. Mitragotri, and K. Banerjee, "MoS_2 Field-Effect Transistor for Next-Generation Label-Free Biosensors," *ACS Nano,* vol. 8, pp. 3992-4003, 2014.
[56] M. Chen, H. Nam, H. Rokni, S. Wi, J. S. Yoon, P. Chen, K. Kurabayashi, W. Lu, and X. Liang, "Nanoimprint-Assisted Shear Exfoliation (NASE) for Producing Multilayer MoS_2 Structures as Field-Effect Transistor Channel Arrays," *ACS Nano,* vol. 9, pp. 8773-8785, 2015.
[57] H. Nam, B. R. Oh, P. Y. Chen, M. K. Chen, S. J. Wi, W. J. Wan, K. Kurabayashi, and X. G. Liang, "Multiple MoS2 Transistors for Sensing Molecule Interaction Kinetics," *Scientific Reports,* vol. 5, pp. 2015.
[58] J. Lee, P. Dak, Y. Lee, H. Park, W. Choi, M. A. Alam, and S. Kim, "Two-Dimensional Layered MoS_2 Biosensors Enable Highly Sensitive Detection of Biomolecules," *Scientific Reports,* vol. 4, pp. 7352/7351-7352/7357, 2014.
[59] H. Nam, B. R. Oh, P. Chen, J. S. Yoon, S. Wi, M. K. Chen, K. Kurabayashi, and X. Liang, "Two Different Device Physics Principles for Operating MoS_2 Transistor Biosensors with Femtomolar-Level Detection Limits," *Applied Physics Letters,* vol. 107, pp. 012105/012101-012105/012105, 2015.
[60] H. Nam, B. R. Oh, M. K. Chen, S. Wi, D. Li, K. Kurabayashi, and X. G. Liang, "Fabrication and comparison of MoS2 and WSe2 field-effect transistor biosensors," *Journal of Vacuum Science and Technology B,* vol. 33, pp. 2015.
[61] M. S. Luchansky, and R. C. Bailey, "Rapid, Multiparameter Profiling of Cellular Secretion Using Silicon Photonic Microring Resonator Arrays," *Journal of the American Chemical Society,* vol. 133, pp. 20500-20506, 2011.

[62] A. Atkinson, "Growth of Nio and Sio2 Thin-Films," *Philosophical Magazine, Part B,* vol. 55, pp. 637-650, 1987.
[63] D. Sarantaridis, and A. Atkinson, "Redox Cycling of Ni-Based Solid Oxide Fuel Cell Anodes: A Review," *Fuel Cells,* vol. 7, pp. 246-258, 2007.
[64] G. S. Kulkarni, and Z. H. Zhong, "Detection beyond the Debye Screening Length in a High-Frequency Nanoelectronic Biosensor," *Nano Letters,* vol. 12, pp. 719-723, 2012.
[65] W. H. Lee, J. M. Lee, M. Uhm, J. Lee, K. R. Kim, S. J. Choi, D. M. Kim, Y. J. Jeong, and D. H. Kim, "Characterization and Capacitive Modeling of Target Concentration-Dependent Subthreshold Swing in Silicon Nanoribbon Biosensors," *IEEE Electron Device Lett.,* vol. 35, pp. 587-589, 2014.
[66] K. Shoorideh, and C. O. Chui, "Optimization of the Sensitivity of FET-Based Biosensors via Biasing and Surface Charge Engineering," *IEEE Transactions on Electronic Devices,* vol. 59, pp. 3104-3110, 2012.
[67] K. Shoorideh, and C. O. Chui, "On the Origin of Enhanced Sensitivity in Nanoscale FET-Based Biosensors," *Proc Natl Acad Sci U S A,* vol. 111, pp. 5111-5116, 2014.
[68] D. J. Late, B. Liu, H. S. S. R. Matte, V. P. Dravid, and C. N. R. Rao, "Hysteresis in Single-Layer MoS_2 Field Effect Transistors," *ACS Nano,* vol. 6, pp. 5635-5641, 2012.
[69] M. S. Choi, G. H. Lee, Y. J. Yu, D. Y. Lee, S. H. Lee, P. Kim, J. Hone, and W. J. Yoo, "Controlled Charge Trapping by Molybdenum Disulphide and Graphene in Ultrathin Heterostructured Memory Devices," *Nature Communications,* vol. 4, pp. 2013.
[70] Y. Zhou, S. T. Han, P. Sonar, and V. A. L. Roy, "Nonvolatile Multilevel Data Storage Memory Device from Controlled Ambipolar Charge Trapping Mechanism," *Scientific Reports,* vol. 3, pp. 2319/2311-2319/2317, 2013.
[71] M. K. Chen, H. Nam, S. Wi, G. Priessnitz, I. M. Gunawan, and X. G. Liang, "Multibit Data Storage States Formed in Plasma-Treated MoS_2 Transistors," *ACS Nano,* vol. 8, pp. 4023-4032, 2014.
[72] W. Z. Bao, X. H. Cai, D. Kim, K. Sridhara, and M. S. Fuhrer, "High Mobility Ambipolar MoS_2 Field-Effect Transistors: Substrate and Dielectric Effects," *Applied Physics Letters,* vol. 102, pp. 042104/042101-042104/042103, 2013.
[73] M. Chen, H. Nam, S. Wi, J. Lian, X. Ren, L. F. Bian, S. Lu, and X. G. Liang, "Stable Few-Layer MoS_2 Diodes Formed by Plasma-Assisted Doping," *Applied Physics Letters,* vol. 103, pp. 142110/142111-142110/142114 2013.
[74] H. Nam, S. Wi, H. Rokni, M. K. Chen, G. Priessnitz, W. Lu, and X. G. Liang, "MoS_2 Transistors Fabricated *via* Plasma-Assisted Nanoprinting of Few-Layer MoS_2 Flakes into Large-Area Arrays," *ACS Nano,* vol. 7, pp. 5870-5881, 2013.
[75] X. X. Duan, Y. Li, N. K. Rajan, D. A. Routenberg, Y. Modis, and M. A. Reed, "Quantification of The Affinities and Kinetics of Protein Interactions Using Silicon Nanowire Biosensors," *Nature Nanotechnology,* vol. 7, pp. 401-407, 2012.
[76] H. Li, M. Du, M. J. Mleczko, A. L. Koh, Y. Nishi, E. Pop, A. J. Bard, and X. L. Zheng, "Kinetic Study of Hydrogen Evolution Reaction over Strained MoS_2 with Sulfur Vacancies Using Scanning Electrochemical Microscopy," *Journal of the American Chemical Society,* vol. 138, pp. 5123-5129, 2016.

[77] W. Kim, A. Javey, O. Vermesh, O. Wang, Y. M. Li, and H. J. Dai, "Hysteresis caused by water molecules in carbon nanotube field-effect transistors," *Nano Letters,* vol. 3, pp. 193-198, 2003.
[78] Y. Park, H. W. Baac, J. Heo, and G. Yoo, "Thermally Activated Trap Charges Responsible for Hysteresis in Multilayer MoS_2 Field-Effect Transistors," *Applied Physics Letters,* vol. 108, pp. 083102/083101-083102/083105, 2016.
[79] J. P. Shu, G. T. Wu, Y. Guo, B. Liu, X. L. Wei, and Q. Chen, "The Intrinsic Origin of Hysteresis in MoS_2 Field Effect Transistors," *Nanoscale,* vol. 8, pp. 3049-3056, 2016.
[80] E. Hotoura, V. Giapros, A. Kostoula, P. Spyrou, and S. Andronikou, "Pre-Inflammatory Mediators and Lymphocyte Subpopulations in Preterm Neonates with Sepsis," *Inflammation,* vol. 35, pp. 1094-1101, 2012.
[81] J. D. Faix, "Biomarkers of Sepsis," *Crit Rev Clin Lab Sci,* vol. 50, pp. 23-36, 2013.
[82] L. Gullestad, T. Ueland, L. E. Vinge, A. Finsen, A. Yndestad, and P. Aukrust, "Inflammatory Cytokines in Heart Failure: Mediators and Markers," *Cardiology,* vol. 122, pp. 23-35, 2012.
[83] M. L. Schmitz, A. Weber, T. Roxlau, M. Gaestel, and M. Kracht, "Signal Integration, Crosstalk Mechanisms and Networks in The Function of Inflammatory Cytokines," *Biochimica Et Biophysica Acta-Molecular Cell Research,* vol. 1813, pp. 2165-2175, 2011.
[84] D. F. Mangan, G. R. Welch, and S. M. Wahl, "Lipopolysaccharide, Tumor-Necrosis-Factor-Alpha, and Il-1-Beta Prevent Programmed Cell-Death (Apoptosis) in Human Peripheral-Blood Monocytes," *Journal of Immunology,* vol. 146, pp. 1541-1546, 1991.
[85] R. M. Friedlander, V. Gagliardini, R. J. Rotello, and J. Y. Yuan, "Functional Role of Interleukin 1 beta (IL-1 beta) in IL-1 Beta-Converting Enzyme-Mediated Apoptosis," *Journal of Experimental Medicine,* vol. 184, pp. 717-724, 1996.
[86] C. A. Dinarello, "Historical Insights into Cytokines," *European Journal of Immunology,* vol. 37, pp. S34-S45, 2007.
[87] C. Y. Chiang, M. L. Hsieh, K. W. Huang, L. K. Chau, C. M. Chang, and S. R. Lyu, "Fiber-optic particle plasmon resonance sensor for detection of interleukin-1 beta in synovial fluids," *Biosensors and Bioelectronics,* vol. 26, pp. 1036-1042, 2010.
[88] B. Ebrahimi, S. L. Tucker, D. H. Li, J. L. Abbruzzese, and R. Kurzrock, "Cytokines in pancreatic carcinoma - Correlation with phenotypic characteristics and prognosis," *Cancer,* vol. 101, pp. 2727-2736, 2004.
[89] S. Mitsunaga, M. Ikeda, S. Shimizu, I. Ohno, J. Furuse, M. Inagaki, S. Higashi, H. Kato, K. Terao, and A. Ochiai, "Serum Levels of IL-6 and IL-1 Beta Can Predict The Efficacy of Gemcitabine in Patients with Advanced Pancreatic Cancer," *British Journal of Cancer,* vol. 108, pp. 2063-2069, 2013.
[90] M. Navazesh, and C. M. Christensen, "A Comparison of Whole Mouth Resting and Stimulated Salivary Measurement Procedures," *Journal of Dental Research,* vol. 61, pp. 1158-1162, 1982.
[91] J. Quereda, A. Castellanos-Gomez, N. Agrait, and G. Rubio-Bollinger, "Single-layer MoS2 roughness and sliding friction quenching by interaction with atomically flat substrates," *Applied Physics Letters,* vol. 105, pp. 2014.

[92] B. Cai, S. Wang, L. Huang, Y. Ning, Z. Zhang, and G.-J. Zhang, "Ultrasensitive label-free detection of PNA–DNA hybridization by reduced graphene oxide field-effect transistor biosensor," *ACS nano,* vol. 8, pp. 2632-2638, 2014.
[93] N. Gao, W. Zhou, X. Jiang, G. Hong, T.-M. Fu, and C. M. Lieber, "General strategy for biodetection in high ionic strength solutions using transistor-based nanoelectronic sensors," *Nano letters,* vol. 15, pp. 2143-2148, 2015.
[94] X. Duan, Y. Li, N. K. Rajan, D. A. Routenberg, Y. Modis, and M. A. Reed, "Quantification of the affinities and kinetics of protein interactions using silicon nanowire biosensors," *Nature nanotechnology,* vol. 7, pp. 401, 2012.
[95] L. Wang, Y. Wang, J. I. Wong, T. Palacios, J. Kong, and H. Y. Yang, "Functionalized MoS2 nanosheet-based field-effect biosensor for label-free sensitive detection of cancer marker proteins in solution," *Small,* vol. 10, pp. 1101-1105, 2014.
[96] B. Ebrahimi, S. L. Tucker, D. Li, J. L. Abbruzzese, and R. Kurzrock, "Cytokines in pancreatic carcinoma: correlation with phenotypic characteristics and prognosis," *Cancer: Interdisciplinary International Journal of the American Cancer Society,* vol. 101, pp. 2727-2736, 2004.
[97] C.-Y. Chiang, M.-L. Hsieh, K.-W. Huang, L.-K. Chau, C.-M. Chang, and S.-R. Lyu, "Fiber-optic particle plasmon resonance sensor for detection of interleukin-1β in synovial fluids," *Biosensors and Bioelectronics,* vol. 26, pp. 1036-1042, 2010.
[98] S. Mitsunaga, M. Ikeda, S. Shimizu, I. Ohno, J. Furuse, M. Inagaki, S. Higashi, H. Kato, K. Terao, and A. Ochiai, "Serum levels of IL-6 and IL-1β can predict the efficacy of gemcitabine in patients with advanced pancreatic cancer," *British journal of cancer,* vol. 108, pp. 2063, 2013.
[99] C. A. Dinarello, "Historical Review of Cytokines," *European journal of immunology,* vol. 37, pp. S34-S45, 2007.
[100] T. Meager, *The Molecular Biology of Cytokines*. John Wiley & Sons: New York, NY, 1998.
[101] A. W. Thompson, and M. T. Lotze, *The Cytokine Handbook 4th Edition*. Academic Press: Amsterdam, Netherlands, 2003.
[102] J. Bienvenu, G. Monneret, N. Fabien, and J. P. Revillard, "The clinical usefulness of the measurement of cytokines," *Clinical Chemistry and Laboratory Medicine,* vol. 38, pp. 267-285, 2000.
[103] D. Payen, G. Monneret, and R. Hotchkiss, "Immunotherapy - a potential new way forward in the treatment of sepsis," *Critical Care,* vol. 17, pp. 2013.
[104] S. A. Rosenberg, J. C. Yang, and N. P. Restifo, "Cancer immunotherapy: moving beyond current vaccines," *Nature Medicine,* vol. 10, pp. 909-915, 2004.
[105] B. Ludewig, A. F. Ochsenbein, B. Odermatt, D. Paulin, H. Hengartner, and R. M. Zinkernagel, "Immunotherapy with dendritic cells directed against tumor antigens shared with normal host cells results in severe autoimmune disease," *Journal of Experimental Medicine,* vol. 191, pp. 795-803, 2000.
[106] R. Valenta, "The future of antigen-specific immunotherapy of allergy," *Nature Reviews Immunology,* vol. 2, pp. 446-453, 2002.
[107] S. Siebert, A. Tsoukas, J. Robertson, and I. McInnes, "Cytokines as Therapeutic Targets in Rheumatoid Arthritis and Other Inflammatory Diseases," *Pharmacological Reviews,* vol. 67, pp. 280-309, 2015.

[108] S. R. Targan, S. B. Hanauer, S. J. H. vanDeventer, L. Mayer, D. H. Present, T. Braakman, K. L. DeWoody, T. F. Schaible, and P. J. Rutgeerts, "A short-term study of chimeric monoclonal antibody cA2 to tumor necrosis factor alpha for Crohn's disease," *New England Journal of Medicine,* vol. 337, pp. 1029-1035, 1997.
[109] E. Abraham, "Why immunomodulatory therapies have not worked in sepsis," *Intensive Care Medicine,* vol. 25, pp. 556-566, 1999.
[110] M. P. Fink, and H. S. Warren, "Strategies to improve drug development for sepsis," *Nature Reviews Drug Discovery,* vol. 13, pp. 741-758, 2014.
[111] W. J.Kox, T.Volk, S.N.Kox, and H.-D.Volk, "Immunomodulatory therapies in sepsis," *Intensive Care Medicine,* vol. 26, pp. S124-S128, 2000.
[112] M. F. Osuchowski, J. Connett, K. Welch, J. Granger, and D. G. Remick, "Stratification is the key: Inflammatory biomarkers accurately direct immunomodulatory therapy in experimental sepsis," *Critical Care Medicine,* vol. 37, pp. 1567-1573, 2009.
[113] H. R. Wong, S. L. Weiss, J. S. Giuliano, M. S. Wainwright, N. Z. Cvijanovich, N. J. Thomas, G. L. Allen, N. Anas, M. T. Bigham, M. Hall, R. J. Freishtat, A. Sen, K. Meyer, P. A. Checchia, T. P. Shanley, J. Nowak, M. Quasney, A. Chopra, J. C. Fitzgerald, R. Gedeit, S. Banschbach, E. Beckman, P. Lahni, K. Hart, and C. J. Lindsell, "Testing the Prognostic Accuracy of the Updated Pediatric Sepsis Biomarker Risk Model," *Plos One,* vol. 9, pp. 2014.
[114] P. Chen, M. T. Chung, W. McHugh, R. Nidetz, Y. Li, J. Fu, T. T. Cornell, T. P. Shanley, and K. Kurabayashi, "Multiplex serum cytokine immunoassay using nanoplasmonic biosensor microarrays," *ACS nano,* vol. 9, pp. 4173-4181, 2015.
[115] B.-R. Oh, P. Chen, R. Nidetz, W. McHugh, J. Fu, T. P. Shanley, T. T. Cornell, and K. Kurabayashi, "Multiplexed Nanoplasmonic Temporal Profiling of T-Cell Response under Immunomodulatory Agent Exposure," *ACS sensors,* vol. 1, pp. 941-948, 2016.
[116] Z. Qu, H. Xu, P. Xu, K. Chen, R. Mu, J. Fu, and H. Gu, "Ultrasensitive ELISA using enzyme-loaded nanospherical brushes as labels," *Analytical chemistry,* vol. 86, pp. 9367-9371, 2014.
[117] H. C. Tekin, and M. A. Gijs, "Ultrasensitive protein detection: a case for microfluidic magnetic bead-based assays," *Lab on a Chip,* vol. 13, pp. 4711-4739, 2013.
[118] S. Ghatak, A. N. Pal, and A. Ghosh, "Nature of electronic states in atomically thin MoS2 field-effect transistors," *Acs Nano,* vol. 5, pp. 7707-7712, 2011.
[119] M. S. Fuhrer, and J. Hone, "Measurement of mobility in dual-gated MoS2 transistors," *Nature nanotechnology,* vol. 8, pp. 146-147, 2013.
[120] B. Radisavljevic, A. Radenovic, J. Brivio, i. V. Giacometti, and A. Kis, "Single-layer MoS2 transistors," *Nature nanotechnology,* vol. 6, pp. 147-150, 2011.
[121] D.-S. Tsai, K.-K. Liu, D.-H. Lien, M.-L. Tsai, C.-F. Kang, C.-A. Lin, L.-J. Li, and J.-H. He, "Few-layer MoS2 with high broadband photogain and fast optical switching for use in harsh environments," *Acs Nano,* vol. 7, pp. 3905-3911, 2013.
[122] D. Xiao, G.-B. Liu, W. Feng, X. Xu, and W. Yao, "Coupled spin and valley physics in monolayers of MoS 2 and other group-VI dichalcogenides," *Physical Review Letters,* vol. 108, pp. 196802, 2012.
[123] H. Nam, B.-R. Oh, M. Chen, S. Wi, D. Li, K. Kurabayashi, and X. Liang, "Fabrication and comparison of MoS2 and WSe2 field-effect transistor biosensors," *Journal of Vacuum Science & Technology B,* vol. 33, pp. 06FG01, 2015.

[124] H. Nam, B.-R. Oh, P. Chen, M. Chen, S. Wi, W. Wan, K. Kurabayashi, and X. Liang, "Multiple MoS2 Transistors for Sensing Molecule Interaction Kinetics," *Scientific reports,* vol. 5, pp. 10546-10546, 2014.
[125] M. Liu, X. Yin, and X. Zhang, "Double-layer graphene optical modulator," *Nano letters,* vol. 12, pp. 1482-1485, 2012.
[126] J. Miao, W. Hu, Y. Jing, W. Luo, L. Liao, A. Pan, S. Wu, J. Cheng, X. Chen, and W. Lu, "Surface Plasmon-Enhanced Photodetection in Few Layer MoS2 Phototransistors with Au Nanostructure Arrays," *small,* vol. 11, pp. 2392-2398, 2015.
[127] S. Su, H. Sun, W. Cao, J. Chao, H. Peng, X. Zuo, L. Yuwen, C. Fan, and L. Wang, "Dual-target electrochemical biosensing based on DNA structural switching on gold nanoparticle-decorated MoS2 nanosheets," *ACS applied materials & interfaces,* vol. 8, pp. 6826-6833, 2016.
[128] H. Sun, J. Chao, X. Zuo, S. Su, X. Liu, L. Yuwen, C. Fan, and L. Wang, "Gold nanoparticle-decorated MoS 2 nanosheets for simultaneous detection of ascorbic acid, dopamine and uric acid," *Rsc Advances,* vol. 4, pp. 27625-27629, 2014.
[129] O. Lopez-Sanchez, D. Lembke, M. Kayci, A. Radenovic, and A. Kis, "Ultrasensitive photodetectors based on monolayer MoS2," *Nat Nano,* vol. 8, pp. 497-501, 2013.
[130] H. Nam, S. Wi, H. Rokni, M. Chen, G. Priessnitz, W. Lu, and X. Liang, "MoS2 transistors fabricated via plasma-assisted nanoprinting of few-layer MoS2 flakes into large-area arrays," *ACS nano,* vol. 7, pp. 5870-5881, 2013.
[131] J. Alicea, Y. Oreg, G. Refael, F. von Oppen, and M. P. Fisher, "Non-Abelian statistics and topological quantum information processing in 1D wire networks," *Nature Physics,* vol. 7, pp. 412-417, 2011.
[132] S. L. Masters, A. Simon, I. Aksentijevich, and D. L. Kastner, "Horror autoinflammaticus: the molecular pathophysiology of autoinflammatory disease," *Annual review of immunology,* vol. 27, pp. 621, 2009.
[133] S. K. Dondapati, T. K. Sau, C. Hrelescu, T. A. Klar, F. D. Stefani, and J. Feldmann, "Label-free biosensing based on single gold nanostars as plasmonic transducers," *Acs Nano,* vol. 4, pp. 6318-6322, 2010.
[134] K. M. Mayer, S. Lee, H. Liao, B. C. Rostro, A. Fuentes, P. T. Scully, C. L. Nehl, and J. H. Hafner, "A label-free immunoassay based upon localized surface plasmon resonance of gold nanorods," *ACS nano,* vol. 2, pp. 687-692, 2008.
[135] X. Wang, Y. Li, H. Wang, Q. Fu, J. Peng, Y. Wang, J. Du, Y. Zhou, and L. Zhan, "Gold nanorod-based localized surface plasmon resonance biosensor for sensitive detection of hepatitis B virus in buffer, blood serum and plasma," *Biosensors and Bioelectronics,* vol. 26, pp. 404-410, 2010.
[136] A. J. Haes, and R. P. Van Duyne, "A nanoscale optical biosensor: sensitivity and selectivity of an approach based on the localized surface plasmon resonance spectroscopy of triangular silver nanoparticles," *Journal of the American Chemical Society,* vol. 124, pp. 10596-10604, 2002.
[137] L. S. Jung, C. T. Campbell, T. M. Chinowsky, M. N. Mar, and S. S. Yee, "Quantitative interpretation of the response of surface plasmon resonance sensors to adsorbed films," *Langmuir,* vol. 14, pp. 5636-5648, 1998.
[138] K. A. Willets, and R. P. Van Duyne, "Localized surface plasmon resonance spectroscopy and sensing," *Annu. Rev. Phys. Chem.,* vol. 58, pp. 267-297, 2007.

[139] F. B. Mayr, S. Yende, and D. C. Angus, "Epidemiology of severe sepsis," *Virulence,* vol. 5, pp. 4-11, 2014.
[140] S. Laukemann, N. Kasper, P. Kulkarni, D. Steiner, A. C. Rast, A. Kutz, S. Felder, S. Haubitz, L. Faessler, A. Huber, C. A. Fux, B. Mueller, and P. Schuetz, "Can We Reduce Negative Blood Cultures With Clinical Scores and Blood Markers? Results From an Observational Cohort Study," *Medicine,* vol. 94, pp. e2264, 2015.
[141] B. D. W. Group., "Biomarkers and surrogate endpoints: preferred definitions and conceptual framework," *Clin Pharmacol Ther,* vol. 69, pp. 89-95, 2001.
[142] J. C. Marshall, and K. Reinhart, "Biomarkers of sepsis," *Crit. Care. Med.,* vol. 37, pp. 2290-2298, 2009.
[143] E. Kolaczkowska, and P. Kubes, "Neutrophil recruitment and function in health and inflammation," *Nat Rev Immunol,* vol. 13, pp. 159, 2013.
[144] I. Neeli, S. N. Khan, and M. Radic, "Histone deimination as a response to inflammatory stimuli in neutrophils," *J Immunol,* vol. 180, pp. 1895-1902, 2008.
[145] Y. Li, B. Liu, E. Y. Fukudome, J. Lu, W. Chong, G. Jin, Z. Liu, G. C. Velmahos, M. Demoya, D. R. King, and H. B. Alam, "Identification of citrullinated histone H3 as a potential serum protein biomarker in a lethal model of lipopolysaccharide-induced shock," *Surgery,* vol. 150, pp. 442-451, 2011.
[146] B. Pan, H. B. Alam, W. Chong, J. Mobley, B. Liu, Q. Deng, Y. Liang, Y. Wang, E. Chen, T. Wang, M. Tewari, and Y. Li, "CitH3: a reliable blood biomarker for diagnosis and treatment of endotoxic shock," *Sci Rep,* vol. 7, pp. 8972, 2017.
[147] J. N. Anker, W. P. Hall, O. Lyandres, N. C. Shah, J. Zhao, and R. P. Van Duyne, "Biosensing with plasmonic nanosensors," *Nat. Mater.,* vol. 7, pp. 442-453, 2008.
[148] B. Sepulveda, P. C. Angelome, L. M. Lechuga, and L. M. Liz-Marzan, "LSPR-based nanobiosensors," *Nano Today,* vol. 4, pp. 244-251, 2009.
[149] X. C. Wang, T.-W.; Lin, G.; Gartia, M. R.; Liu, G. L., "Self-Referenced Smartphone-Based Nanoplasmonic Imaging Platform for Colorimetric Biochemical Sensing," *Anal Chem,* vol. 89, pp. 611-615, 2017.
[150] S. M. d. l. R. Russell, R., "Paper transducers to detect plasmon variations in colorimetric nanoparticle biosensors," *Sens Actuators, B,* vol. 270, pp. 327-332, 2018.
[151] F. Yesilkoy, R. A. Terborg, J. Pello, A. A. Belushkin, Y. Jahani, V. Pruneri, and H. Altug, "Phase-sensitive plasmonic biosensor using a portable and large field-of-view interferometric microarray imager," *Light: Sci. Appl.,* vol. 7, pp. 17152, 2018.
[152] K. M. Mayer, and J. H. Hafner, "Localized Surface Plasmon Resonance Sensors," *Chem Rev,* vol. 111, pp. 3828-3857, 2011.
[153] Y. Y. Wang, J. H. Zhou, and J. H. Li, "Construction of Plasmonic Nano-Biosensor-Based Devices for Point-of-Care Testing," *Small Methods,* vol. 1, pp. UNSP 1700197, 2017.
[154] P. Y. Chen, M. T. Chung, W. McHugh, R. Nidetz, Y. W. Li, J. P. Fu, T. T. Cornell, T. P. Shanley, and K. Kurabayashi, "Multiplex Serum Cytokine Immunoassay Using Nanoplasmonic Biosensor Microarrays," *ACS Nano,* vol. 9, pp. 4173-4181, 2015.
[155] Y. Zhang, Y. Tang, Y.-H. Hsieh, C.-Y. Hsu, J. Xi, K.-J. Lin, and X. Jiang, "Towards a high-throughput label-free detection system combining localized-surface plasmon resonance and microfluidics," *Lab Chip,* vol. 12, pp. 3012-3015, 2012.

[156] Y. Park, B. Ryu, B. R. Oh, Y. Song, X. Liang, and K. Kurabayashi, "Biotunable Nanoplasmonic Filter on Few-Layer MoS2 for Rapid and Highly Sensitive Cytokine Optoelectronic Immunosensing," *ACS Nano,* vol. 11, pp. 5697-5705, 2017.
[157] O. Lopez-Sanchez, D. Lembke, M. Kayci, A. Radenovic, and A. Kis, "Ultrasensitive photodetectors based on monolayer MoS2," *Nat. Nanotechnol.,* vol. 8, pp. 497, 2013.
[158] J. Pak, J. Jang, K. Cho, T.-Y. Kim, J.-K. Kim, Y. Song, W.-K. Hong, M. Min, H. Lee, and T. Lee, "Enhancement of photodetection characteristics of MoS2 field effect transistors using surface treatment with copper phthalocyanine," *Nanoscale,* vol. 7, pp. 18780-18788, 2015.
[159] W. Choi, M. Y. Cho, A. Konar, J. H. Lee, G.-B. Cha, S. C. Hong, S. Kim, J. Kim, D. Jena, J. Joo, and S. Kim, "High-Detectivity Multilayer MoS2 Phototransistors with Spectral Response from Ultraviolet to Infrared," *Adv. Mater.,* vol. 24, pp. 5832-5836, 2012.
[160] Z. Yin, H. Li, H. Li, L. Jiang, Y. Shi, Y. Sun, G. Lu, Q. Zhang, X. Chen, and H. Zhang, "Single-Layer MoS2 Phototransistors," *ACS Nano,* vol. 6, pp. 74-80, 2012.
[161] Q. Deng, B. Pan, H. Alam, Y. Liang, B. Liu, N. Mor-Vaknin, X. Duan, A. M. Williams, Y. Tian, Z. Wu, J. Zhang, and Y. Li, "Citrullinated Histone H3 as a Therapeutic Target for Endotoxic Shock in Mice," *Front Immunol,* vol. Under review, pp. 2019.
[162] J. Sebaugh, and P. McCray, "Defining the linear portion of a sigmoid-shaped curve: bend points," *Pharmaceutical Statistics: The Journal of Applied Statistics in the Pharmaceutical Industry,* vol. 2, pp. 167-174, 2003.
[163] S. J. Parker, and P. E. Watkins, "Experimental models of gram-negative sepsis," *Br J Surg,* vol. 88, pp. 22-30, 2001.
[164] K. A. Wichterman, A. E. Baue, and I. H. Chaudry, "Sepsis and septic shock--a review of laboratory models and a proposal," *J Surg Res,* vol. 29, pp. 189-201, 1980.
[165] S. Q. Latifi, M. A. O'Riordan, and A. D. Levine, "Interleukin-10 controls the onset of irreversible septic shock," *Infect Immun,* vol. 70, pp. 4441-4446, 2002.
[166] D. G. Remick, G. R. Bolgos, J. Siddiqui, J. Shin, and J. A. Nemzek, "Six at six: interleukin-6 measured 6 h after the initiation of sepsis predicts mortality over 3 days," *Shock,* vol. 17, pp. 463-467, 2002.
[167] K. Doi, A. Leelahavanichkul, P. S. Yuen, and R. A. Star, "Animal models of sepsis and sepsis-induced kidney injury," *J Clin Invest,* vol. 119, pp. 2868-2878, 2009.
[168] S. Ruiz, F. Vardon-Bounes, V. Merlet-Dupuy, J.-M. Conil, M. Buléon, O. Fourcade, I. Tack, and V. Minville, "Sepsis modeling in mice: ligation length is a major severity factor in cecal ligation and puncture," *Intensive Care Med. Exp.,* vol. 4, pp. 22, 2016.
[169] Y. Li, B. Liu, E. Y. Fukudome, J. Lu, W. Chong, G. Jin, Z. Liu, G. C. Velmahos, M. deMoya, D. R. King, and H. B. Alam, "Identification of Cit H3 as a Potential Serum Protein Biomarker in a Lethal Model of LPS-induced Shock," *Surgery,* vol. 150, pp. 442-451, 2011.
[170] W. Xiao, M. N. Mindrinos, J. Seok, J. Cuschieri, A. G. Cuenca, H. Gao, D. L. Hayden, L. Hennessy, E. E. Moore, J. P. Minei, P. E. Bankey, J. L. Johnson, J. Sperry, A. B. Nathens, T. R. Billiar, M. A. West, B. H. Brownstein, P. H. Mason, H. V. Baker, C. C. Finnerty, M. G. Jeschke, M. C. Lopez, M. B. Klein, R. L. Gamelli, N. S. Gibran, B.

Arnoldo, W. Xu, Y. Zhang, S. E. Calvano, G. P. McDonald-Smith, D. A. Schoenfeld, J. D. Storey, J. P. Cobb, H. S. Warren, L. L. Moldawer, D. N. Herndon, S. F. Lowry, R. V. Maier, R. W. Davis, R. G. Tompkins, Inflammation, and P. Host Response to Injury Large-Scale Collaborative Research, "A genomic storm in critically injured humans," *J Exp Med,* vol. 208, pp. 2581-2590, 2011.
[171] T. Zhao, B. Pan, H. B. Alam, B. Liu, R. T. Bronson, Q. Deng, E. Wu, and Y. Li, "Protective effect of Cl-amidine against CLP-induced lethal septic shock in mice," *Sci Rep,* vol. 6, pp. 36696, 2016.
[172] P. Y. Chen, N. T. Huang, M. T. Chung, T. T. Cornell, and K. Kurabayashi, "Label-free cytokine micro- and nano-biosensing towards personalized medicine of systemic inflammatory disorders," *Adv. Drug Delivery Rev.,* vol. 95, pp. 90-103, 2015.
[173] R. Satija, and A. K. Shalek, "Heterogeneity in immune responses: from populations to single cells," *Trends Immunol,* vol. 35, pp. 219-229, 2014.
[174] J. W. Uhr, "The Heterogeneity of the Immune Response," *Science,* vol. 145, pp. 457-464, 1964.
[175] H. Li, C. Tsai, A. L. Koh, L. Cai, A. W. Contryman, A. H. Fragapane, J. Zhao, H. S. Han, H. C. Manoharan, and F. Abild-Pedersen, "Activating and Optimizing MoS_2 Basal Planes for Hydrogen Evolution Through the Formation of Strained Sulphur Vacancies," *Nat. Mater.,* vol. 15, pp. 48-53, 2016.
[176] O. Lopez-Sanchez, D. Lembke, M. Kayci, A. Radenovic, and A. Kis, "Ultrasensitive Photodetectors Based on Monolayer MoS_2," *Nat. Nanotechnol.,* vol. 8, pp. 497-501, 2013.
[177] Y. Park, B. Ryu, B.-R. Oh, Y. Song, X. Liang, and K. Kurabayashi, "Biotunable Nanoplasmonic Filter on Few-Layer MoS_2 for Rapid and Highly Sensitive Cytokine Optoelectronic Immunosensing," *ACS Nano,* vol. 11, pp. 5697-5705, 2017.
[178] B. Ryu, H. Nam, B.-R. Oh, Y. Song, P. Chen, Y. Park, W. Wan, K. Kurabayashi, and X. Liang, "Cyclewise Operation of Printed MoS_2 Transistor Biosensors for Rapid Biomolecule Quantification at Femtomolar Levels," *ACS Sens.,* vol. 2, pp. 274-281, 2017.
[179] B. Ryu, E. Yang, Y. Park, K. Kurabayashi, and X. Liang, "Fabrication of Prebent MoS_2 Biosensors on Flexible Substrates," *J. Vac. Sci. Technol., B* vol. 35, pp. 06G805/801-806G805/808, 2017.
[180] S. Wi, H. Kim, M. Chen, H. Nam, L. J. Guo, E. Meyhofer, and X. Liang, "Enhancement of Photovoltaic Response in Multilayer MoS_2 Induced by Plasma Doping," *ACS Nano,* vol. 8, pp. 5270-5281, 2014.
[181] Y. Jang, S. Yeo, H. Kim, and S.-H. Kim, "Wafer-Scale, Conformal and Direct Growth of MoS_2 Thin Films by Atomic Layer Deposition," *Appl. Surf. Sci.,* vol. 365, pp. 160-165, 2016.
[182] S. B. Desai, S. R. Madhvapathy, M. Amani, D. Kiriya, M. Hettick, M. Tosun, Y. Zhou, M. Dubey, J. W. Ager, and D. Chrzan, "Gold-Mediated Exfoliation of Ultralarge Optoelectronically-Perfect Monolayers," *Adv. Mater.,* vol. 28, pp. 4053-4058, 2016.
[183] D. Li, S. Wi, M. Chen, B. Ryu, and X. Liang, "Nanoimprint-Assisted Shear Exfoliation Plus Transfer Printing for Producing Transition Metal Dichalcogenide Heterostructures," *J. Vac. Sci. Technol., B* vol. 34, pp. 06KA01/01-06KA01/06, 2016.
[184] D. K. Nandi, U. K. Sen, D. Choudhury, S. Mitra, and S. K. Sarkar, "Atomic Layer Deposited MoS_2 As A Carbon and Binder Free Anode in Li-Ion Battery," *Electrochim. Acta* vol. 146, pp. 706-713, 2014.

[185] J. Robertson, X. Liu, C. Yue, M. Escarra, and J. Wei, "Wafer-Scale Synthesis of Monolayer and Few-Layer MoS_2 via Thermal Vapor Sulfurization," *2D Mater.,* vol. 4, pp. 045007/045001-045007/045013, 2017.
[186] L. K. Tan, B. Liu, J. H. Teng, S. Guo, H. Y. Low, and K. P. Loh, "Atomic Layer Deposition of A MoS_2 Film," *Nanoscale,* vol. 6, pp. 10584-10588, 2014.
[187] H. Yu, M. Liao, W. Zhao, G. Liu, X. Zhou, Z. Wei, X. Xu, K. Liu, Z. Hu, and K. Deng, "Wafer-Scale Growth and Transfer of Highly-Oriented Monolayer MoS_2 Continuous Films," *ACS Nano,* vol. 11, pp. 12001-12007, 2017.
[188] M. Amani, M. L. Chin, A. L. Mazzoni, R. A. Burke, S. Najmaei, P. M. Ajayan, J. Lou, and M. Dubey, "Growth-Substrate Induced Performance Degradation in Chemically Synthesized Monolayer MoS_2 Field Effect Transistors," *Appl. Phys. Lett.,* vol. 104, pp. 203506/203501-203506/203505, 2014.
[189] R. Ionescu, A. George, I. Ruiz, Z. Favors, Z. Mutlu, C. Liu, K. Ahmed, R. Wu, J. S. Jeong, and L. Zavala, "Oxygen Etching of Thick MoS_2 Films," *Chem. Commun.,* vol. 50, pp. 11226-11229, 2014.
[190] J. Jadwiszczak, C. O'Callaghan, Y. Zhou, D. S. Fox, E. Weitz, D. Keane, C. P. Cullen, I. O'Reilly, C. Downing, and A. Shmeliov, "Oxide-Mediated Recovery of Field-Effect Mobility in Plasma-Treated MoS_2," *Sci. Adv.,* vol. 4, pp. eaao5031/5031-eaao5031/5010, 2018.
[191] S. Y. Yang, J. G. Oh, D. Y. Jung, H. Choi, C. H. Yu, J. Shin, C. G. Choi, B. J. Cho, and S. Y. Choi, "Metal-Etching-Free Direct Delamination and Transfer of Single-Layer Graphene with A High Degree of Freedom," *Small,* vol. 11, pp. 175-181, 2015.
[192] Y. Liu, H. Nan, X. Wu, W. Pan, W. Wang, J. Bai, W. Zhao, L. Sun, X. Wang, and Z. Ni, "Layer-by-Layer Thinning of MoS_2 by Plasma," *ACS Nano,* vol. 7, pp. 4202-4209, 2013.
[193] J. Zhao, H. Yu, W. Chen, R. Yang, J. Zhu, M. Liao, D. Shi, and G. Zhang, "Patterned Peeling 2D MoS_2 Off The Substrate," *ACS Appl. Mater. Interfaces,* vol. 8, pp. 16546-16550, 2016.
[194] G. H. Han, N. J. Kybert, C. H. Naylor, B. S. Lee, J. Ping, J. H. Park, J. Kang, S. Y. Lee, Y. H. Lee, and R. Agarwal, "Seeded Growth of Highly Crystalline Molybdenum Disulphide Monolayers at Controlled Locations," *Nat. Commun.,* vol. 6, pp. 6128/6121-6128/6126, 2015.
[195] D. Sun, A. E. Nguyen, D. Barroso, X. Zhang, E. Preciado, S. Bobek, V. Klee, J. Mann, and L. Bartels, "Chemical Vapor Deposition Growth of A Periodic Array of Single-Layer MoS_2 Islands via Lithographic Patterning of An SiO_2/Si Substrate," *2D Mater.,* vol. 2, pp. 045014/045011-045014/045015, 2015.
[196] X. Chen, Y. J. Park, T. Das, H. Jang, J.-B. Lee, and J.-H. Ahn, "Lithography-Free Plasma-Induced Patterned Growth of MoS_2 and Its Heterojunction with Graphene," *Nanoscale,* vol. 8, pp. 15181-15188, 2016.
[197] N. Otsu, "A Threshold Selection Method from Gray-Level Histograms," *IEEE Trans. Syst., Man, Cybern.,* vol. 9, pp. 62-66, 1979.
[198] R. Hinchet, A. Ghaffarinejad, Y. Lu, J. Y. Hasani, S.-W. Kim, and P. Basset, "Understanding and Modeling of Triboelectric-Electret Nanogenerator," *Nano Energy,* vol. 47, pp. 401-409, 2018.

[199] M.-L. Seol, S.-H. Lee, J.-W. Han, D. Kim, G.-H. Cho, and Y.-K. Choi, "Impact of Contact Pressure on Output Voltage of Triboelectric Nanogenerator Based on Deformation of Interfacial Structures," *Nano Energy,* vol. 17, pp. 63-71, 2015.
[200] H. J. Kim, H. Kim, S. Yang, and J. Y. Kwon, "Grains in Selectively Grown MoS_2 Thin Films," *Small,* vol. 13, pp. 1702256/1702251-1702256/1702257, 2017.
[201] H. Li, Q. Zhang, C. C. R. Yap, B. K. Tay, T. H. T. Edwin, A. Olivier, and D. Baillargeat, "From Bulk to Monolayer MoS_2: Evolution of Raman Scattering," *Adv. Funct. Mater.,* vol. 22, pp. 1385-1390, **2012**.
[202] M. Boukhicha, M. Calandra, M.-A. Measson, O. Lancry, and A. Shukla, "Anharmonic Phonons in Few-Layer MoS_2: Raman Spectroscopy of Ultralow Energy Compression and Shear Modes," *Phys. Rev. B,* vol. 87, pp. 195316/195311-195316/195315, **2013**.
[203] S. Hussain, M. A. Shehzad, D. Vikraman, M. F. Khan, J. Singh, D.-C. Choi, Y. Seo, J. Eom, W.-G. Lee, and J. Jung, "Synthesis and Characterization of Large-Area and Continuous MoS_2 Atomic Layers by RF Magnetron Sputtering," *Nanoscale,* vol. 8, pp. 4340-4347, 2016.
[204] R. Cheng, S. Jiang, Y. Chen, Y. Liu, N. Weiss, H.-C. Cheng, H. Wu, Y. Huang, and X. Duan, "Few-Layer Molybdenum Disulfide Transistors and Circuits for High-Speed Flexible Electronics," *Nat. Commun.,* vol. 5, pp. 5143/5141-5143/5149, 2014.
[205] S. Najmaei, Z. Liu, W. Zhou, X. Zou, G. Shi, S. Lei, B. I. Yakobson, J.-C. Idrobo, P. M. Ajayan, and J. Lou, "Vapour Phase Growth and Grain Boundary Structure of Molybdenum Disulphide Atomic Layers," *Nat. Mater.,* vol. 12, pp. 754-759, 2013.
[206] C. Zhou, X. Wang, S. Raju, Z. Lin, D. Villaroman, B. Huang, H. L.-W. Chan, M. Chan, and Y. Chai, "Low Voltage and High ON/OFF Ratio Field-Effect Transistors Based on CVD MoS_2 and Ultra High-k Gate Dielectric PZT," *Nanoscale,* vol. 7, pp. 8695-8700, 2015.
[207] J.-H. Ahn, W. M. Parkin, C. H. Naylor, A. C. Johnson, and M. Drndić, "Ambient Effects on Electrical Characteristics of CVD-Grown Monolayer MoS_2 Field-Effect Transistors," *Sci. Rep.,* vol. 7, pp. 4075/4071-4075/4079, 2017.
[208] H. Bergeron, V. K. Sangwan, J. J. McMorrow, G. P. Campbell, I. Balla, X. Liu, M. J. Bedzyk, T. J. Marks, and M. C. Hersam, "Chemical Vapor Deposition of Monolayer MoS_2 Directly on Ultrathin Al_2O_3 for Low-Power Electronics," *Appl. Phys. Lett.,* vol. 110, pp. 053101/053101-053101/053105, 2017.
[209] V. K. Sangwan, D. Jariwala, I. S. Kim, K.-S. Chen, T. J. Marks, L. J. Lauhon, and M. C. Hersam, "Gate-Tunable Memristive Phenomena Mediated by Grain Boundaries in Single-Layer MoS_2," *Nat. Nanotechnol.,* vol. 10, pp. 403-406, 2015.
[210] P. Bampoulis, R. van Bremen, Q. Yao, B. Poelsema, H. J. Zandvliet, and K. Sotthewes, "Defect Dominated Charge Transport and Fermi Level Pinning in MoS_2/Metal Contacts," *ACS Appl. Mater. Interfaces,* vol. 9, pp. 19278-19286, 2017.
[211] V. K. Sangwan, H.-S. Lee, H. Bergeron, I. Balla, M. E. Beck, K.-S. Chen, and M. C. Hersam, "Multi-Terminal Memtransistors from Polycrystalline Monolayer Molybdenum Disulfide," *Nature,* vol. 554, pp. 500-504, 2018.
[212] C. Li, M. Hu, Y. Li, H. Jiang, N. Ge, E. Montgomery, J. Zhang, W. Song, N. Dávila, and C. E. Graves, "Analogue Signal and Image Processing with Large Memristor Crossbars," *Nat. Electron.,* vol. 1, pp. 52-59, 2018.

[213] A. Priye, S. Wong, Y. Bi, M. Carpio, J. Chang, M. Coen, D. Cope, J. Harris, J. Johnson, and A. Keller, "Lab-On-A-Drone: Toward Pinpoint Deployment of Smartphone-Enabled Nucleic Acid-Based Diagnostics for Mobile Health Care," *Anal. Chem.,* vol. 88, pp. 4651-4660, 2016.
[214] T. Someya, Z. Bao, and G. G. Malliaras, "The Rise of Plastic Bioelectronics," *Nature,* vol. 540, pp. 379-385, 2016.
[215] J. Kim, R. Ghaffari, and D.-H. Kim, "The Quest for Miniaturized Soft Bioelectronic Devices," *Nat. Biomed. Eng.,* vol. 1, pp. 0049/0041-0049/0044, 2017.
[216] X. Pan, X. Hong, L. Xu, Y. Li, M. Yan, and L. Mai, "On-Chip Micro/Nano Devices for Energy Conversion and Storage," *Nano Today,* vol., pp. 100764/100761-100764/100723, 2019.
[217] J. Zhou, J. Qin, X. Zhang, C. Shi, E. Liu, J. Li, N. Zhao, and C. He, "2D Space-Confined Synthesis of Few-Layer MoS_2 Anchored on Carbon Nanosheet for Lithium-Ion Battery Anode," *ACS Nano,* vol. 9, pp. 3837-3848, 2015.
[218] J. Huang, Z. Wei, J. Liao, W. Ni, C. Wang, and J. Ma, "Molybdenum and Tungsten Chalcogenides for Lithium/Sodium-Ion Batteries: Beyond MoS_2," *J. Energy Chem.,* vol. 33, pp. 100-124, 2019.
[219] K. Chang, and W. Chen, "L-Cysteine-Assisted Synthesis of Layered MoS_2/Graphene Composites with Excellent Electrochemical Performances for Lithium Ion Batteries," *ACS Nano,* vol. 5, pp. 4720-4728, 2011.
[220] L. Ma, B. Zhao, X. Wang, J. Yang, X. Zhang, Y. Zhou, and J. Chen, "MoS_2 Nanosheets Vertically Grown on Carbonized Corn Stalks as Lithium-Ion Battery Anode," *ACS Appl. Mater. Interfaces,* vol. 10, pp. 22067-22073, 2018.
[221] Y. Teng, H. Zhao, Z. Zhang, Z. Li, Q. Xia, Y. Zhang, L. Zhao, X. Du, Z. Du, and P. Lv, "MoS_2 Nanosheets Vertically Grown on Graphene Sheets for Lithium-Ion Battery Anodes," *ACS Nano,* vol. 10, pp. 8526-8535, 2016.
[222] Y. Jiao, A. Mukhopadhyay, Y. Ma, L. Yang, A. M. Hafez, and H. Zhu, "Ion Transport Nanotube Assembled with Vertically Aligned Metallic MoS_2 for High Rate Lithium-Ion Batteries," *Adv. Energy Mater.,* vol. 8, pp. 1702779/1702771-1702779/1702779, 2018.
[223] G. Wang, J. Zhang, S. Yang, F. Wang, X. Zhuang, K. Müllen, and X. Feng, "Vertically Aligned MoS_2 Nanosheets Patterned on Electrochemically Exfoliated Graphene for High-Performance Lithium and Sodium Storage," *Adv. Energy Mater.,* vol. 8, pp. 1702254/1702251-1702254/1702258, 2018.
[224] X. Liang, X. Zhang, W. Liu, D. Tang, B. Zhang, and G. Ji, "A Simple Hydrothermal Process to Grow MoS_2 Nanosheets with Excellent Dielectric Loss and Microwave Absorption Performance," *J. Mater. Chem. C,* vol. 4, pp. 6816-6821, 2016.
[225] X. Zheng, Y. Zhu, Y. Sun, and Q. Jiao, "Hydrothermal Synthesis of MoS_2 with Different Morphology and Its Performance in Thermal Battery," *J. Power Sources,* vol. 395, pp. 318-327, 2018.
[226] L. Luo, M. Shi, S. Zhao, W. Tan, X. Lin, H. Wang, and F. Jiang, "Hydrothermal Synthesis of MoS_2 with Controllable Morphologies and Its Adsorption Properties for Bisphenol A," *J. Saudi Chem. Soc.,* vol. 23, pp. 762-773, 2019.
[227] B. Ryu, D. Li, C. Park, H. Rokni, W. Lu, and X. Liang, "Rubbing-Induced Site-Selective Growth of MoS_2 Device Patterns," *ACS Appl. Mater. Interfaces,* vol. 10, pp. 43774-43784, 2018.

[228] A. Teichler, J. Perelaer, and U. S. Schubert, "Inkjet Printing of Organic Electronics–Comparison of Deposition Techniques and State-of-the-art Developments," *J. Mater. Chem. C,* vol. 1, pp. 1910-1925, 2013.
[229] Y. Shi, H. Li, J. I. Wong, X. Zhang, Y. Wang, H. Song, and H. Y. Yang, "MoS_2 Surface Structure Tailoring via Carbonaceous Promoter," *Sci. Rep.,* vol. 5, pp. 10378/10371-10378/10311, 2015.
[230] T. Stephenson, Z. Li, B. Olsen, and D. Mitlin, "Lithium Ion Battery Applications of Molybdenum Disulfide (MoS_2) Nanocomposites," *Energy Environ. Sci.,* vol. 7, pp. 209-231, 2014.
[231] J. He, C. Zhang, H. Du, S. Zhang, P. Hu, Z. Zhang, Y. Ma, C. Huang, and G. Cui, "Engineering Vertical Aligned MoS_2 on Graphene Sheet Towards Thin Film Lithium Ion Battery," *Electrochim. Acta,* vol. 178, pp. 476-483, 2015.
[232] V. Shokhen, Y. Miroshnikov, G. Gershinsky, N. Gotlib, C. Stern, D. Naveh, and D. Zitoun, "On the Impact of Vertical Alignment of MoS_2 for Efficient Lithium Storage," *Sci. Rep.,* vol. 7, pp. 3280/3281-3280/3211, 2017.
[233] S. Majee, C. Liu, B. Wu, S.-L. Zhang, and Z.-B. Zhang, "Ink-jet Printed Highly Conductive Pristine Graphene Patterns Achieved with Water-Based Ink and Aqueous Doping Processing," *Carbon,* vol. 114, pp. 77-83, 2017.
[234] H. Wang, Y. Wang, X. Cao, M. Feng, and G. Lan, "Vibrational Properties of Graphene and Graphene Layers," *J. Raman Spectrosc.,* vol. 40, pp. 1791-1796, 2009.
[235] K. Rana, J. Singh, J.-T. Lee, J. H. Park, and J.-H. Ahn, "Highly Conductive Freestanding Graphene Films as Anode Current Collectors for Flexible Lithium-Ion Batteries," *ACS Appl. Mater. Interfaces,* vol. 6, pp. 11158-11166, 2014.
[236] L. Oakes, R. Carter, T. Hanken, A. P. Cohn, K. Share, B. Schmidt, and C. L. Pint, "Interface Strain in Vertically Stacked Two-Dimensional Heterostructured Carbon-MoS_2 Nanosheets Controls Electrochemical Reactivity," *Nat. Commun.,* vol. 7, pp. 11796/11791-11796/11797, 2016.
[237] L. Zhang, D. Sun, J. Kang, J. Feng, H. A. Bechtel, L.-W. Wang, E. J. Cairns, and J. Guo, "Electrochemical Reaction Mechanism of the MoS_2 Electrode in a Lithium-Ion Cell Revealed by In Situ and Operando X-ray Absorption Spectroscopy," *Nano Lett.,* vol. 18, pp. 1466-1475, 2018.
[238] S. Ding, D. Zhang, J. S. Chen, and X. W. D. Lou, "Facile Synthesis of Hierarchical MoS_2 Microspheres Composed of Few-Layered Nanosheets and Their Lithium Storage Properties," *Nanoscale,* vol. 4, pp. 95-98, 2012.
[239] J. Xiao, X. Wang, X. Q. Yang, S. Xun, G. Liu, P. K. Koech, J. Liu, and J. P. Lemmon, "Electrochemically Induced High Capacity Displacement Reaction of PEO/MoS_2/Graphene Nanocomposites with Lithium," *Advanced Functional Materials,* vol. 21, pp. 2840-2846, 2011.
[240] A. P. Cohn, L. Oakes, R. Carter, S. Chatterjee, A. S. Westover, K. Share, and C. L. Pint, "Assessing the Improved Performance of Freestanding, Flexible Graphene and Carbon Nanotube Hybrid Foams for Lithium Ion Battery Anodes," *Nanoscale,* vol. 6, pp. 4669-4675, 2014.
[241] B. M. Stewart, "The Production of High-Purity Water in the Clinical Laboratory," *Lab. Med.,* vol. 31, pp. 605-612, 2000.

[242] D. Kong, H. Wang, J. J. Cha, M. Pasta, K. J. Koski, J. Yao, and Y. Cui, "Synthesis of MoS_2 and $MoSe_2$ Films with Vertically Aligned Layers," *Nano Lett.,* vol. 13, pp. 1341-1347, 2013.